Doctor of philosophy

Graphene nanoislands on Ni(111)

Marc Ollé Soronellas

2013

Universitat Autònoma
de Barcelona

Universitat Autonoma de Barcelona
Facultat de Ciències-Física
Institut Català de Nanotecnologia

Supervisors
Dr. Gustavo Ceballos
Prof. Dr. Pietro Gambardella

Date of the graduation
April 2013

“Todos los códigos de la ética que intenten hacerte tragar,
son sólo papel moneda puesto en circulación por timadores
para despojar de sus virtudes a la gente.”
Francisco d’Aconia

Contents

Abstract

Graphene has shown extraordinary electronic and mechanical properties that can be applied in a wide variety of devices and technological fields. Exploring and controlling the different methods to obtain graphene is a crucial step for the successful implementation of this material. Epitaxial growth of graphene on metal surfaces by CVD processes has proven to be a reliable method to obtain graphene layers with good quality and, most importantly, scalable for industrial processes. In this thesis we study using Scanning Tunnel Microscopy at RT and at high temperature the Chemical Vapor Deposition (CVD) reaction that takes place in the Ni(111).

We develop a method to grow graphene nanoislands on Ni(111) by tuning the parameters involved in the CVD reaction such as the crystal temperature, propene dose and reaction time. The method consist in dosing the propene at RT and heat the sample once the dosing process is complete during a controlled time. The temperature turns out to be the most determinant parameter. Heating the sample below 400 ºC results in the formation of Ni_2C, a surface carbide that inhibits the formation of graphene at the surface. Heating the sample above 400 ºC results in the formation of graphene nanoislands with irregular shape. Above 500 ºC the number of islands diminishes strongly due to gas desorption. To obtain graphene nanoislands in a reproducible manner a minimum dose of 1 L is required, and the coverage of graphene increase with the total dose offered to the surface until it reaches the saturation value at 5 L. The heating time also has an effect in the formation of graphene nanoislands and is found to be optimum for 5 min. A post-reaction thermal treatment can lead to a shape transformaiton of the islands. Annealing at 500 ºC during 20 min forms triangular graphene nanoislands, while annealing the sample at 650 ºC for 10 min leads to hexagonal islands.

The structure of the islands is systematically studied paying special attention to the stacking configuration and island edges. Most islands exhibit a 1x1 stacking, although some islands with rotational Moiré patterns were observed. Islands obtained after the thermal treatment have straight edges, which have a crystallographic orientation characteristic of zigzag edges. On the Ni(111) the zigzag hollow (zz_h) edges are stable at RT but zigzag top (zz_t) edges present a pentagon-heptagon reconstruction named $zz_t(57)$. Triangular nanoislands exhibit zz_h edges with a predominant top-fcc stacking. The interaction between the substrate and the zz_h edges is strong enough to produce stacking changes in some small triangular nanoislands and islands with top-hcp are occasionally observed. Hexagonal nanoislands have zz_h and $zz_t(57)$ edges alternated.

Clearly the edges are related with the final shape of the islands, for that reason we studied the dynamics of the growth processes of the islands by high temperature STM. We observe that island grow in a isotropically manner with defective edges at a temperature of 450 ºC. Increasing the sample temperature at 500 ºC modify the island edges, which acquire a straight shape. The island growth at 500 ºC takes place in both types of zigzag edges with different growth velocity. Zz_t edges than grow faster than zz_h and tend to disappear. The difference in the edge growth velocity is the responsible of the evolution of the island to a triangular shape. The growth velocity of zz_h and zz_t edges equals at 650 ºC and consequently the islands grown at this temperature have an hexagonal shape.

Finally we studied the growth of a graphene monolayer on Ni(111) by in-situ high temperature STM. At the initial stages of the CVD reaction a Ni_2C layer is formed on the surface. This layer is formed at temperatures as high as 600 ºC and covers the whole surface. With some delay in time the growth of graphene is observed. The graphene grows by propagation of a reaction front. Growth of graphene is observed in a temperature range from 500 to 730 ºC.

Overall, the results provide a detailed study of the graphene growth on Ni(111) by CVD reaction focused on nanoisland growth, as well as a characterization of their structure.

1 Introduction

Graphene is a one atom thick layer of Carbon atoms forming a 2D structure. Its electronic bands were theoretically studied in the 40's [1], but considered to be unstable in free-standing conditions due to the instability of 2D structures in the free state [2, 3, 4]. However, in 2004 Geim et. al. developed a method to mechanically isolate graphene sheets from Highly Ordered Pyrolytic Graphene (HOPG) by mechanical exfoliation [5], and demonstrated that graphene is in fact stable at RT thanks to intrinsic microscopic roughening [6]. This discovering owns to him and his college Novoselov the Nobel Prize in Physics in 2010 and was the detonating step to study its properties experimentally. Since then, more than 20.000 scientific articles have been published and graphene has established as a hot topic of actual research.

Graphene is a singular material thanks to its unique electronic band, which make electrons and hole behave as relativistic particles. It has an extraordinary electronic properties which overcome those of most metals and semiconductors. Mechanically speaking, graphene is the hardest material ever tested, far above diamond. Not enough with that, graphene also have an unique optical properties, which makes it a good candidate for production of solar cells. It can be said that graphene has a new range of properties that could be applied to many technological field and, as already has been claimed, could represent a revolution in the society as plastics did in the XX century.

A necessary step is the development of new production processes able to produce graphene with different quality and price ranges. As an example graphene produced with chemical exfoliation techniques produce gram quantities of graphene at a low cost but with poor structural quality. On the other extreme, mechanically exfoliated graphene exhibits good crystalline quality but the method is not scalable and only flakes of few micrometers can be obtained. Epitaxial graphene grown by Chemical Vapor Deposition (CVD) methods on metal surfaces exhibit good crystalline quality and the method is scalable to obtain graphene buffers of several. In this thesis we study the CVD growth of graphene on nickel surfaces.

1.1 Graphene structure

Carbon atoms on graphene are bounded with p and sp^2 orbitals. Sp^2 orbitals have a planar structure and are perpendicular to p orbitals, as observed in Figure 1.1.a. The resultant structure is a 2D honeycomb lattice (Figure 1.1.b), which can be described

as an hexagonal lattice with a basis composed of two carbon atoms. The sp^2 orbitals give rise to the valence band σ and conduction band σ^*. The sp^2 covalent bond is the responsible of the extraordinary mechanical properties, such as high resistance and flexibility, which will be explained in detail below. The p orbital forms the valence band π and conduction band π^*. Near the fermi energy, only π and π^* are available, hence the electronic properties of graphene are determined by those bands. The electronic structure of graphene is shown in Figure 1.1.c. We observe that the conduction and the valence bands touch in a single point called the Dirac Point. Near this point the bands have a conic shape.

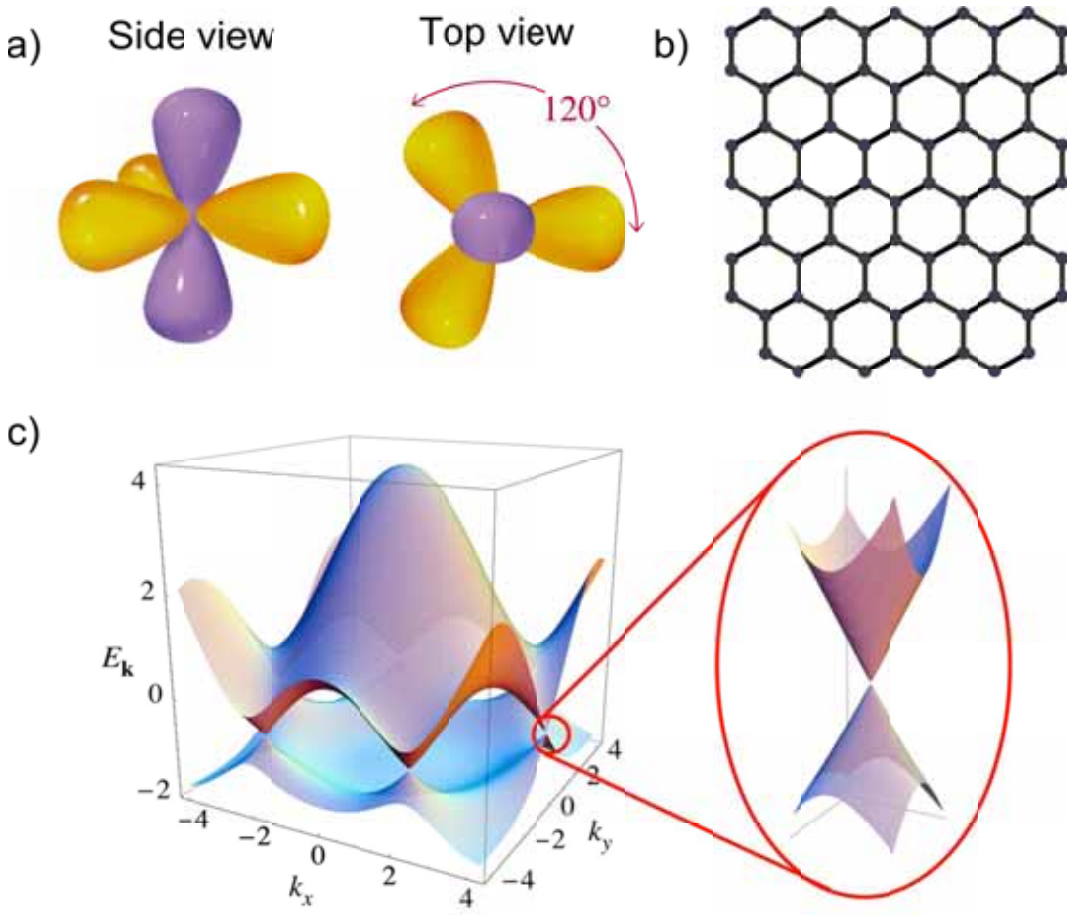

Figure 1.1: Graphene structure. a) Carbon atom with p and sp^2 orbitals [7]. b) Graphene atomic structure [8]. c) Electronic dispersion of graphene [9].

1.2 Graphene properties

1.2.1 Electronic properties.

Graphene has unique electronic band formed by the π and π^* bands, which touch in a single point at the Fermi energy called the Dirac point. Those bands have a conic shape near the Dirac point [1], what implies the electrons and holes has a zero effective mass. This means that the electrons and holes on those bands can be described by the Dirac equation and behave as Dirac fermions (relativistic particles with semi-integer spin). The Dirac equation is

$$\hat{H} = c\vec{\sigma} \cdot \hat{p}$$

where $\hat{H}$ is the Hamiltonian of the system, $\vec{\sigma}$ the Pauli Matrix, $\hat{p}$ the momentum operator and c is the speed of light. Adapting this equation to graphene

$$\hat{H} = v_f\vec{\sigma} \cdot \hat{p}$$

where $\hat{H}$ is the Hamiltonian of the system, $\vec{\sigma}$ the pseudo-spin matrix [10], $\hat{p}$ the momentum operator and v_f is the fermi velocity ($\sim 10^6 m \cdot s^{-1}$).

Hence graphene represents a unique system in where to study the properties of Dirac fermions and its unusual related effects. An intrinsic effect of electronic systems described by the Dirac equation is the minimum conductivity [11, 12, 13, 14], which can be observed in graphene since its conductance never falls below the quantum unit of conductance ($\frac{e^2}{h}$) even when the concentration of electrons or holes tends to zero[15]. Quantum Hall Effect (QHE) is observed in 2D systems such as Si or GaAs at extremely low temperature and high magnetic fields. Additionally QHE in graphene presents a unique behavior due to the pseudo-spin of its charge carriers which arise from its honeycomb structure [10]. The pseudo-spin introduce an extra degree of freedom to the system which results in an anomalous QHE named as Fractional Quantum Hall Effect (FQHE) [16]. But what is more extraordinary is the observation of FQHE in graphene at relative low magnetic fields and at RT [17] thanks to its unique properties such as large carrier concentration (up to 10^{13} cm^{-2}) with only a single 2D subband occupied and high mobility of Dirac fermions (10,000 cm^2 V^{-1} s^{-1}) at RT. The carrier concentration and mobility of graphene depends strongly on the samples. Mobilities as high as 185,000 cm^2 V^{-1} s^{-1} were reported on suspended graphene at 20 K for a carrier concentration below 5×10^{-9} cm^{-2}[18]. These value can not be attained in semiconductors, for that reason graphene is a very interesting material with potential applications in the electronic industry. Graphene has also an intrinsic interest from the magnetic point of view due to its low spin-orbit interaction, which results in long spin coherence length above 1 μm at room

temperature [19]. Spin currents can be injected and collected in graphene without suffering an important loss, which is crucial for the implementation of spintronic devices. Also, gate-tunable spin valve made of graphene has shown sharp switching at RT [20]. Hence graphene seems the ideal material to push the spintronics to a new level of sophistication.

1.2.2 Mechanical properties

The strong covalent bond of the sp^2 orbital gives graphene an extraordinary mechanical properties. Graphene has proven to be the hardest material ever tested. Changgu Lee et. al. measured the elastic properties and intrinsic breaking strength of free-standing monolayer graphene membranes by nanoindentation in an atomic force microscope [21]. They obtained a breaking strength of 42 N m^{-1}, which is a huge value for a single atom thick layer. As a comparison, assuming an effective graphene thickness of 0.335 nm, the resultant intrinsic stress is 1.3×10^{11} Pa, which is several orders of magnitude below the intrinsic stress of Diamond (2.800×10^9 Pa) and steel ($5 - 10 \times 10^8$ Pa).

1.2.3 Optical properties

The conical shape of the electronic bands of graphene strongly determine its optical properties. Theoretically graphene absorbs $\pi\alpha$ of light independently of its frequency, where α is the fine structure constant. Experimentally this value has been confirmed with very good agreement between 0.1 and 0.6 eV [22]. The frequency independence of the absorption and its high value makes graphene a promising material for solar cells, since it can use all the spectra of white light. Also, since a monolayer graphene only absorbs 2.3% of light, graphene is a good material for transparent electrodes.

1.3 Graphene synthesis

All the properties explained in previous section depend strongly on the crystalline quality of graphene layers. The crystalline quality of graphene depend strongly on the synthesis method used to obtain it. There are several methods to obtain graphene, which can be mostly divided in to groups, exfoliation and epitaxial methods.

1.3.1 Exfoliation methods

Exfoliation methods produce graphene sheets for graphitic materials, normally HOPG. HOPG has a lamellar structure, which consists of planes of graphene sheets stacked

and with an week interaction between them. For that reason it can be exfoliated easily.

1.3.1.1 Mechanical exfoliation

A good technique to obtain high quality graphene flakes is mechanical exfoliation of HOPG. It was the first developed method to obtain graphene and is still widely used for scientific applications. The mechanical exfoliation is done using a scotch tape. A HOPG is placed on a scotch tape (Figure 1.2.a), which is folded to cover the HOPG. Then the tape is unfolded, what causes the HOPG to divide in two pieces, one on each side of the tape (Figure 1.2.b). This process is repeated several until the HOPG is divided in extremely thin flakes. The flakes are transferred to a substrate (Figure 1.2.c). Luckily one of these flakes will contain a small piece of graphene, which normally are identified by optical techniques (Figure 1.2.d). Although this process seems too simple, it allow the obtainment of graphene flakes in a cheap way. Graphene flakes obtained by mechanical exfoliation are widely used for research purposes, however these method has an intrinsic randomness that limits its scalability.

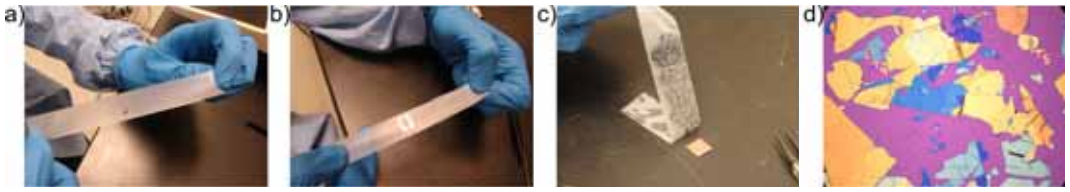

Figure 1.2: Graphene mechanical exfoliation [23].

1.3.1.2 Chemical exfoliation

The chemical exfoliation of graphene consist also in the separation of graphene layers from graphite and can be achieved by a wide variety of chemical techniques. Choucair et. al. [24] obtained gram-scale quantities of graphene by low-temperature flash pyrolysis of a solvothermal product of sodium and ethanol, followed by gentle sonication of the nanoporous carbon product. Stankovich et. al. synthesized graphene by reduction of a colloidal suspension of exfoliated graphene oxide sheets [25]. Hernandez et. al. use organic solvents to disperse and exfoliate graphite and obtain individual graphene sheets. An alternative method proposed by Dan Li et. al. consist in the the oxidation of graphite followed by its exfoliation by ultrasonication in water to obtain individual graphene oxide sheets. The graphene oxide sheets are converted back to graphene by chemical reduction. The chemical methods have the advantage of obtaining gram quantities of graphene at low cost, however the quality of the graphene layers obtained with these techniques needs to improve to achieve the needs of the electronic industry.

1.3.2 Epitaxial methods

An alternative method to obtain graphene layers is the epitaxial grow. Epitaxial techniques offer a good quality graphene layers, an easily scalable process and relative cheap. The epitaxial growth of graphene has been achieved succesfully in a wide variety of substrates, which can be divided in Silicon Carbide (SiC) and metal surfaces.

1.3.2.1 Silicon carbide

Epitaxial graphene grown on Silicon Carbide (SiC) is a promising candidate, since the industrial processes are already familiarized with silicon [26]. The epitaxial growth is achieved by thermal decomposition in two different faces of SiC, the SiC(0001) and the SiC(000$\bar{1}$), which show different advantages and disadvantages. The graphene layers obtained by this process display the properties of ideal graphene and have carrier mobilities equivalent to free-standing graphene [27]. However graphene grown on this substrate usually present areas with bi and tri-layer graphene, which can dramatically changes its properties.

1.3.2.2 Metal surfaces

Several decades before the mechanical exfoliation of graphene [5], graphene layer were obtained on metal substrates [28, 29, 30, 31, 32]. During the preparation of Ru and Pt crystals, carbon impurities segregate and form graphitic layers on the surface. The thick of these graphitic layers can be controlled by controlling the carbon density and temperature of the crystal, reaching a few graphene layers only, or even of monolayers [33]. The epitaxial growth of graphene on transition-metal substrates by chemical vapor deposition (CVD) represents one of the most promising routes for the production of large-area homogeneous graphene sheets [34, 35, 36, 37, 38, 39], offering significant advantages over the micro-mechanical cleavage of highly oriented pyrolytic graphite [40]. Graphene has been grown on several metal surfaces, being the most studied Rh(0001), Ir(111), and Ni(111). Graphene grown on metal surface has been prepared by two methods; by surface decomposition of carbon-containing molecules such as propene, ethylene, or bigger molecules, and by segregation of carbon previously dissolved in the bulk. The surface reaction of carbon-containing molecules always results in monolayer graphene, since the metal surface have a catalytic role in the reaction. The segregation of carbon to the surface can lead to a monolayer graphene, due to the difference in the thermodynamical stability of single and multiple layer graphene. Multilayer graphene can also be prepared by this method [41]. These different methods have been observed by isotope labeling by Li et. al. [42]. They grow graphene on Ni and Cu substrates by two steps dosing process using methane with C^{12} and C^{13} isotopes. Once the graphene layer is formed they measure it with Raman spectroscopy and observe the shift of the

graphene characteristic peaks due to the different nuclear mass of the isotopes. On Cu domains with different Raman signatures were observed (Figure 1.3.c,d), what indicates that carbon atoms react at the surface and the graphene was formed during the dosing of each isotope. On Ni, the Raman signature does not differentiate any domains (Figure 1.3.e), what indicates that carbon atoms dilute to the bulk and precipitate once both isotopes are mixed.

Graphene is normally grown on hexagonally close-packed metal surfaces and present a Moiré structure resulting from the lattice mismatch or the lattice misorientation with the substrate . The origin of the Moiré is explained in detail in subsubsection 4.2.3.2. On and Ru(0001) , graphene is grown normally by carbon segregation. The growth of graphene on Ru(0001) can lie to big domains, since the layers growth overpassing the limits of substrate terraces. The first graphene layer is strongly attached to the metal surface, what strongly modifies its electronic properties. However the second graphene layer is almost completely detached and shows the inherent electronic properties of graphene [34]. On Ir(111), graphene is obtained by surface decomposition of carbon containing molecules. Graphene layers on Ir(111) shows a small interaction with the substrate and its electronic structure is weekly altered [43].

The growth of graphene on Ni(111) has been achieve by both techniques, carbon segregation and surface reaction. Nickel has the advantage than the substrate have a small lattice mismatch with graphene and lies in a 1x1 stacking. This allows to produce high quality graphene monolayers. Recently, a method to transfer graphene layers from a nickel substrate to any arbitrary substrate was developed [44], allowing to obtain cheap and high quality graphene layers in a industrial scale.

1.4 Graphene nanostructures

A necessary condition for its success in the electronic industry and any nanotechnological application is the control of graphene structure and properties at the nanoscale. Owing to confinement and edge effects, graphene quantum dots have attracted considerable interest for applications in nanoelectronics [45, 46] as well as for fundamental reasons [47, 48, 49]. Moreover, theoretical investigations predict the appearance of intriguing magnetic properties on the edges of graphene islands [50, 51, 52], where zigzag edges may possess finite magnetic moments that add up in triangular islands but compensate exactly in hexagonal ones [50].

Most efforts to produce graphene nanostructures with controlled shape rely on top-down techniques such as electron beam lithography (Figure 1.4.a) [53], nanoimprint (Figure 1.4.b) [54], and scanning probe lithography [55, 56]. An interesting possibility is the fine-tuning the epitaxial process to induce the self-assembly of graphene nanostructures of well-defined shape and dimensions. On metals, graphene nanoislands have been obtained by surface segregation of bulk C [34], direct evaporation of C, and thermal dissociation of hydrocarbons on Ir(111) [57], Ru(0001) [58], Co(0001)

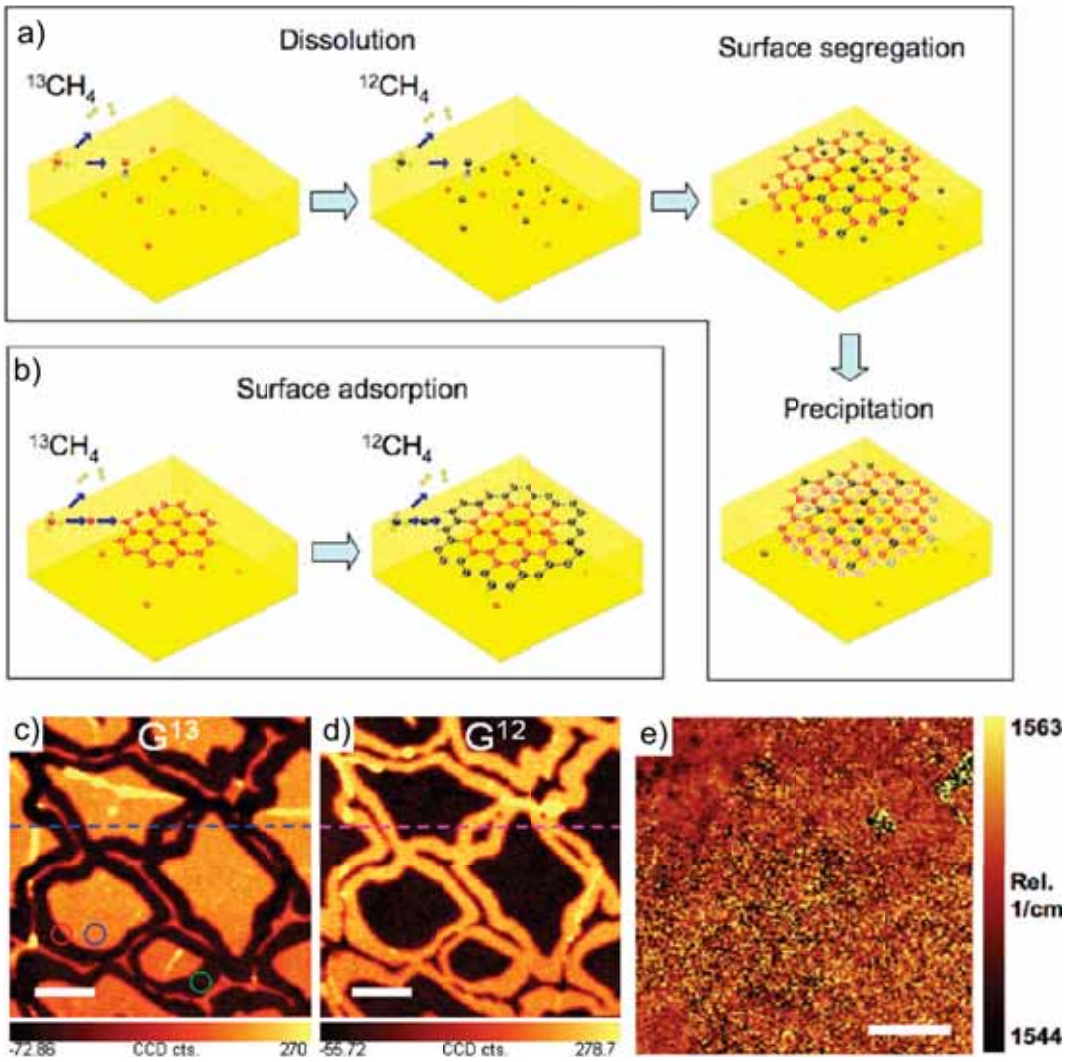

Figure 1.3: Growth by surface decomposition and carbon segregation. a) Scheme of carbon segregation growth. Red and black balls represent C^{12} and C^{13} isotopes. b) Scheme of surface decomposition growth. c,d) Intensity of G Raman peak of assigned to C^{13} and C^{12} isotopes respectively of a graphene layer on Cu. e) Relation between G bands of C^{13} and C^{12} isotopes of a graphene layer on Ni. Images obtained from[42].

(Figure 1.4.c) [48] and Cu(001) [59]. In most of such cases, the islands grow with irregular shapes and present a broad size distribution. Attempts to steer the growth process towards shape and size selection have so far been successful only for nanoribbons [60] and very small graphene-like clusters with dimensions in the range of 1 to 25 nm^2 [61, 62, 63].

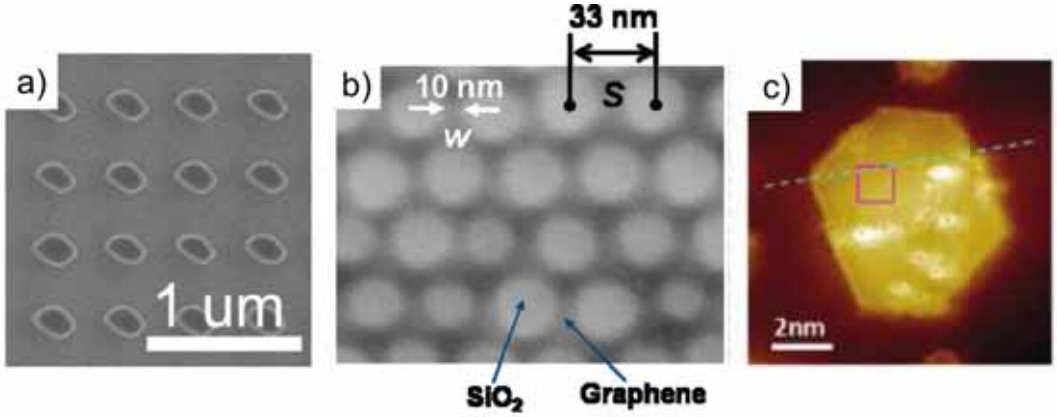

Figure 1.4: Graphene nanostructures obtained by a) electron beam lithography [53] b) nanoimprint [54]c) and epitaxial growth [48].

For graphene nanoislands on metals, the edge energy can play an important role on the islands stacking. Straight graphene edges are usually found on metals and are divided in two groups depending on the symmetry direction they follow, called zigzag and armchair edges. Once the graphene atomic structure is observed, armchair and zigzag edges can be easily distinguished by 30^o difference of their orientation. Epitaxial graphene nanoislands with zigzag edges have been observed on transition metals as Co(0001) [48], Ir(111) [64] and Pd(111) [65] . However, graphene nanoisland on these substrates do not have a lattice coincidence.

In this thesis we present a method to grow graphene nanoislands on Ni(111). We study the growth, structure and dynamics of the islands as well as the dependence on the CVD reaction on parameters such as the temperature and dose. Graphene nanoislands on Ni(111) are specially interesting for two reasons: first, the small lattice mismatch that produces the 1x1 stacking avoids any superstructure such as moiré pattern and the islands are more homogenous; and, second, the magnetic properties of nickel and its interaction with the graphene nanoislands could result in the stabilization of the net magnetic moment predicted for triangular graphene nanoislands with zigzag edges [50].

1.5 Thesis structure

After the introduction presented on this chapter, this thesis is organized as follows:

- chapter 2 explains the experimental technique used for the experiments presented, which is Scanning Tunnel Microscopy (STM). STM experiments were performed at RT and high temperature and allow us to determine the atomic structure and dynamics of the system.
- In chapter 3 we present a method to grow graphene nanoislands on Ni(111). By controlling the parameters of the reaction we are able to obtain shape selected graphene nanoislands. A modified form of this chapter is published in [66].
- In chapter 4 we study the structure of the graphene nanoislands, the stacking configuration with the substrate, and the structure of the edges. Density Functional Theory (DFT) calculations corroborate the experimental results.
- chapter 5 presents the study of the dynamics and growth processes of graphene nanoislands on Ni(111) depending on the temperature.
- In chapter 6 we show the CVD process that occurs when a hot Ni(111) surface is exposed to carbon containing gasses such as propene. The formation and stability of nickel carbide and graphene layers is studied in-situ.
- chapter 7 present the main conclusions obtained from all the experiments presented in this thesis.

2 Scanning Tunneling Microscopy

In this chapter we describe the basic functioning of scanning tunneling microscopy (STM) and scanning tunneling spectroscopy (STS) used to obtained all the experimental result described in this thesis. STM and STS are a surface characterization technique widely used in the scientific community due to their high spatial resolution, better than one Angstrom (Å) and their versatility. STM can be performed in ambient or UHV conditions and even in liquids. The basic functioning of an STM is to measure the electric current flowing between a conductive sample and a sharp conductive tip maintained at a different voltage. The tip and the sample are separated by a few Å and the electric current is very sensitive to the relative position between the tip and the sample. From this sensitivity emerges the high resolution of the STM/STS techniques. The tip is attached to a piezodrive which consist of three piezoelectric transducers that control the movement in the x-y-z directions by applying a voltage to them. The system is vibration-isolated to maintain the relative position between the tip and the sample as controlled as possible. Although STS measurements are usually done at low temperature, STM measurements can be performed in a wide range of temperature, ranging from mK to above 1000 K. No matter the temperature used, it is very important to maintain it constant to avoid thermal drift, which can affect the relative position between the tip and the sample.

Figure 2.1 shows the basic scheme of an STM. The tip is approached to the sample using a coarse positioner. Once the distance between tip and sample is of the order of a few Å, the distance is precisely controlled by the z piezo. When we apply a bias voltage between the sample and the tip, the resulting tunneling current is measured and recorded by the computer. This electric current is the primary measured quantity and is very sensitive to the distance between tip and sample surface. It is used to obtain a contour of the sample surface by scanning the sample with the x and y piezos. The tunneling current is produced due to the overlap of the electronic wave functions of the sample and tip, and is a quantum phenomena that cannot be explained by classical models. Its origin is explained in detail in section 2.1.

2.1 The quantum tunneling effect

The quantum tunneling effect was predicted in the early 20th century [67]. It describes how a particle can pass through a potential energy barrier higher than its

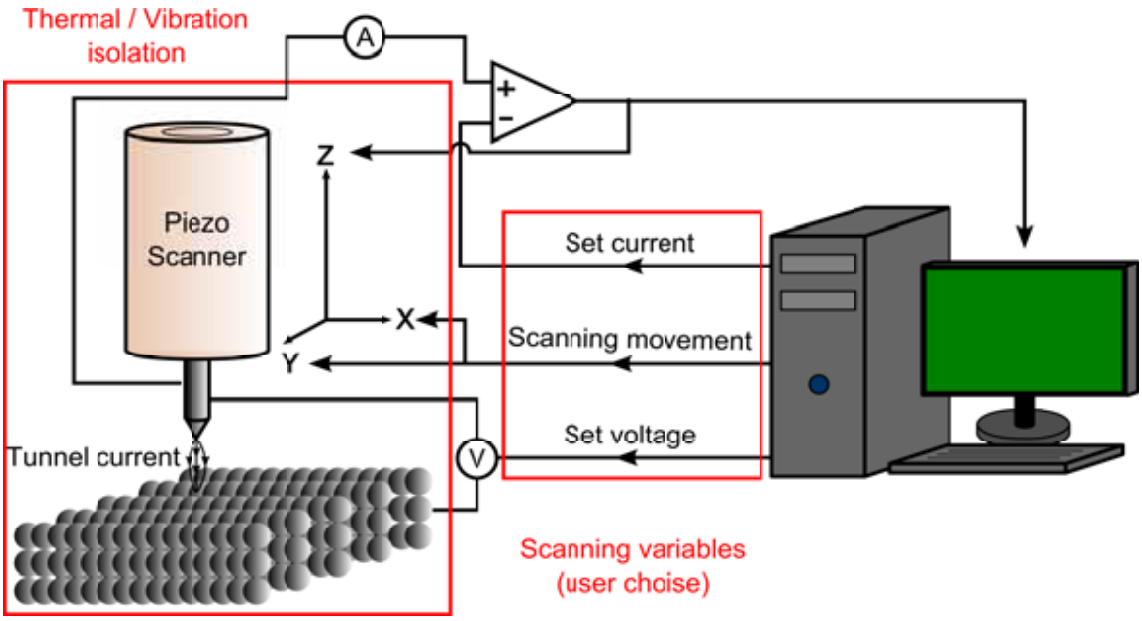

Figure 2.1: The scanning tunnel microscopy. An atomically sharp tip is placed near a sample surface and moved through it using a piezo scanner. Due to the bias voltage applied between the sample and the tip a tunnel current flows, which is recorded and used to obtain information of the sample surface. The informations obtained gives us information about the sample surface topography and electronic properties.

own energy. In classical mechanics the particle will never penetrate in the potential barrier, but a detailed study of the problem using quantum mechanics reveals that the particle can penetrate the barrier and even pass through it with a probability that depends on the height and width of the barrier. The particles of interest, in the case of STM, are electrons.

2.1.1 1D model

First we will study the quantum tunneling process in a simple 1D model as an illustrative example. In classical mechanics a particle with mass m moving in a potential $U(z)$ has total energy

$$E = \frac{p(z)^2}{2m} + U(z) \tag{2.1}$$

where z is the position of the particle and $p(z)$ is the kinetic momentum. From this relationship, the kinetic momentum of the particle is

$$p(z) = \sqrt{2m(E - U(z))} \qquad . \tag{2.2}$$

Equation 2.2 implies that the particle can move only in regions where $U(z) \leq E$, otherwise p will be imaginary, which is not possible.

This conclusion is not valid for quantum mechanics. In quantum mechanics a particle with mass m moving in a potential $U(z)$ is described by the Schrödinger equation

$$-\frac{\hbar^2}{2m}\frac{d^2}{dz^2}\psi(z) + U(z)\psi(z) = E\psi(z) \tag{2.3}$$

where $\psi(z)$is the wave function of the particle. For simplicity we consider a potential of the form

$$U(z) = \begin{cases} U & 0 \leq z \leq m \\ 0 & z < 0 \text{ or } d < z \end{cases} \tag{2.4}$$

Using Equation 2.3 andEquation 2.4 we obtain

$$\psi(z) \propto e^{\pm ikz} \qquad \text{with} \qquad k = \frac{\sqrt{2m(E - U(z))}}{\hbar} \tag{2.5}$$

where k is the particle wave vector. Opposite to the classical case, Equation 2.5 has physical meaning also for $U(z) > E$. In this case

$$\psi(z) = \psi(0)e^{-\kappa z} \qquad \text{with} \qquad \kappa = \frac{\sqrt{2m(U - E)}}{\hbar} = ik \in \mathbb{R} \qquad . \tag{2.6}$$

This means that there is a nonzero probability to find the particle inside the barrier.

To simplify the calculations we chose the phase to satisfy $\psi(0) \in \mathbb{R}$ and $\psi(0) < 0$. With these conditions and taking into account that the wave function has to be continuous, Equation 2.5 can be written as

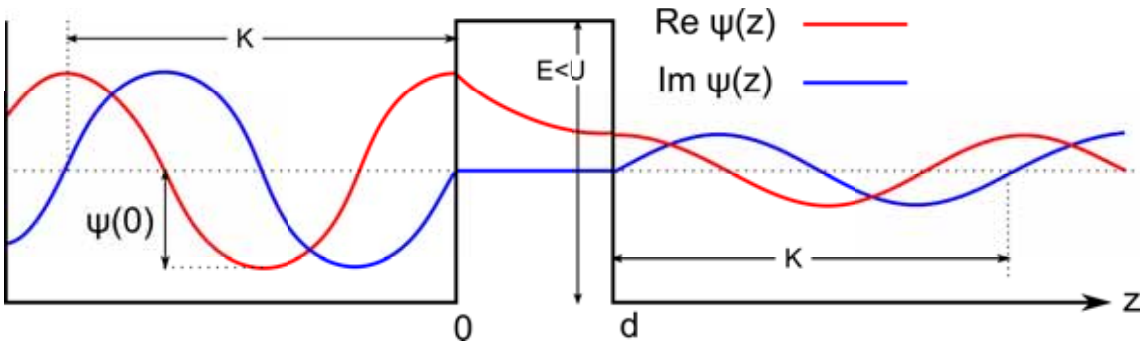

Figure 2.2: Propagation of a wave function of a free electron moving from the left to the right part through a potential barrier higher than the electron's energy in a one dimensional model.

$$\psi(z) = \begin{cases} \psi(0)e^{ikz} & z < 0 \\ \psi(0)e^{-\kappa z} & 0 \leq z \leq d \\ \psi(0)e^{-\kappa d}e^{ikz} & d < z \end{cases} \tag{2.7}$$

Figure 2.2 represents the wave function on both sides of and inside the potential barrier.

The transmission probability thoguht the barrier will be defined by

$$T(a \to b) = \frac{|\psi(b)|^2}{|\psi(a)|^2} = \frac{\left|\psi(0)e^{-\kappa d}e^{ikb}\right|^2}{|\psi(0)e^{ika}|^2} = e^{-2\kappa d} \qquad for \qquad a < 0,\ d < b \tag{2.8}$$

In an STM the tunneling effect occurs with the electrons that move between the sample surface and the tip (normally made of tungsten or platinum-iridium alloy) that is located to a distance d from the sample. Analogously to the problem discussed in subsection 2.1.1 with the simple 1D model, the potential barrier in this system is defined as the energy needed to move an electron from the surface to a free state, that is the work function ϕ of the material. To simplify the calculus the work function of the tip and the sample are defined to be equal. While the sample and the tip are at the same potential, the electrons will tunnel from the Fermi level of the sample surface to the Fermi level of the tip (and opposite). As a first approach, using Equation 2.8 we obtain

$$T(sample \to tip) = \frac{|\psi(tip)|^2}{|\psi(surface)|^2} = e^{-2\kappa d} = e^{-\frac{2d\sqrt{2m_e\phi}}{\hbar}} = e^{-10.2d\sqrt{\phi}} \tag{2.9}$$

Due to the exponential nature of the transmission probability the tunnel current is very sensitive to the distance between the surface and the tip. As an example, using the work function of Nickel (5.0 eV) measured with the photoelectric effect we obtain an increase of the transmission probability of an order of magnitude by displacing the tip from 1 Å to 11 Å.

2.1.2 Quantum tunneling beyond the 1D model

If we consider a more elaborated model, for a 3D system the problem can be addressed by separately considering the penetrations of the wave function of two electrodes to a potential barrier [68]. Then the rate of transferring electrons from one subsystem to the other can be calculated by using first-order time dependent perturbation theory. As Bardeen demonstrated [69] the probability of an electron to tunnel through two states will be determined by

$$T = \frac{2\pi}{\hbar} |M|^2 \, \delta(E_\psi - E_\chi) \qquad , \tag{2.10}$$

where ψ and χ are the wave functions of the states of the different electrodes, E_ψ and E_χ is the energy of the states and M is the tunneling matrix element that depends on the overlap of the wave functions

$$M = \frac{\hbar}{2m} \int_{z=d} (\chi^* \frac{\partial \psi}{\partial z} - \psi^* \frac{\partial \chi}{\partial z}) dS \qquad . \tag{2.11}$$

The term $\delta(E_\psi - E_\chi)$ in Equation 2.10 clearly indicates that electrons tunnel only through states with the same energy.

We can obtain a net electric current flow by applying a bias voltage (V_T) between the electrodes. As seen in Figure 2.3, this allows the transition between certain energy states that otherwise would be occupied. Depending on the sign of the bias voltage we can induce a net tunnel current flow from one direction or the opposite direction. When applying a bias voltage, the tunnel effect takes place for more than one pair of states at the same time, hence the net tunnel current will be the addition of all the tunnel channels formed by the overlapping of the wave functions of the electrodes.

$$I = e \int_{\infty}^{\infty} [f(E_F - eV_T + \epsilon) - f(E_F + \epsilon)] D_\psi(E_F - eV_T + \epsilon) D_\chi(E_F + \epsilon) T d\epsilon \tag{2.12}$$

where $f(\epsilon)$is the Fermi distribution function and $D_\psi(\mathfrak{e})$ and $D_\chi(\mathfrak{e})$ are the density of states of the different electrodes. Using the low temperature approximation, the Fermi distribution function will be approximated by a step function; in this case, Equation 2.12 can be written as

$$I = e \int_0^{eV_T} D_\psi(E_F - eV_T + \epsilon) D_\chi(E_F + \epsilon) T d\epsilon \quad . \tag{2.13}$$

For low values of the bias voltage V_T we can assume that the tunneling matrix element $|M|$ is constant for the states considered, and the tunnel current can be expressed as the convolution of the densities of states of the tip and sample:

$$I \propto \int_0^{eV_T} D_\psi(E_F - eV_T + \epsilon) D_\chi(E_F + \epsilon) d\epsilon \quad . \tag{2.14}$$

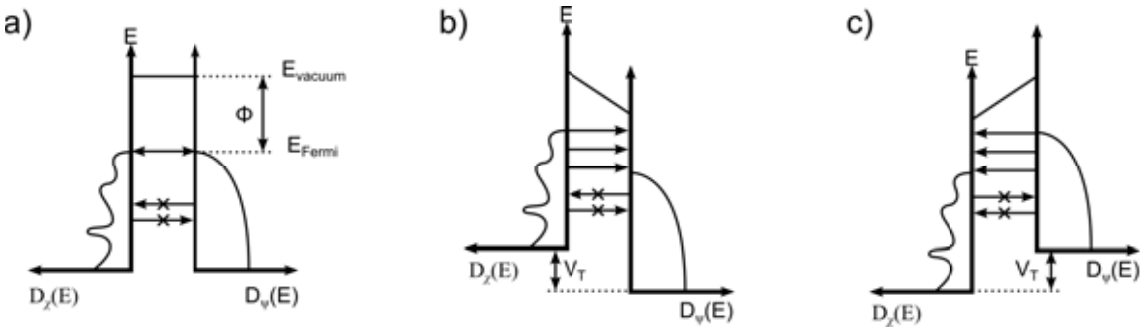

Figure 2.3: Schematics of the net current flow between the states of the sample and tip when applying a bias voltage. a) $V_T = 0$, no net tunnel current is obtained. b) $V_T > 0$, the electrons tunnel from the sample to the empty states of the tip.c) $V_T < 0$, the electrons tunnel from the tip to the empty states of the sample.

2.1.3 The Tersoff-Hamann model

Using the same perturbative approach of Bardeen, Tersoff and Hamann introduce the effect of the electronic structure of the sample and the tip shape in a more realistic model [70]. They described the wave functions using the symmetries of the system, considering the sample as a perfect surface and the tip as a sphere. The states for the sample have a wave function decays exponentially outside the sample in the perpendicular direction

$$\psi_\nu = V_s^{-1/2} \sum_G a_G \underbrace{e^{i(\vec{k}_\parallel + \vec{G})\vec{x}}}_{\text{Bloch's function}} \underbrace{e^{-\sqrt{\kappa^2 + \left|\vec{k}_\parallel + \vec{G}\right|^2} z}}_{\text{exp. decay}}$$

where V_S is the normalization surface volume, a_G is the state coefficient, $\vec{G}$ is the reciprocal lattice vector, $k_{\|}$ is the wave vector of the surface bloch wave vector of the state and $\kappa = (2m_e\phi)^{1/2}\hbar^{-1}$ is the decay rate.

In the case of the tip, Tersoff and Hamann consider it as a locally spherical (Figure 2.4)potential well with wave functions in the region of interest of the form of

$$\chi_\mu = V_{Tip}^{-1/2}\kappa R e^{\kappa R}\frac{e^{-\kappa|\vec{r}-\vec{r_0}|}}{\kappa\,|\vec{r}-\vec{r_0}|} \tag{2.15}$$

where $V_{Tip}^{-1/2}$ is the normalization tip volume and R the tip radius.

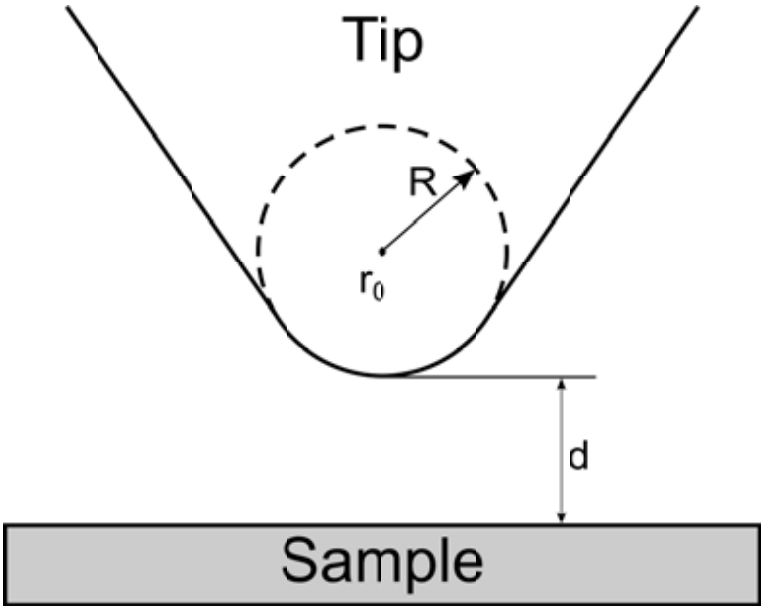

Figure 2.4: Geometry of the tip-sample system in the Tersoff-Hamann model.

Using the wave functions proposed by Tersoff and Hamann for the sample and the tip in Equation 2.11 and after a relatively complex calculation [70] one obtains

$$M_{\nu,\mu} = \frac{\hbar^2}{2m_e}4\pi\kappa^{-1}V_{Tip}^{-1/2}\kappa R e^{\kappa R}\psi_\nu(\vec{r_0}) \qquad . \tag{2.16}$$

The tunnel current for an arbitrary geometry can thus be defined as

$$I = \frac{2\pi e}{\hbar}\sum_{\mu,\nu} f(E_{\psi_\nu})[1 - f(E_{\chi_\mu} + eV_T)\,|M_{\mu,\nu}|^2\,\delta(E_{\psi_\nu} - E_{\chi_\mu}) \qquad . \tag{2.17}$$

This equation can be simplified for the low temperature case and $eV_T \ll \phi$ as

$$I = \frac{2\pi}{\hbar} e^2 V_T \sum_{\mu,\nu} |M_{\mu,\nu}|^2 \, \delta(E_{\psi_\nu} - E_F)\delta(E_{\chi_\mu} - E_F) \quad . \tag{2.18}$$

Inserting Equation 2.16 in Equation 2.18 we obtain

$$I = \frac{32\pi^3}{\hbar\kappa^4} e^2 V_T \phi^2 R^2 e^{2\kappa R} \frac{1}{V_{Tip}} \sum_{\mu,\nu} \left|\psi_\nu(\vec{r_0})\right|^2 \delta(E_{\psi_\nu} - E_F)\delta(E_{\chi_\mu} - E_F) \quad . \tag{2.19}$$

Note that the density of states is defined as

$$D(E) = \frac{1}{V} \sum_i \delta(E_{\Psi_i} - E) \tag{2.20}$$

for a system with states Ψ_i . The local density of states at a point $\vec{r}$ is defined as

$$D(E, \vec{r}) = \frac{1}{V} \sum_i |\Psi_i(r)|^2 \, \delta(E_{\Psi_i} - E) \quad . \tag{2.21}$$

Using these definitions in Equation 2.19 we obtain

$$I \propto V_T D_{Tip}(E_F) D_{Sample}(E_F, \vec{r_0}) \quad . \tag{2.22}$$

These expression is only valid for low temperatures and $eV_T \ll \phi$. A more realistic description consider the contribution of all states by integrating over the states that contribute to the tunnel process, that is the states with energies between E_F and $E_F + eV_T$ [71, 72, 73]:

$$I = \int_{E_F}^{E_F+eV_T} D_{Sample}(\epsilon - eV_T) D_{Tip}(\epsilon) T(d, \epsilon, V_T) d\epsilon \propto \int_{E_F}^{E_F+eV_T} D_{Sample}(\epsilon - eV_T, \vec{r_0}) D_{Tip}(\epsilon) d\epsilon \tag{2.23}$$

2.2 Fundamentals of STM and STS

2.2.1 Scanning tunneling microscopy

As explained in section 2.1, the quantum tunneling effect takes place between the tip and an electrically conductive sample when applying a bias voltage between them (in the range from mV to several V). For a fixed bias voltage there are two dependent magnitudes involved in a tunneling process:

1. The tunnel current: Measured between the tip and the surface, usually ranges from a few pA to a few nA.
2. The tip-surface distance: Controlled with the Z piezo, ~5-10Å.

An STM measurement consists in obtaining a representation of a certain area of the sample surface. This is done by fixing one of these parameters while measuring and recording the variation of the other. To do that, the tip is moved over the surface in the x-y plane by applying a voltage to the X and Y piezos (U_x, U_y). It describes a scanning movement consisting of parallel straight lines that cover all the measured area. Changes of the morphology and local electronic structure in this area produce changes in the tunneling conditions that are used to form an image. Depending on the parameter that is fixed the measurement is performed using one of the two scanning modes, the constant current or the constant height modes.

2.2.1.1 Constant current mode

In the constant current mode (Figure 2.5.a-b), the bias voltage is maintained constant and a tunnel current value is selected by the user. To obtain an image, the scanner moves the tip over the surface (x-y plane) and the local differences of the surface produces a change in the tunnel current (I_T). This change is detected by a feedback that reacts by applying a voltage to the z piezo (U_z) and approaches or retracts the tip to cancel the difference between the measured and the set tunnel current. Therefore, the signal $U_z(U_x, U_y)$ is recorded and can be easily transformed into $z(x, y)$ by knowing the X,Y,Z piezos responses to voltage. The function $z(x, y)$ represents the tip height depending on its position with respect to the sample surface. The final STM image in constant current mode is a representation of the values of the function $z(x, y)$ (Figure 2.5.e).

Although the basic functioning of this mode is rather simple, the fundamental understanding of the contour $z(x, y)$ is not as simple as it seems. The height of the tip cannot be interpreted as a pure topographic image. According to Equation 2.22, $z(x, y)$ represents a surface of constant density of states of the sample, which is often, but not always, related to the morphology of the sample but a convolution between topography and electronic structure. An important factor to consider is the response velocity of the feedback. A slow feedback response could result in the

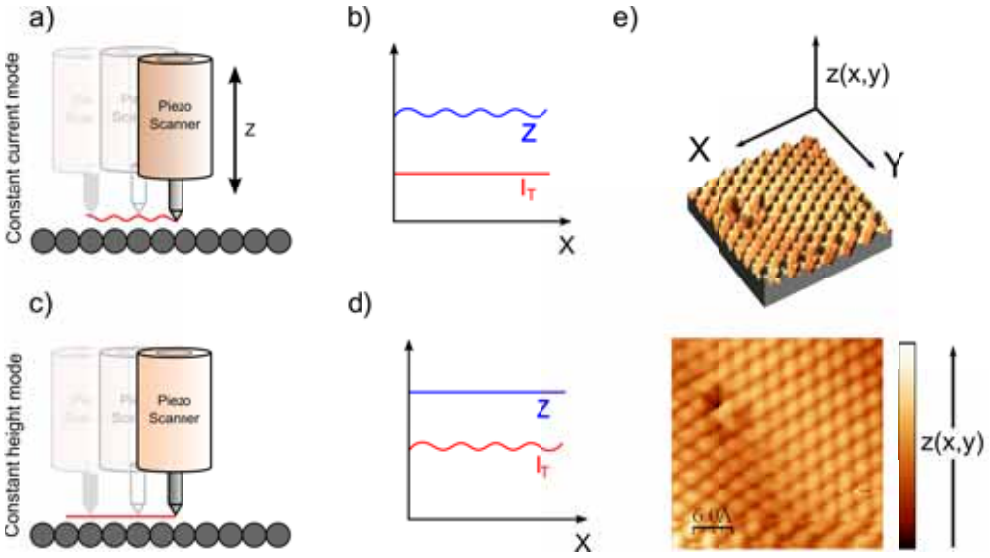

Figure 2.5: Brief description of the constant current (c.c) and constant height (c.h) mode. a) Tip movement in the c.c mode. b) Signals obtained for the tunnel current (red) and tip height(blue) in c.c mode. c) Tip movement in the c.h mode. As observed the tip is displaced in the x,y plane but not in the z direction b) Signals obtained for the tunnel current (red) and tip height(blue) in c.c mode. e) 3D (upper) and 2D (lower) representation of the same $z(x, y)$ (constant current mode) function, which constitute the STM image. The images represents an Au(111) surface with an atomic defect.

lost of information, while a fast feedback response would amplify the residual noise produced by mobile molecules absorbed on the surface or at the tip and can produce a resonance with the system vibrational frequencies. For these reason the feedback velocity has to be chose carefully and it is a limiting factor of the scan velocity.

2.2.1.2 Constant height mode

The main drawback of the constant current mode described in subsubsection 2.2.1.1 lies in the finite time of response of the feedback which affects the obtained STM image and limits the scan velocity and hence the data acquisition time. To solve this problem the feedback can be switched off completely during the scanning process and the variation of the tunnel current measured to form an image by recording $I_T(U_x, U_y)$ (Figure 2.5), which can be easily transformed into $I_T(x, y)$ by knowing the X,Y piezos response to voltage. This scanning mode is called constant height mode and is represented in Figure 2.5c-d. The main advantage to use this scanning mode lies in the high data acquisition velocity. In contrast, STM measurements in constant height mode have to be done on nearly atomically flat surfaces, since the feedback is switched off and the roughness of the surface could provoke a tip crash with the sample. Another important disadvantage of the constant height mode is

that the resulting function $I_T(x, y)$ is difficult to transform into $z(x, y)$, while in constant current mode it is obtained almost directly.

2.2.1.3 Artifacts and tip effects in STM measurements

The images obtained by STM represent the interaction between a sample surface and a tip that is supposed to be atomically sharp. However the reality is not always like this. Although the exponential decay of the tunnel current minimizes any effect of the surrounding of the end of the tip, in some cases we obtain artifacts that do not represent or distort real physical information. One of the undesired effects that affect significantly the function $Z(x, y)$ or $I_T(x, y)$ is the tip shape, as observed in Figure 2.6. When the STM measurement is performed with a tip that is not perfectly sharp, tunneling can take place simultaneously in more than a single point or even in a finite area. This leads to shadows in the final image and, in extreme cases, to a total loss of useful information. This effect is known as multiple-tip effect. Some tip preparation techniques as voltage pulses, or indentations have been developed to solve the problem of multiple tip and tip roundness, although their success depends strongly on random processes. Another important effect to be aware for the evaluation of the images is the different apparent height of different atomic species. As explained in section 2.1 the tunnel current depends on the local density of states of the surface at the tip position. Every atomic species has different states and the transition probability of electrons between them and the tip is strongly affected. As an example substitutional carbon on a Ni(111) surface results in a local minimum in the $z(x, y)$ or $I_T(x, y)$ function, while topographically speaking, both atoms are at the same height (Figure 2.6).

2.2.2 Scanning tunneling spectroscopy

The STS technique is used to electronically characterize a sample surface. The objective of this technique is to measure the change in the tunnel conditions produced by the variation of one of the three parameters described in subsection 2.2.1. Contrary to the STM technique, in STS the tip is stabilized at a certain position, and the changes in the tunnel condition are produced by the change of the bias voltage or the surface-tip distance.

As deduced from Equation 2.22 the tunnel current depends on the integral of the local density of states of the sample and tip. Therefore, by taking the derivative of the tunneling current with respect to the bias voltage , one obtains

$$\left.\frac{dI}{dV}\right|_{V_T} \propto D_{tip}(E_F) D_{Sample}(E_F, \vec{r_0}) \quad . \tag{2.24}$$

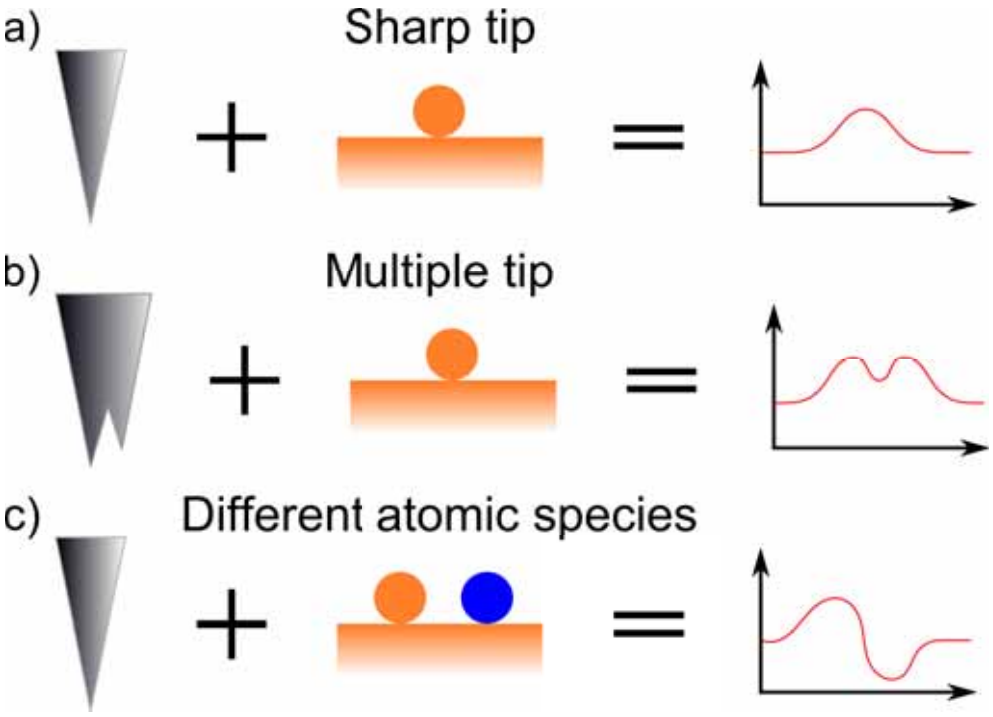

Figure 2.6: Artifacts and tip effects in STM images. a) Scan line profile for an atom on a surface in ideal conditions. b) Scan line profile for an atom on a surface with a multiple tip. c) Scan line profile for two atoms of different species on a surface.

Clearly the first derivative of the current has a measurable contribution of the density of states of the tip. For this reason, one has to be very careful to distinguish between the features attributed to the tip and the ones attributed to the sample in STS. The spectra obtained can be interpreted as a convolution between D_{Sample} and D_{Tip}. For these reason the spectra obtained reflects reasonable well the position of the peaks in D_{Sample}, while its intensity can differ significantly. When performing STS measurements, it is very important to know the form of D_{Tip}, since peaks in the density of states of the tip would be also observed in the obtained spectra. The easiest way to obtain an approximation of D_{Tip}, is by performing a spectra on a surface with a known density of states.

STS can also be used to investigate the electronic states in the field emission regime, where the bias voltage is larger than the work function. In this case, the voltage is increased while the tip is removed from the sample to maintain the tunnel current constant. This technique is used to investigate the field emission resonances (FER).

Although numerical methods can be used to obtain the first derivative of the tunnel intensity with respect to the bias voltage, a lock-in amplifier is used to directly measure it with a better signal to noise ratio and increased dynamic range.

2.3 Experimental setup

Two different experimental setups have been used in this work. In this subsection we will briefly describe the configuration and advantages of each one of them. Basically the two microscopes used for these work can be divided by the operation temperature, being these the room temperature and the high temperature setups.

2.3.1 The room temperature experimental setup.

Performing experiments at RT has the advantage that the sample preparation and analysis are far simpler and faster. These conditions are ideal for the study of systems with lots of variables involved, such as chemical vapor deposition (CVD) growth, where big series of experiments have to be done. The experimental setup for room temperature experiments consist of a UHV chamber with a base pressure below $3 \cdot 10^{-10}$ mBar (Figure 2.7.a). The pumping system of the chamber consist of an ionic pump, a titanium sublimation pump and a turbomolecular pump supported by a scroll pump. The chamber is equipped with a commercial STM 150 Aarhus to perform the STM measurements. All measurements have been performed at RT. The chamber also have a Low Energy Electron Diffraction (LEED) unit. Samples are prepared at the same chamber, which is equipped with an argon ion gun, a heating stage, a metal evaporator and leak valves to dose gases with a controlled manner.

2.3.1.1 The 150 Aarhus STM

The 150 Aarhus STM is mounted on a heavy copper block that offers to the STM head a vibrational and thermal stability as seen in Figure 2.7.b. The copper block is held by springs, which offer a good vibrational isolation.

The STM head (Figure 2.7.c) is composed by and inchworm coarse motor that holds the scanner. The tip is placed at the end of the scanner. The inchword is the responsible of approaching the tip to the sample (Z direction) and can not move in the X-Y direction. The scanner is composed by 5 piezos responsible of scanning movement, which are X^+,X^-, Y^+,Y^- and Z. The Z piezo is responsible of the distance of the tip and hence affects directly the tunnel current, the other four piezos are used to displace the tip through the surface and scan it. The sample is placed on top in the center of the STM head (silver plate in Figure 2.7.d) facing down.

In this system the tip can not be replaced without opening the chamber. For that reason an argon sputter gun is placed on top of the microscope in the UHV chamber to clean the tip by argon sputtering in case it is necessary.

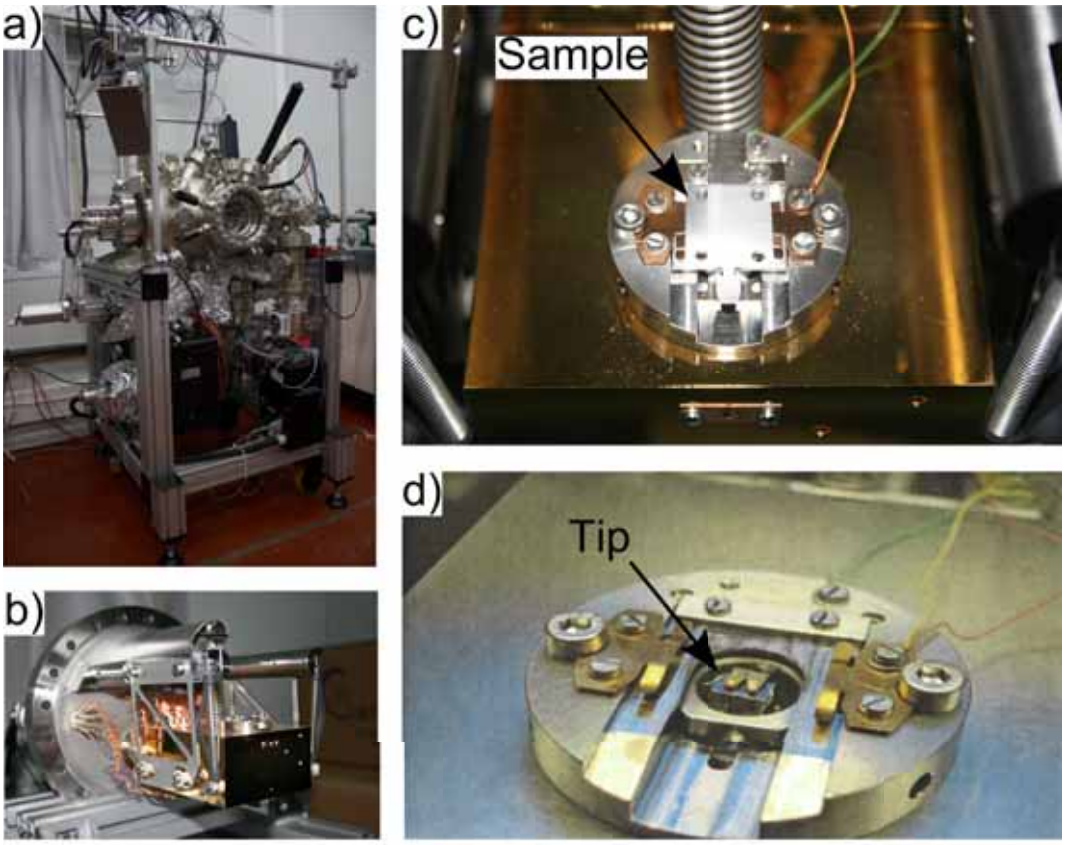

Figure 2.7: a) The room temperature STM vacuum chamber. The chamber is equipped with leak valves, two ion guns, a heating stage, and a triple metal evaporator to prepare and grow the samples. To characterize the samples the chamber is equipped with a LEED and a variable temperature STM. b) Detail of the commercial 150 Aarhus STM from the company Specs. We can observe the microscope lies in the upper part of a cooper block that provides thermal and mechanical stability. c) The sample is held on top of the microscope facing down. d) Detail of the tip, which is attached to the piezo scanner pointing upwards.

2.3.2 The high temperature experimental setup

The experimental setup for high temperature experiments consist of a UHV multi-chamber system with a base pressure below $3 \cdot 10^{-10}$ mBar (Figure 2.7.a). The system consist in a preparation chamber, a sample storage chamber and a microscope chamber. This division is done to maintain the microscope chamber and storage chamber as clean as possible. The pumping system consist of two ionic pumps, a titanium sublimation pump and two turbomolecular pumps supported by a scroll pumps. The preparation chamber is equipped with an ionic gun, a heating stage and several leak valves. The microscope chamber is equipped with a commercial STM 150 Aarhus HT to perform the STM measurements all high temperature.

2.3.2.1 The 150 Aarhus STM HT

High temperature STM measurements offer the opportunity to study the dynamics of systems and the phenomena involved in their growth. The high temperature setup to realize these experiments consist in a UHV chamber divided in different sub-chambers. Each one of these sub-chambers can be separated of the others by using valves and are designed to realize a concrete task, such as sample preparation or sample analysis. The HT STM images are taken using a 150 Aarhus STM HT (Figure 2.8.a), which is a modification of the 150 Aarhus STM (subsubsection 2.3.1.1) consisting of an addition of a radiation heater attached to the cooper base with a high stability power supply (Figure 2.8.b), capable of stabilize the temperature with a precision of 0.1 K and up to 1300 K.

2.4 Topographic sample characterization

A good way to characterize the sample composition is to compare the relative height of certain areas with respect to the others. In this thesis the system studied is graphene on Ni(111). Identifying graphene layers or nanoislands with their topography is quite easy and allows us to identify them rapidly. For that we have to know the height of nickel steps and the apparent height of graphene on Ni(111), which depends on the bias voltage used. Figure 2.9.a shows an STM image of a clean Ni(111) surface. The height of the nickel terrace steps is 2.1 Å and is independent of the bias voltage, since the dependence of the tunnel current with the bias voltage is the same for all terraces. Figure 2.9.b shows an STM image of a graphene nanoislands of Ni(111) with a bias voltage of 10 mV. The apparent height of the island is 1.6 Å, but change with different bias voltages. As an example Figure 2.9.c shows a decrease of the apparent height down to 1.2 Å for a bias voltage of 400 mV, which increase to 1.5 Å when measuring with a bias voltage of 1.3 V (Figure 2.9.d). The different electronic states below the bias voltage of Ni(111) and graphene on Ni(111) contribute in a different manner to the tunnel current, what results in the change of

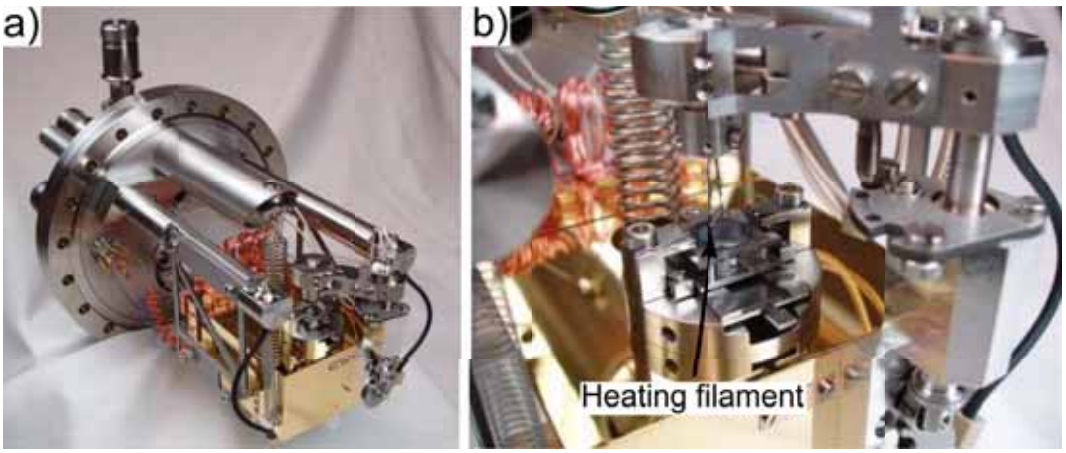

Figure 2.8: a) The high temperature measurements are done using a commercial 150 Aarhus STM with the high temperature upgrade. b) The HT upgrade consist of a filament that heats the sample by means of thermal radiation. The sample is thermally isolated from the microscope by placing the sample holder on a separation plate, which prevents radiation and diffusion heat transfer to the microscope.

the apparent height. The topographic characterization of the sample has an error of ± 0.1 Å.

As an exercise we show the characterization of a graphene partially covered Ni(111) surface. In this system we can observe 3 different values of the step height, which correspond to nickel on nickel (H_{Ni}), graphene on nickel (H_{Gr}), and the interphase of graphene and nickel on the same terrace (H_{Ni}-H_{Gr}). The STM image showed in Figure 2.10.a was obtained with a bias voltage of 0.5 V. At this voltage the apparent height of a graphene monolayer on nickel is H_{Gr}=1.2 Å. The apparent height of nickel on nickel is independent of the bias voltage and equal to 2.0 Å and the height of the interphase is H_{Ni}-H_{Gr}= 0.8 Å. With this values we can identify the different regions of a sample. The STM image shows 6 different numbered terraces. Terrace 1 corresponds to a terrace situated far below, hence will not be considered. While terraces 2, 4 and 5 are assigned to graphene monolayers, terraces 2 and 6 are assigned to nickel. The height difference between terraces 3 and 4 is 1.2 Å (blue height profile), this identifies terrace 3 as a nickel terrace, while terrace 4 is the graphene monolayer that lies on it. The height difference between graphene terraces 2, 4 and 5 is 2.0 Å, which corresponds to a nickel terrace step. Hence these terraces are graphene monolayers situated on different nickel terraces. The height difference between terrace 5 and 6 is 0.8 Å, which is the height difference of a nickel-graphene interface

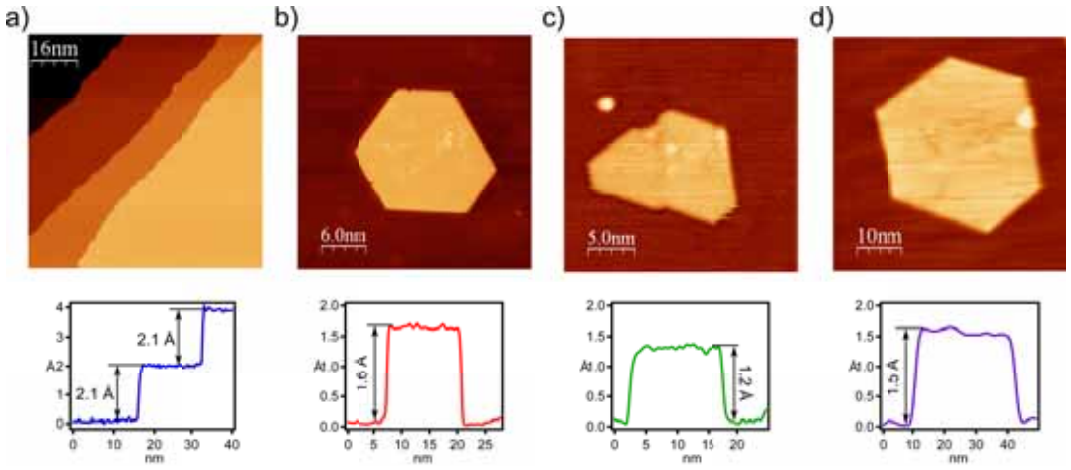

Figure 2.9: Topography dependence on Bias. a) Clean Ni(111) terrace steps showing a height of 2.1 Å. b) Graphene nanoislands on Ni(111) obtained with a bias voltage of 10 mV and with an apparent height of 1.6 Å. c) Bias voltage of 400 mV resulting in an apparent height of 1.2 Å. d) Bias voltage of 1.3 V resulting in an apparent height of 1.5 Å.

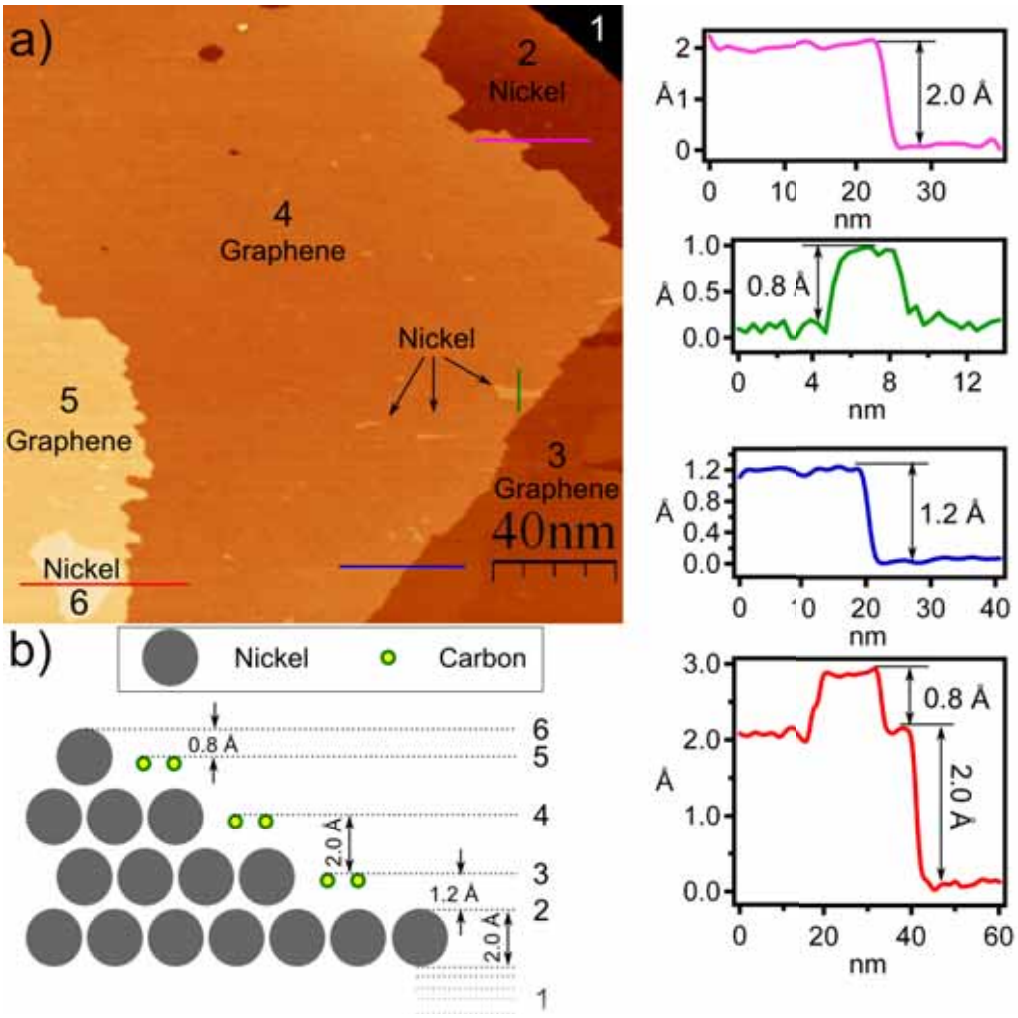

Figure 2.10: a) STM image of a partially graphene covered Ni(111) surface. The terraces are numbered for illustrative purposes. Height profiles are obtained along the line of the same color in the STM image. b) Scheme showing the height difference between the different terraces of the STM image.

3 Island growth

The catalytic decomposition of hydrocarbons on transition-metal surfaces has attracted increasing interest as a method to prepare high quality graphene layers and nanostructures. Graphene nanoislands prepared by hydrocarbon decomposition have been obtained on Ir(111) [57], Ru(0001) [58], Co(0001) [48] and Cu(001) [59]. Ni(111) appears to be an ideal substrate to tune the magnetic properties of zigzag edges present in graphene nanoislands[50] due to its surface magnetism [74] and small lattice mismatch [75]. Graphene layers on Ni(111) are prepared by decomposition of carbon containing molecules such as carbon monoxide [76], ethylene [77]and propene [78]. However the production of graphene nanostructures is still limited to other substrates and no graphene nanoislands have been grown on Ni(111) substrate.

In this chapter, we develop a method to grow graphene nanoislands on a Ni(111) surface with selected shape, dimensions from a few atoms up to 300 nm^2, and optimal edge quality. We present a systematic investigation of the growth parameters that affect the yield, structure, size, and shape of sub-monolayer C islands on Ni(111) following the deposition of propene (C_3H_6) at room temperature. We show that sequential control of the catalytic decomposition of a fixed dose of propene on nickel, reaction temperature, and post-annealing procedure leads to the formation of graphene islands with either triangular or hexagonal shape, zigzag edges and partial size selection.

3.1 Experimental details

All the experiments described in this chapter were performed in the room temperature experimental setup (subsection 2.3.1). A Ni(111) single-crystal surface was kept at all time in the ultra-high vacuum chamber with a base pressure of $3 \cdot 10^{-10}$ mbar. The crystal surface was cleaned by repeated cycles of Ar^+ sputtering followed by annealing at 800 ºC for 1 minute. The surface temperature was measured throughout the experiment using a pyrometer (IMPAC IGA 140) with ±25 ºC accuracy at 450 ºC and ±2 ºC at 500 ºC. Topographic images of the surface were obtained using a variable-temperature scanning tunneling microscope (STM) and processed using the WSxM software [79]. After the cleaning procedure, the nickel crystal presented less than 0.01 monolayers (ML) of carbon contamination in the form of nickel carbide. Such a minor contamination did not affect the growth process in a measurable way,

as verified by the absence of graphene nucleation upon annealing to 500 ºC. The procedure used to prepare the graphene nanoislands, represented in Figure 3.1, is divided in three steps:

1. Dosing of propene on Ni(111) at room temperature (RT).
2. Decomposition of propene and formation of ordered C phases at the reaction temperature $350 \leq T_R \leq 600$ ºC.
3. Post-annealing of graphene nanoislands at temperature $450 \leq T_A \leq 650$ ºC.

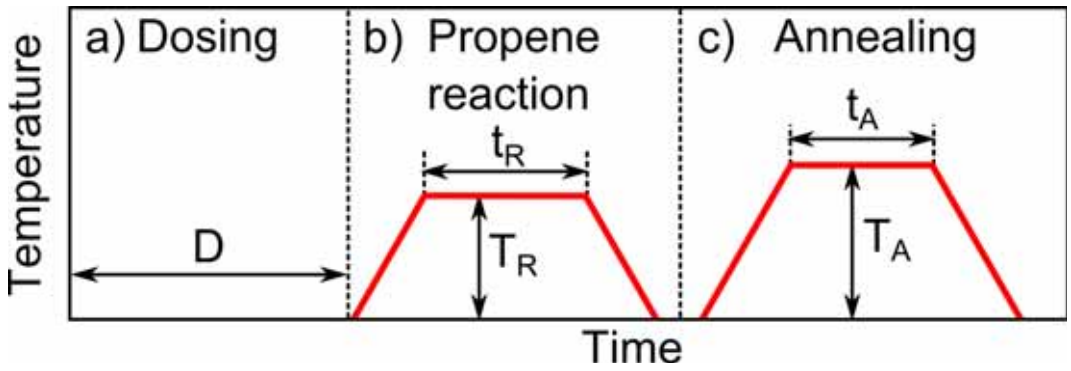

Figure 3.1: Scheme of the sample preparation procedure to form the graphene nanoislands. The preparation is divided in three main steps. a) The dosing step consists in dosing propene at a constant pressure of 10^{-6} mbar during a certain time. The final dose D is the time integral of the pressure. b) Once the dose is complete the sample is heated to a reaction temperature T_R during a time t_R. The surface reaction results in the formation of irregular graphene nanoislands. c) Post-annealing at a temperature T_A during a time t_A induce changes of the size and shape of the irregular graphene nanoislands.

During the first two steps propene decomposes and forms graphene; during the third step, surface and bulk C diffusion compete, determining the yield as well as the average size and shape of graphene nanoislands. The initial dose of propene (D) is expressed in Langmuirs, calculated by time-integration of the partial pressure of propene. Once D has reached its programmed value and the chamber has recovered its base pressure, the sample is heated up to T_R using a constant heating rate of 12 ºC/s. After reaching T_R, the sample temperature is kept stable within ±5 °C for a time t = t_R, after which heating is stopped and the sample allowed to cool at a rate of 1.7 ºC/s until RT, before transfer into the STM. This sequence is repeated on a clean surface for every value of T_R investigated in this chapter. The results of systematically varying D, t_R and T_R are described in detail in section 3.2. During the post-annealing process the graphene nanoislands are heated from RT to T_A for a time t_A, after which the sample is cooled and observed by STM. The results of the post-annealing process are explained in detail in section 3.3.

3.2 Graphene nanoislands growth

In order to describe the critical steps of graphene growth, we have systematically varied the values of the reaction parameters T_R, D, and t_R .

3.2.1 Temperature dependence

We start by describing the effect of T_R, which turns out to be the most important reaction parameter. To study the effect of this parameter we prepared a series of samples at constant dose (D = 1 L) and reaction time (t_R = 1 min) varying the value of T_R between 350 ºC and 550ºC. Figure 3.2 shows representative STM images of the submonolayer growth process obtained after step 2 described in section 3.1. As observed in Figure 3.2.a, relatively large round islands form already at T_R=350 ºC. These islands are 2.5 Å high and present a characteristic stripe pattern on their upper surface. The same pattern can be observed on the terraces, covering the entire crystal surface and forming a multi-domain striped phase. High resolution STM images of this pattern on flat terraces (Figure 3.2.e, left) reveal the atomic structure of nickel carbide (Ni_2C), as previously observed by Klink et. al. [80] and confirmed by low energy electron diffraction. Similar results are obtained for reactions up to T_R=400 ºC.

At T_R=450 ºC (Figure 3.2.b) the Ni_2C islands are still present, but the surface is only partially covered by the Ni_2C phase, which is now single-domain and concentrated on the upper part of the surface steps (light blue area on the right hand side of Figure 3.2.b). Atomic resolution images (Figure 3.2.e) taken on an area equivalent to the dark blue region of Figure 3.2.b reveal an hexagonal lattice with interatomic distance identical to that of pristine Ni(111). In the regions where pure nickel is exposed to the surface we observe small islands of irregular shape with a height of 1.5 Å, which represent the first stage of graphene formation on this surface.

Figure 3.2.c shows the preparation at T_R=500 ºC. The Ni_2C phase has entirely dissolved. On the other hand, we observe a broad distribution of islands with compact but rather irregular shape, which have the same height (1.5 Å) as the small islands observed in Figure 3.2.b. High-resolution images of these islands (Figure 3.2.e, center) show the threefold symmetry typical of the monolayer graphene structure on Ni(111) [80]. The images also show the presence of a second phase enclosed in some of the graphene islands, which we attribute to nickel atoms from its apparent height (2.1 Å). As T_R increases up to 550 ºC, we observe that the density of graphene islands has reduced drastically (Figure 3.2.d) and that the islands present a more regular shape compared to Figure 3.2.b, c. Above 600 ºC, we observe no graphene formation and the nickel surface appears clean and homogenous.

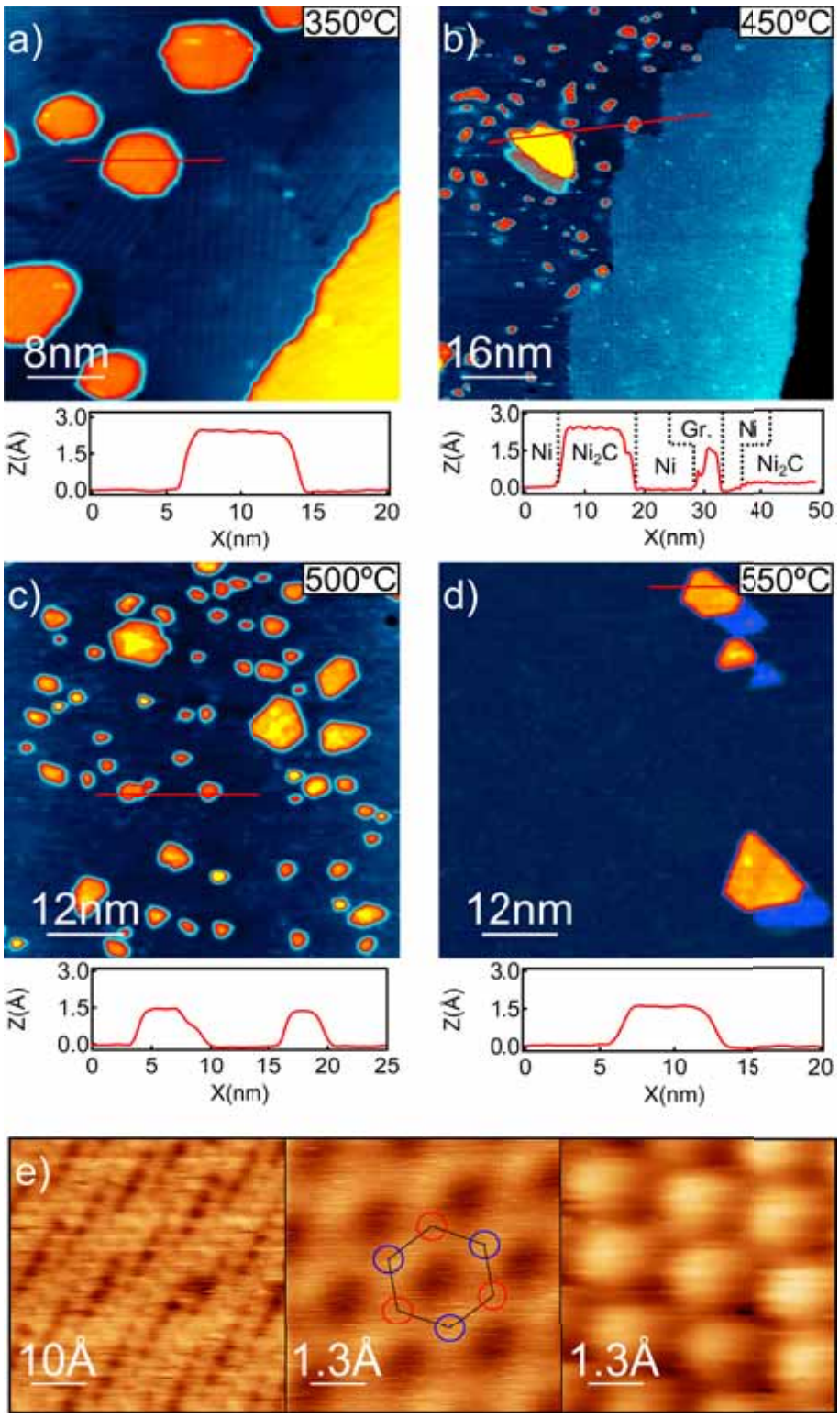

Figure 3.2: STM images of the surface topography following preparations with D=1 L, t_R=1 min and (a) T_R=350 ºC, (b) T_R=450 ºC, (c) T_R=500ºC, and (d) T_R=550 ºC. Images b and d are affected by a double tip effect. (e) Atomic resolution images of Ni_2C (left), graphene (center), and Ni(111) (right).

Clearly, there are large differences in graphene yield depending on T_R. Figure 3.3 shows the graphene coverage estimated from the STM images at different temperatures. In such analysis, we did not consider the contribution of islands smaller than 1 nm^2 and of the nickel atoms enclosed in graphene, which amount to about 0.02 of a clean nickel monolayer. We observe that the graphene yield peaks at T_R=500 ºC and decreases steeply already at 520 ºC. Graphene formation starts at around 450 ºC as the Ni_2C phase recedes. Our results show that annealing a sample covered with Ni_2C for 1 min at 500 ºC yields a clean Ni(111) surface with no traces of either graphene or carbide. Thus, the carbide phase does not transform directly into graphene. This is in agreement with the results of Lahiri et. al. [39], which showed that C atoms first dissolve into the bulk at 480 ºC, whereas nucleation of graphene from reverse C diffusion to the surface occurs on a time scale of hours.

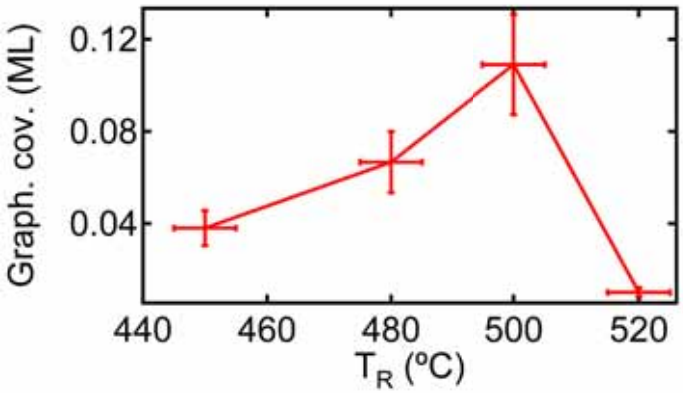

Figure 3.3: Graphene coverage as a function of T_R at constant D=1 L and t_R=1 min.

The growth process as a function of T_R is summarized in Figure 3.4. At temperatures below 400 ºC, propene reacts with nickel surface atoms to form nickel carbide, in agreement with previous observations [81]. The Ni_2C phase observed at T_R=450 ºC is most probably formed during the heating ramp, as the carbide starts to decompose around 400 ºC [82] and our data indicate that the atomic mobility is high enough to restructure the carbide domains above this temperature. As mentioned above, the carbide phase does not directly contribute to the formation of graphene but rather diffuses into the bulk upon increasing T_R to 500 ºC. Graphene formation therefore occurs above 400 ºC in the presence of C atoms directly dissociating from propene. This explains why monolayer graphene is usually grown by dosing hydrocarbons directly at high temperature. Above this point the reaction rate decreases abruptly, which can be explained by the onset of propene desorption from the surface before the reaction can take place. We thus find that the optimal reaction temperature to grow graphene on Ni(111) is 500 ºC, whereas dosing at RT allows for reproducible submonolayer control of the graphene coverage.

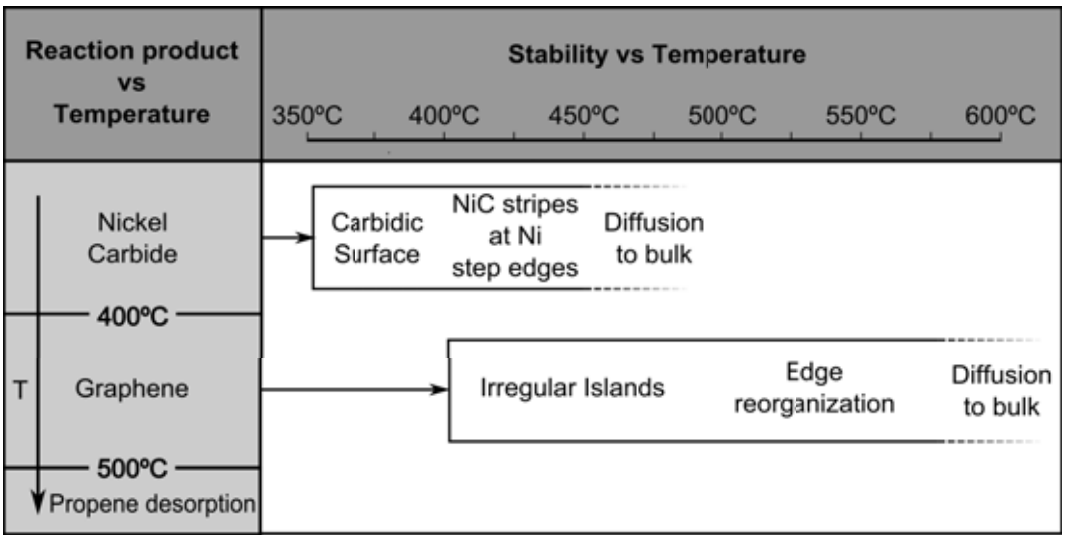

Figure 3.4: The Carbon phase formation and stability on Ni(111) surface depends strongly on the temperature. Below 400 ºC a carbidic phase is formed, above z graphitic phase prevails. The stability of carbidic and graphitic phases is compromised at high temperature.

3.2.2 Dose dependence

The relationship between the dose D and final graphene coverage has been studied at T_R=500 ºC and t_R=5 min to ensure that a maximal amount of graphene is formed and that all the propene molecules have reacted with the surface. Figure 3.5 shows that the coverage of graphene increases linearly with the propene dose up to about 0.5 ML between 1 L and 5 L. The saturation value depends on the competition between propene dissociation and desorption, which prevents the formation of a full graphene ML at constant dose. The increase in coverage is also accompanied by a change in morphology of the graphene. Below 0.1 ML, we observe isolate nanoislands of different sizes, whereas at larger coverage the islands start to coalesce, becoming large and irregular.

Low dose reproducibility Samples with $D \leq$0.5 L (T_R=500 ºC and t_R=5 min.) are not included in Figure 3.5 due to the low reproducibility of the graphene yield: most of preparations with D=0.5 L present no graphene islands, whereas for some of them the graphene coverage is lower than expected, around 0.01 ML. This behavior can be understood if we assume that the critical island size to catalyze the growth of graphene on metals is a C_5 cluster, as proposed by Zangwill and Vvedensky [83], implying that fluctuations of the density of C atoms around a minimum threshold value are critical to stabilize the growth of graphene. Meng et. al. [84] calculate the final structure of carbon atoms placed on a Ni(111) surface. Their calculations were done on a cell containing 3 terraces of 64 nickel atoms and a certain number of

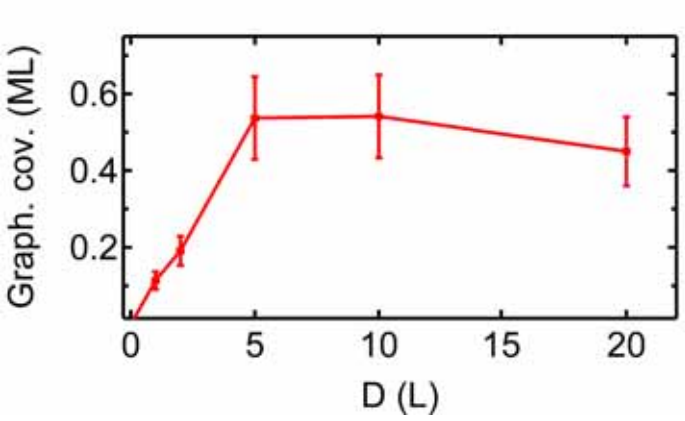

Figure 3.5: Graphene coverage as a function of D at constant T_R=500 ºC and t_R=5 min.

carbon atoms. If 32 carbon atoms are introduced to the system a graphitic structure is formed at the surface, while introducing 16 carbon atoms results in their diffusion into the bulk and no structure is formed.

The effect of this phenomena is observed in Figure 3.6, where we show two STM images with identical preparations parameters. The values used were D=0.5 L and T_R=500 ºC. However, the reaction time was increased up to t_R=25 min to increase the sample coverage by carbon precipitation (see subsection 3.2.3 and chapter 5). While for the preparation shown in Figure 3.6.a no graphene was found, the preparation shown in Figure 3.6.b results in a significant graphene coverage. In the first preparation no graphene nucleation takes place while in the second preparation the carbon concentration is high enough to nucleate graphene nanoislands that act as a seed for the graphene growth as we will show in chapter 5. Both preparations were grown consecutively, so the different result could not be attributed to different sample history.

3.2.3 Time dependence

Our study shows that the reaction time has also significant effects on the final amount of graphene, as expected for a kinetically controlled process. Figure 3.7 shows that the graphene coverage increases with t_R. For $t_R \leq 1$ min, the coverage increases rapidly with an average growth rate of $8 \cdot 10^{-2}$ ML/min and reaches saturation after 2 min at constant dose (D=1 L) and temperature (T_R=500 ºC). To study the effect of temperature at long timescales, a sample with a low initial coverage of graphene (0.06 ML) was kept at 500 ºC for up to 90 min and observed by STM at the same temperature. We found that the graphene coverage increases slowly with time with a growth rate of about $8 \cdot 10^{-4}$ ML/min (Figure 3.7). Since propene has entirely desorbed at this temperature, such a small growth rate is attributed to carbon diffusion from the bulk. We thus conclude that graphene growth occurs in two

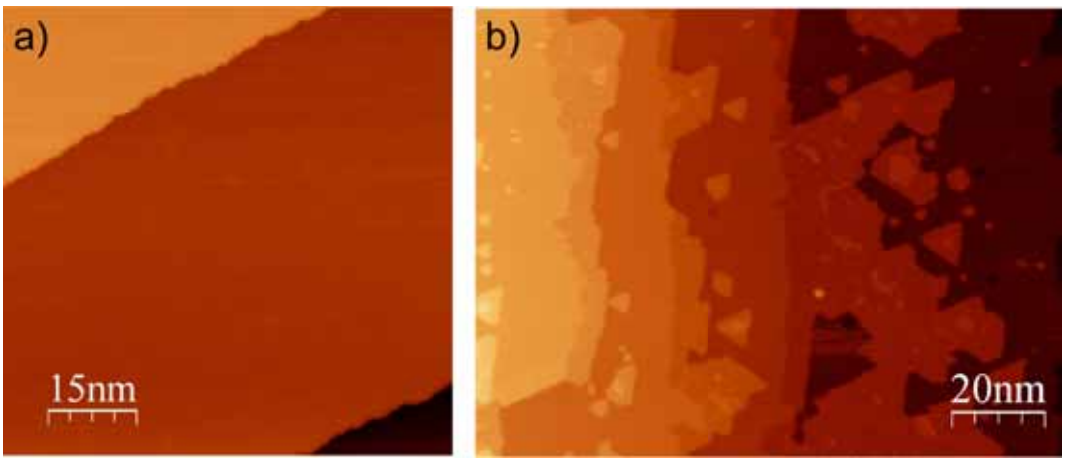

Figure 3.6: Two samples with identical preparation parameters and different result due to low reproducibility of low dose regime. Parameters used for both samples are D=0.5 L, T_R=500 ^{o}C and t_R=25 min. The resultant preparations shows a) a clean Ni(111) surface with no traces of nickel carbide nor graphene nanoislands. b) a Ni(111) surface with notorious graphene coverage.

different regimes. The first one ($t_R \leq 5$ min) is characterized by a high growth rate and attributed to carbon obtained directly from the propene reaction, whereas the second regime is characterized by a very low growth rate and is attributed to carbon precipitation from the bulk. The effects of the growth by carbon precipitation is studied in detail in chapter 5.

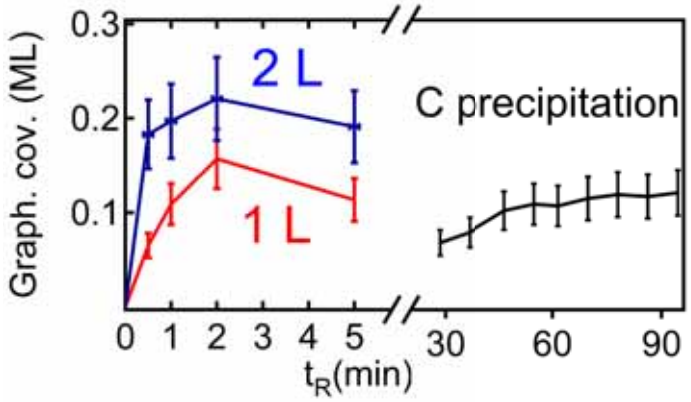

Figure 3.7: Graphene coverage as a function of t_R at D=1 (red), 2 (blue) L and T_R=500^{o}C. The black curve shows the slow increase of the graphene coverage of a sample maintained at 500^{o}C for up to 90 min due to carbon precipitation.

3.3 Post-annealing effect on graphene nanoislands

A common feature of the graphene islands prepared according to the method described above is the irregularity of sizes and shapes, which seems to be inherent to the graphene growth process. As observed in Figure 3.8, STM images obtained for preparations with identical T_R and D and different reaction times (t_R=2,20 min) further show that the island density, morphology, and size change with time . This motivated us to investigate systematically to what extent the average size and shape of the islands can be controlled through post-annealing, once the graphene reaction is complete. To systematically study the effect of a post-annealing process (step 3 in section 3.1), we systematically anneal graphene nanoislands at a temperature T_A during a time t_A. The graphene nanoislands are prepared with the method described in previous section (section 3.2) using T_R=500 ºC, to ensure graphene formation and avoid nickel carbide contamination, and t_R=5 min for complete graphene formation and a variable D. All result shown in this sections are obtained after the post-annealing process.

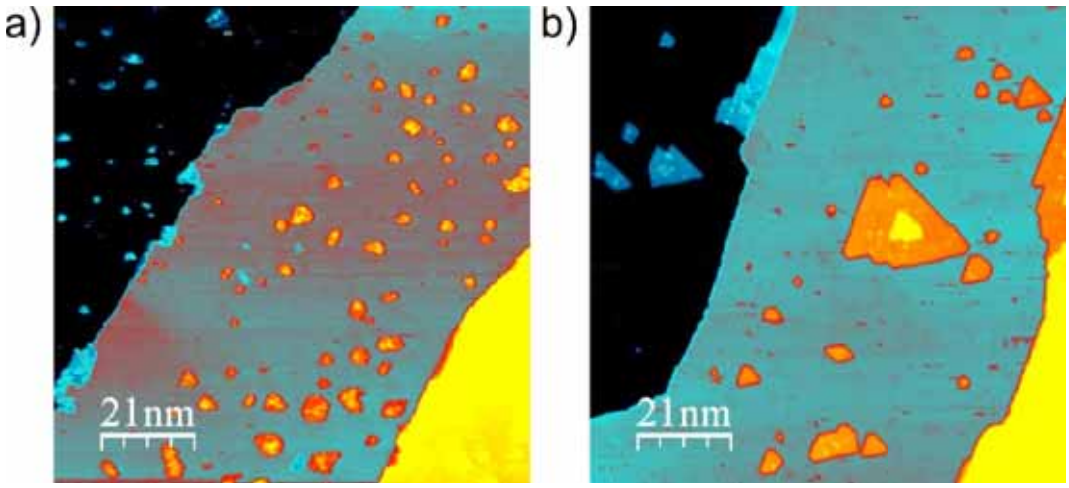

Figure 3.8: STM images of surface topography of two preparations with T_R=500 ºC, D=1 L and a) t_R=2 min and b) t_R=20 min.

Figure 3.9 shows the graphene coverage of a group of samples whit identical preparation parameters but varying T_A after the post-annealing process. We observe a decreasing of the final coverage as T_A increases. To counter this effect and obtain a moderated final graphene coverage, in the preparations used in next subsections the value of D is selected to be 1 L for samples with T_A<600 ºC and 2 L for samples with $T_A \geq$600 ºC. For the same reason, for samples with T_A<600 ºC we use t_A=20 min, while for $T_A \geq$600 ºC t_A=10 min is used.

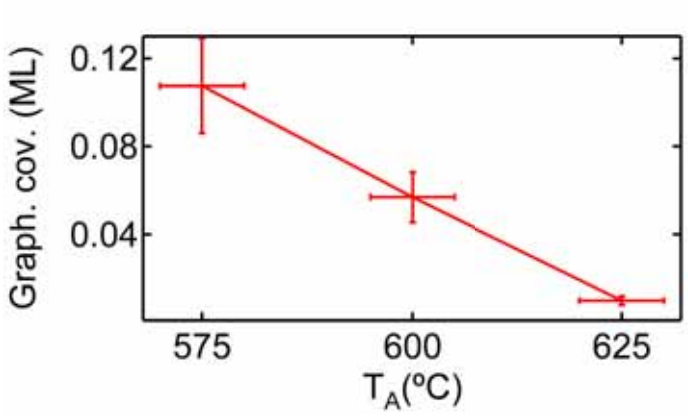

Figure 3.9: Graphene coverage as a function of T_A at constant D=2 L, t_R=1 min, T_R=500ºC, and t_A=10 min.

3.3.1 Shape selection

STM images in Figure 3.10 show that post-annealing induces significant changes of the island shape. Figure 3.10.a shows the results of the annealing at T_A=450 ºC and t_A=20 min. The edge of the islands remains irregular and no appreciable edge reorganization is observed. At this temperature the island structure is stable since no change in the island morphology is observed as a function of t_A. A major change of the average island morphology is observed for $T_A \geq$500 ºC. Figure 3.10.b shows that the larger islands assume a triangular shape after prolonged annealing at 500 ºC. Atomic resolution STM images further show that the triangle edges are now smooth zigzag edges oriented parallel to the $[11\bar{1}]$, $[\bar{1}11]$ and $[1\bar{1}1]$ directions of the Ni(111) surface, as explained in chapter 4. Upon increasing T_A to 600 ºC, we observe that most of the islands present truncated corners. The transition from equilateral to truncated triangles is associated to the different growth rates of the islands along the $[11\bar{2}]$ and $[\bar{1}\bar{1}2]$ high-symmetry directions of Ni(111) surface, in analogy with epitaxial metal systems [3, 4]. This process culminates in the formation of hexagonal islands as T_A reaches 650 ºC, as shown in Figure 3.10.d. We note that at this temperature the island density is very low owing to graphene lost to C migration into bulk nickel.

To statistically study the effect of the post-annealing process to the islands shape we define the shape parameter (Σ) the area of each island divided by its perimeter squared

$$\Sigma = \frac{\text{Area}}{\text{Perimeter}^2}$$

The value of Σ is determined by the shape of the island. As an example for equilateral triangles, hexagons and circles we have

$$\triangle \Rightarrow \quad \Sigma = \frac{a\frac{a}{2}\sin 60}{(3a)^2} = \frac{\sin 60}{18} \approx 0.048$$
$$\hexagon \Rightarrow \quad \Sigma = \frac{6a\frac{a}{2}\sin 60}{(6a)^2} = \frac{\sin 60}{12} \approx 0.072$$
$$\bigcirc \Rightarrow \quad \Sigma = \frac{\pi r^2}{(2\pi r)^2} = \frac{1}{4\pi} \approx 0.080$$

Statistic measurements have been done on samples with triangular (Figure 3.10.b) and hexagonal (Figure 3.10.d) islands. Figure 3.11 show the histogram of the shape parameter before (blue) and after (red) the post-annealing process. as observed in Figure 3.11.a reveals that most islands evolve from a round irregular shape ($0.048<\Sigma\leq 1/4\pi$) towards a triangular shape (Σ=0.048). Although the number of islands is not enough to collect a statistic comparable to the triangular case (T_A=500 ºC), Figure 3.11.b shows that after post-annealing at T_A=650 ºC the Σ distribution narrows around an intermediate value between triangles (Σ=0.048) and hexagons (Σ=0.072), representing hexagonal islands with unequal edge length.

3.3.2 Size distribution

As observed in Figure 3.8, the post-annealing process has a clear effect on the island size. To study its effect we perform statistical analysis on samples prepared with the optimal conditions for triangular (Figure 3.10.b; T_R=500 ºC, t_R=5 min, D=1 L, T_A=500 ºC and t_A=20 min.) and hexagonal (Figure 3.10.d; T_R=500 ºC, t_R=5 min, D=2 L, T_A=650 ºC and t_A=10 min.) graphene nanoislands, which is represented in Figure 3.12.

For preparation with T_A=500 ºC, the size distribution peaks at S=100 nm^2 while the number of smaller islands decreases significantly with respect to the islands observed before the post-annealing process (Figure 3.12.a). Although the number of islands is not enough to collect a statistic comparable to the T_A=500 ºC case, for T_A=650 ºC, we observe that all the small islands have completely disappeared during the post-annealing process and that the average size of the hexagons is about 130 nm^2 (Figure 3.12.b).

In both cases we find that the island size (S) follows a gamma distribution function

$$P(S) = \frac{\alpha^M}{\Gamma(M)} e^{-\alpha S} S^{M-1}$$

where Γ is the gamma function, α a scale parameter, M the shape parameter governing disorder, and the average island size is given by $\langle S\rangle = M/\alpha$ [1, 2]. The limit M=1, represents the exponential distribution expected for random events. Prior to post-annealing, we obtain M=1.2, indicating that the simple decomposition of

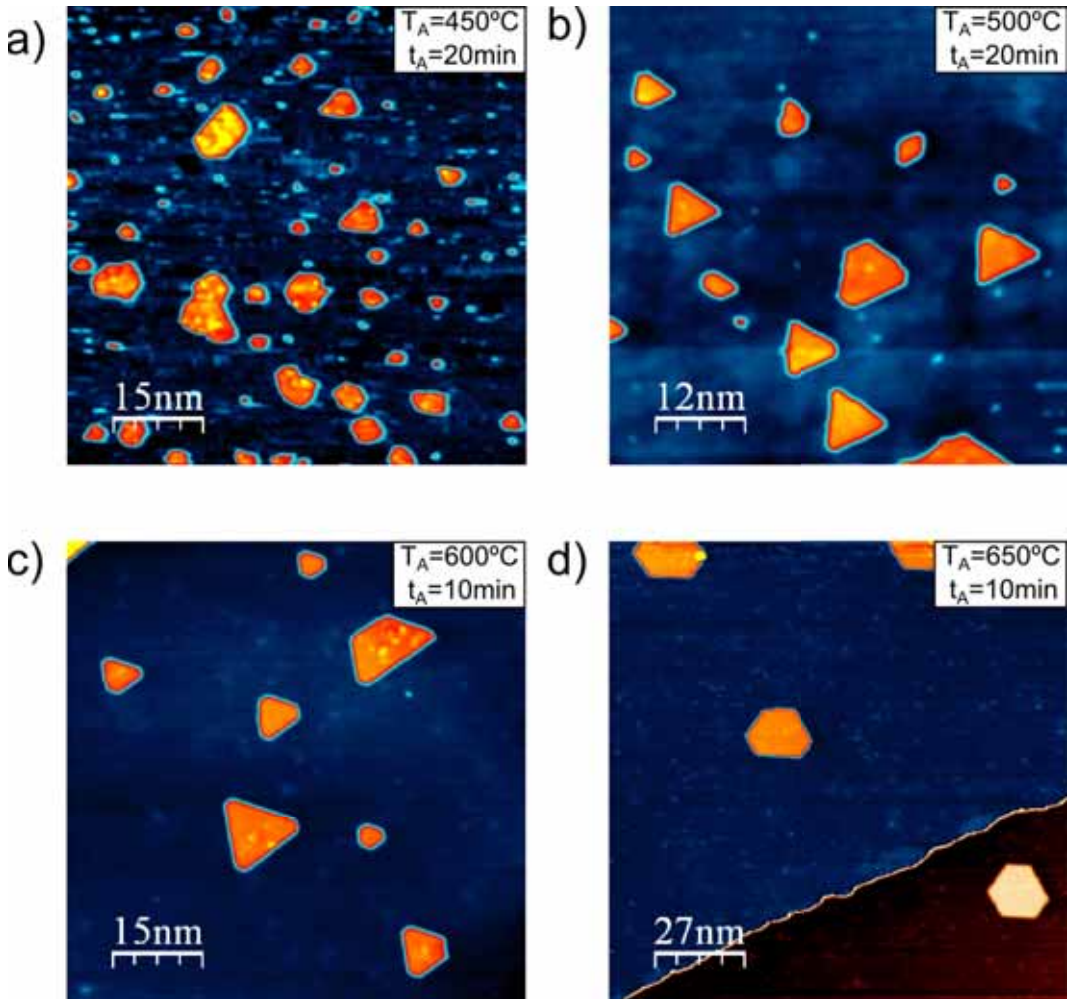

Figure 3.10: Size and shape of graphene nanoislands as a function of post-annealing. All samples are prepared with T_R=500 ºC and t_R=5 min. Representative STM images are shown for (a) D=1 L, T_A=450 ºC, and t_A=20 min. (b) D=1 L, T_A=500 ºC and t_A=20 min. (c) D=2 L T_A=600 ºC and t_A=10 min. (d) D=2 L, T_A=650 ºC and t_A=10 min. (e-h) Size and shape histograms of islands obtained before (blue sticks) and after (red stick) post-annealing at T_A=500 ºC (e,f) and T_A=650 ºC (g,h).

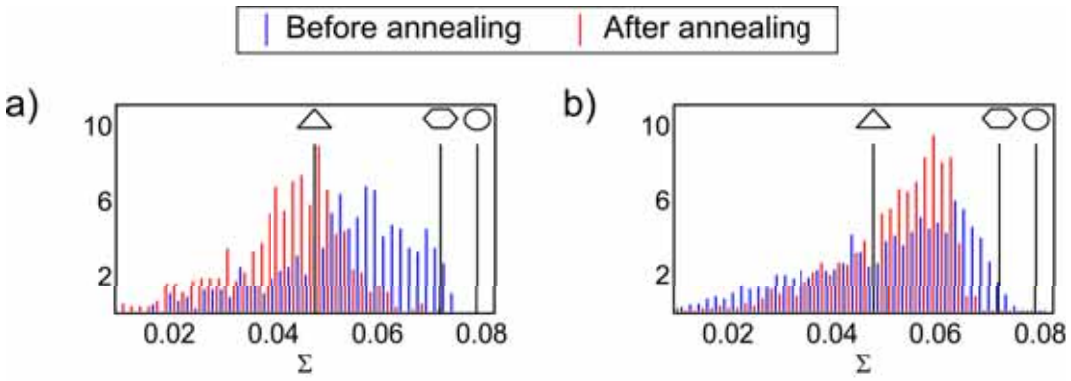

Figure 3.11: Shape parameter histograms of preparations before and after the post-annealing treatment. Parameters used for the preparations are a) T_R=500 ºC, t_R=5 min, D=1 L, T_A=500 ºC and t_A=20 min. b) T_R=500 ºC, t_R=5 min, D=2 L, T_A=650 ºC and t_A=10 min.

propene does not lead to the self-assembly of graphene islands with a preferred size. Following post-annealing, we find that the distribution changes from exponential to a peaked function with increasing T_A, leading to M=2.8±0.3 at T_A=650 ºC and a 10-fold increase of the average island size from about 10 to 120 nm^2.

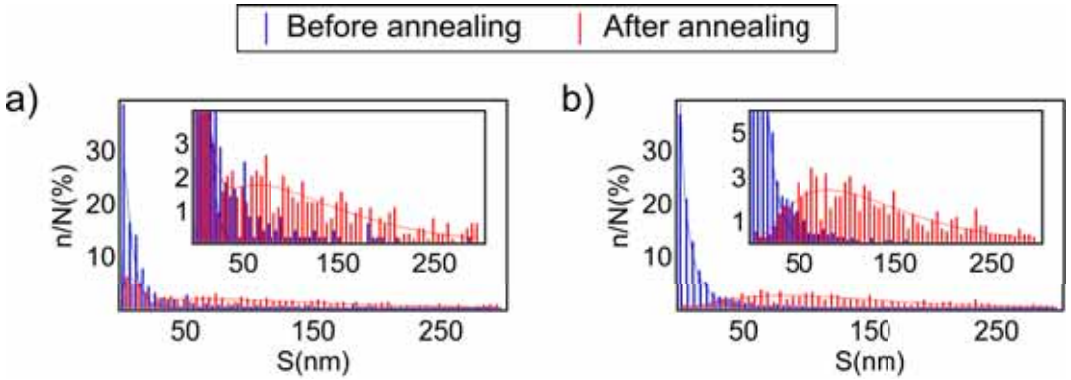

Figure 3.12: Size distribution histograms of preparations before and after the post-annealing treatment. Parameters used for the preparations are a) T_R=500 ºC, t_R=5 min, D=1 L, T_A=500 ºC and t_A=20 min. b) T_R=500 ºC, t_R=5 min, D=2 L, T_A=650 ºC and t_A=10 min.

3.4 Summary

Epitaxial graphene islands grown on close-packed metal surfaces by decomposition of hydrocarbons usually present broad shape and size distributions [1-4]. Inducing the self-assembly of graphene nanoislands appears to be particularly difficult due to

the need of optimizing several contrasting processes, such as hydrocarbon pyrolysis against desorption, graphene against carbide formation, edge and surface diffusion of C atoms against bulk diffusion. To summarize our systematic investigation of the growth parameters governing the formation of graphene on Ni(111), we found that the reaction temperature, dose, and post-nucleation annealing of the substrate must be sequentially optimized in order to minimize the width of the size and shape distribution of nanosized graphene islands. We developed a method to grow relatively large graphene nanoislands of selected shape on Ni(111). This method is based on the pre-adsorption of a fixed dose of propene on nickel at RT, followed by heating up to 500 ºC, which yields the maximum amount of graphene per dose unit but irregular islands. Lower reaction temperatures favor the formation of Ni_2C , whereas larger temperatures favor fast propene desorption. Annealing time and dose determine the amount of graphene formed. The graphene coverage increases proportionally to the dose up to D=5 L, after which it saturates to about 0.5 ML. In the final post-annealing step, irregular graphene islands undergo a thermal shape selection process, while the smallest islands vanish due to ripening and C migration into the bulk. We showed that, by varying the annealing temperature between 500 and 650 ºC, we can induce the formation of islands larger than 100 nm^2 with either triangular or hexagonal shape. These islands present good structural quality and straight zigzag edges.

4 Island structure

The lattice of free-standing graphene and the Ni(111) surface are known to have a small mismatch. Due to this coincidence the graphene/Ni(111) system presents a 1x1 stacking [76]. Gamo et. al. [85] studied the stacking of graphene on Ni(111) by means of LEED. The 3m symmetry observed in the LEED pattern observed in their studies indicated that carbon atoms are situated on the symmetry points of the Ni(111) surface. These symmetry points are the "on-top" sites, located on the topmost nickel atoms, and one of the two hollow sites corresponding to hcp and fcc stacking, located on top of the 2nd and 3rd layer nickel atoms. Graphene has a honeycomb structure composed by two sub-lattices. Gamo et. al. considered thee possible stacking structures: top-fcc, top-hcp and fcc-hcp. They conclude that the top-fcc structure is the most likely in accordance to their LEED intensity experiments. DFT calculations performed by Lahiri et. al. [77] show the lowest energy configuration for the top-fcc stacking, although the increase of the system energy corresponding to top-hcp is only 12 meV/atom . Experimentally both stackings where observed by STM [77]. The fcc-hcp structure is energetically unstable and no experimental evidence of its existence has been found. Kozlov et. al. expand the study of graphene stacking on Ni(111) with three more possibilities, called bridge-top, brigde-fcc and bridge-hcp. In their results bridge-top stacking is the lowest energy stacking [86], with a small energy decrease from top-fcc stacking.

Besides the stacking configuration, another factors that determines the electronic properties of graphene is the presence and type of edges in nanostructures [45, 46, 47, 48, 49]. Graphene edges can be divides in two main groups, being chiral and achiral edges. Achiral edges have been observed to dominate over chiral edges after Joule heating [87]. Two types of achiral edges exist, named armchair and zigzag edges. Theoretical calculations show that armchair edges are stable, while zigzag edges are metastable and reconstruct spontaneously into pentagon-heptagon configuration [88]. The stabilization of zigzag edges can be achieved by substrate interaction. For that reason epitaxial growth of graphene nanoislands is a good method to produce and study zigzag edges.

Graphene nanoislands have been obtained epitaxially on Ir(111) [57], Ru(0001) [58], Co(0001) [48] and Cu(001) [59]. Graphene nanoislands on Ni(111) are specially interesting for two reasons: first, the small lattice mismatch that produces the 1x1 stacking avoid any superstructure such as Moiré pattern and the islands are more homogenous; and second, the magnetic properties of nickel and its interaction with the graphene nanoislands could result in a fixation of the net magnetic moment

predicted for triangular graphene nanoislands with zigzag edges [50].

In this chapter we present an structural study of graphene nanoislands on Ni(111). The islands present zigzag edges, which can be divide in hollow (zz_h) and top (zz_t) edges depending on the position of the outer carbon atom with respect to the substrate. While zz_h edges are found to be stable at RT due to the effect of the substrate, zz_t edges reconstruct into pentagon-heptagon structure ($zz_t(57)$) as in the case of free-standing graphene. The stacking with the substrate of the islands depends strongly on the edges and can adopt different configurations to minimize the edge energy. As we show in the following sections, triangular graphene nanoislands are have top-fcc stacking with zz_h edges while hexagonal graphene nanoislands have both types of edges, zz_h and $zz_t(57)$. The proposed structures are supported by DFT calculations. Three different Moiré patters are observed in some graphene nanoislands attributed to different angle rotations of the graphene lattice respect to the substrate.

4.1 Experimental details

All the experiment described in this chapter were performed in the room temperature experimental setup described in detail in subsection 2.3.1. A Ni(111) single crystal was used to grow graphene nanoislands using the procedure described in **??**.

4.2 Stacking and edge types of graphene on Ni(111)

In this section we introduce the possible stacking configurations of graphene on Ni(111) . We will also discus the different types of graphene edges depending on the edge direction and graphene stacking.

4.2.1 Atomic structure of nickel crystal and Ni(111) surface

Nickel has a face centered cubic (fcc) atomic structure. The Ni(111) surface presents a hexagonal structure as illustrated in Figure 4.1.a. The nickel atoms at the (111) surface are separated by 249 pm [75]. The crystal structure can be understood as multiple planes of (111) surfaces displaced by a distance d/3 in the $\left[11\bar{2}\right]$ direction, being d the distance between two atoms in this crystallographic direction equal to 431 pm (Figure 4.1.b). Figure 4.1.c illustrates the atomic position of nickel atoms when observing the crystal in the direction perpendicular to the (111) surface.

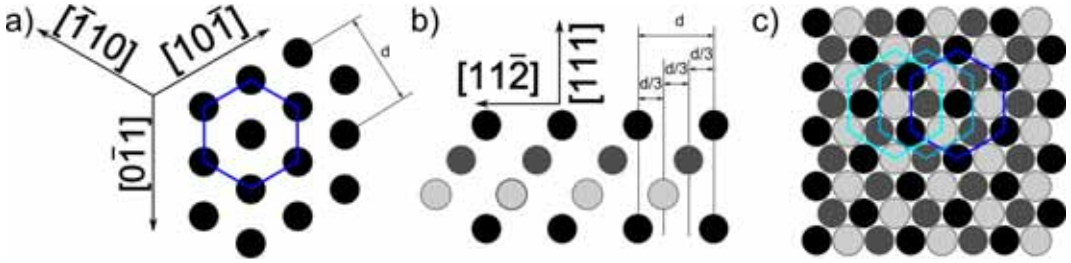

Figure 4.1: a) Atomic structure of the Ni(111) surface. b) Atomic structure of the nickel crystal in a plane perpendicular to the surface. c) Position of the nickel atoms of different layers on the Ni(111) surface.

4.2.2 Atomic structure of graphene

To study the atomic structure of graphene we will first consider the case of free-standing graphene. Free-standing graphene is a 2D crystal of carbon atoms with honeycomb structure kept together by sp2 bonds. As seen in Figure 4.2.a, honeycomb structure consist of an hexagonal lattice with a basis composed of two carbon atoms (A and B). The distance between carbon atoms in freestanding graphene is 142 pm and the lattice parameter is 246 pm, which is very similar to the interatomic distance in the Ni(111) surface. Figure 4.2.b shows the atomic structure of the Ni(111) surface at scale for comparison.

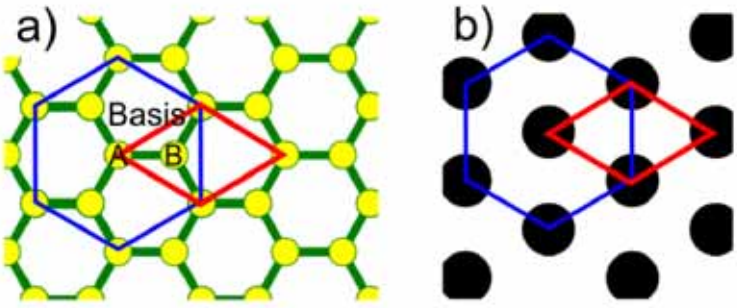

Figure 4.2: a) Graphene structure, composed of atoms belonging to two sublattices A and B. b) Ni(111) structure represented at the same scale.

4.2.3 Graphene stacking with the substrate

When placing a graphene sheet on a metal surface the final structure of the system will strongly depend on the graphene interaction with the substrate. In this subsection we introduce the possible structures of graphene on a Ni(111) surface.

4.2.3.1 1x1 stacking configuration

The absence of a Moiré pattern (see subsubsection 4.2.3.2) in the vast majority of graphene nanoislands on Ni(111) indicates a pseudomorphic alignment of the graphene lattice with the nickel substrate. Several 1x1 stacking structures have been proposed. Gamo et. al. [85] proposed three stacking configurations called top-fcc (Figure 4.3.a), top-hcp (Figure 4.3.b) and fcc-hcp (Figure 4.3.c). In their experiments the top-fcc stacking was proposed to be the most common configuration. Later, Lahiri et. al.[77] found a coexistence of two stacking configurations that they identify to be top-fcc and top-hcp. Their DFT calculations predict a slight difference in energy for top-fcc and top-hcp, with top-fcc being the most stable. The fcc-hcp structure was found to be unstable. Kozlov et. al. performed DFT calculation on six stacking configurations [86], the three already defined by Gamo et. al. and three more called bridge-top (Figure 4.3.d), bridge.hcp (Figure 4.3..e) and bridge-fcc (Figure 4.3.f). They found bridge-top stacking to be the more energetically favorable stacking configuration. The energy difference calculated between bridge-top and top-fcc configurations was less than 0.5 $kJ \cdot mol^{-1}$. Surprisingly, all other stacking configurations, including top-hcp, were found to be unstable, in contradiction with the results of Lahiri et. al. Although there is no agreement with respect the minimum energy stacking, some configurations as fcc-hcp, bridge-hcp and bridge-fcc are considered unstable in all publications. For that reason, we will consider only top-fcc, top-hcp and bridge-top stacking in our analysis.

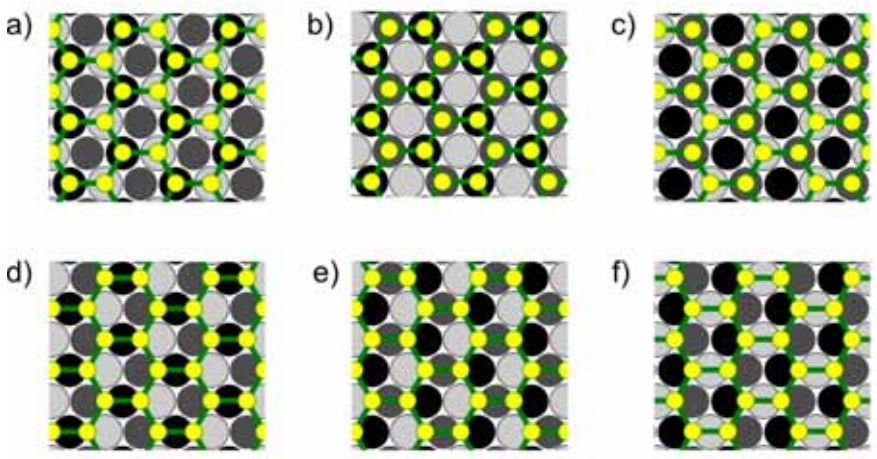

Figure 4.3: Graphene stacking structures on Ni(111) in case of perfect lattice alignment. The stacking configurations are called a) top-fcc b) top-hcp c) fcc-hcp d) bridge-top e) bridge-hcp f) bridge-fcc. Nickel atoms are represented as black (1^{st} layer) dark grey (2^{nd} layer) and light grey (3^{rd} layer) spheres. Carbon atoms are represented as yellow spheres

4.2.3.2 Moiré pattern as a measure of graphene orientation

Although very rare, Moiré patterns are observed for certain preparations on graphene on Ni(111)[89, 39]. In this subsubsection introduce the origin of Moiré patterns and present the results obtained for graphene nanoislands on Ni(111).

Graphene grown on metals normally presents a moiré pattern determined by the mismatch between the lattice parameters of graphene and the substrate, and the lattice orientation with respect to the substrate. A Moiré pattern is an interference pattern caused by the superposition of two periodical lattices with different periodicity or different orientation. In the case of graphene on Ni(111) the lattice parameters are almost equal hence the Moiré patterns formed by the two lattices are due to a misalignment. Figure 4.4 illustrates the effect of superposing two lattices with identical lattice parameter. When a rotation is introduced to the system, a Moiré patters in formed. The Moiré has a periodicity and a inclination that depends on the misalignment of the superposed lattices.

Given a certain 2D Bravais lattice $\mathbf{R} = n_1\vec{a_1} + n_2\vec{a_2}$ where n_i are integers and a_i are the lattice vectors, we define the reciprocal lattice as a set of vectors $\mathbf{K} = m_1\vec{k}_1 + m_2\vec{k}_2$ that fulfills the condition

$$e^{i\mathbf{K}\cdot\mathbf{R}} = 1 \tag{4.1}$$

which implies

$$\left|\vec{k_i}\right| = \frac{2\pi}{|\vec{a_i}|}\, i = 1, 2\,. \tag{4.2}$$

Generally, the periodicity and orientation of a Moiré pattern is given by [57]

$$\mathbf{K}_M = \mathbf{K}_\Theta - \mathbf{K}_\Lambda \tag{4.3}$$

where $\mathbf{K}_M$, $\mathbf{K}_\Theta$, and $\mathbf{K}_\Lambda$ are the reciprocal lattice vectors of the Moiré, lattice Θ and lattice Λ. In our case, lattice Θ is the nickel surface ($\mathbf{K}_{Ni}$) and lattice Λ is the graphene ($\mathbf{K}_G$). If we consider the reciprocal vectors separately, Equation 4.3 can be written as

$$\vec{k}_{i,M} = \vec{k}_{j,Ni} - \vec{k}_{k,G} \quad i, j, k = 1, 2\,. \tag{4.4}$$

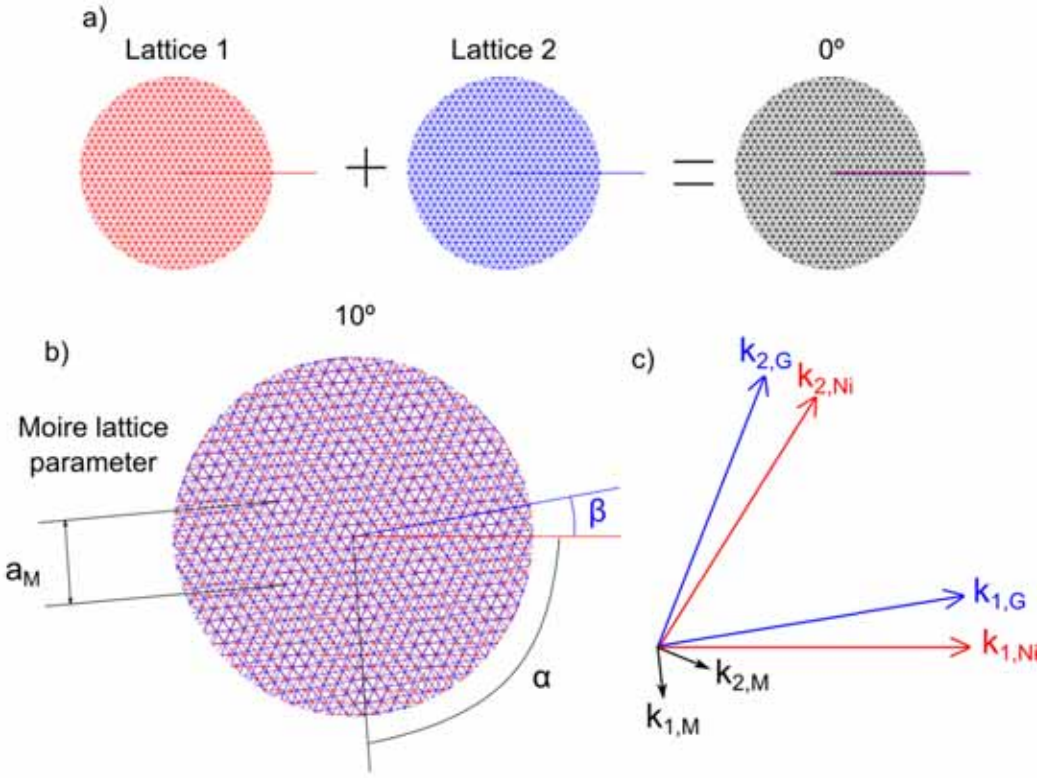

Figure 4.4: Origin of a Moiré pattern. a) Two identical lattices superposed with identical structure and orientation do not result in a Moiré pattern. b) When one lattice is rotated by an angle β a Moiré pattern is created, which has a periodicity a_M and a rotation α. c) The reciprocal vectors of the Moiré pattern are the subtraction of the reciprocal vectors of the original lattices.

The nickel surface, graphene, and the Moiré patterns have hexagonal structure, for these reason the calculations will be equivalent for both reciprocal vectors. To simplify the notation we remove the i sub-index. The reciprocal vector can be expressed as

$$\begin{aligned} \vec{k}_{1,M} = \vec{k}_M &= \left|\vec{k}_M\right| (\cos\alpha, \sin\alpha) \\ \vec{k}_{1,Ni} = \vec{k}_{Ni} &= \left|\vec{k}_{Ni}\right| (1, 0) \\ \vec{k}_{1,G} = \vec{k}_G &= \left|\vec{k}_G\right| (\cos\beta, \sin\beta) \end{aligned} \tag{4.5}$$

where α is the angle between $\vec{k}_{Ni}$ and $\vec{k}_M$ and β is the angle between $\vec{k}_{Ni}$ and $\vec{k}_G$.

By substituting Equation 4.5 in Equation 4.3 we have

$$\left.\begin{aligned}\left|\vec{k}_M\right|\cos\alpha &= \left|\vec{k}_{Ni}\right| - \left|\vec{k}_G\right|\cos\beta \\ \left|\vec{k}_M\right|\sin\alpha &= -\left|\vec{k}_G\right|\sin\beta\end{aligned}\right\}. \tag{4.6}$$

By squaring each side

$$\begin{aligned}\left.\begin{aligned}\left|\vec{k}_M\right|^2\cos^2\alpha &= \left|\vec{k}_{Ni}\right|^2 + \left|\vec{k}_G\right|^2\cos^2\beta - 2\left|\vec{k}_{Ni}\right|\left|\vec{k}_G\right|\cos\beta \\ \left|\vec{k}_M\right|^2\sin^2\alpha &= \left|\vec{k}_G\right|^2\sin^2\beta\end{aligned}\right\} \\ \left|\vec{k}_M\right|^2\left(1-\left|\vec{k}_G\right|^2\sin^2\beta\right) &= \left|\vec{k}_{Ni}\right|^2 + \left|\vec{k}_G\right|^2\cos^2\beta - 2\left|\vec{k}_{Ni}\right|\left|\vec{k}_G\right|\cos\beta \\ \left|\vec{k}_M\right|^2 &= \left|\vec{k}_{Ni}\right|^2 + \left|\vec{k}_G\right|^2 - 2\left|\vec{k}_{Ni}\right|\left|\vec{k}_G\right|\cos\beta\,.\end{aligned} \tag{4.7}$$

In the case of graphene on Ni(111), the lattice parameters have a difference of 1% [75]. Since $\left|\vec{k}_{Ni}\right| \approx \left|\vec{k}_G\right|$ we define

$$\left|\vec{k}_{eff}\right| = \frac{2\pi}{a_{eff}} = \frac{2\pi}{\frac{a_{Ni}+a_G}{2}} = \frac{2}{\frac{1}{\left|\vec{k}_{Ni}\right|}+\frac{1}{\left|\vec{k}_G\right|}} = \frac{2\left|\vec{k}_{Ni}\right|\left|\vec{k}_G\right|}{\left|\vec{k}_{Ni}\right|+\left|\vec{k}_G\right|} \approx \left|\vec{k}_{Ni}\right| \approx \left|\vec{k}_G\right| \tag{4.8}$$

where a_{eff} is the median of both lattice parameters. By substituting $\left|\vec{k}_{Ni}\right|$ and $\left|\vec{k}_G\right|$ by $\left|\vec{k}_{eff}\right|$ in Equation 4.7 we obtain

$$\cos\beta = 1 - \frac{\left|\vec{k}_M\right|^2}{2\left|\vec{k}_{eff}\right|^2} \tag{4.9}$$

With this expression we can obtain the rotation angle of the Moiré with respect to the graphene lattice more precisely than by directly measuring it from the STM images. To obtain the rotation of the graphene lattice with respect to the nickel surface we only have to substitute Equation 4.9 in the first Equation 4.7

$$\begin{aligned}\left|\vec{k}_M\right|\cos\alpha &= \left|\vec{k}_{eff}\right| - \left|\vec{k}_{eff}\right|\left(1-\frac{\left|\vec{k}_M\right|^2}{2\left|\vec{k}_{eff}\right|^2}\right) \\ \left|\vec{k}_M\right|\cos\alpha &= \frac{\left|\vec{k}_M\right|^2}{2\left|\vec{k}_{eff}\right|} \\ \cos\alpha &= \frac{\left|\vec{k}_M\right|}{2\left|\vec{k}_{eff}\right|}\end{aligned} \tag{4.10}$$

4.2.4 Edge configuration and symmetries

When considering nanostructured graphene the edges acquire an increasing importance on its properties and can determine the stacking with the substrate [90]. In this subsection we define the different graphene edge types as well as their geometry when placed on a Ni(111) substrate.

4.2.4.1 Edges of free-standing graphene

On free-standing graphene two types of edges are identified, the so called armchair and zigzag edges. As illustrated in Figure 4.5, armchair edges own their name to their shape. They are composed by two atoms at the outer part of the edge and two in the inner part. Zigzag edges have one atom in the outer part and one in the inner part. Both, armchair and zigzag edges, have sixfold symmetry. There is a deviation of 30º between armchair and zigzag edges, hence we can change from one to the other by rotating the edge direction by 30º.

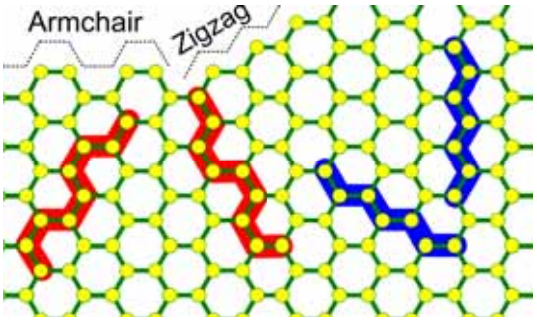

Figure 4.5: Armchair and zigzag edges of free-standing graphene. Red (blue) lines represent alternative directions with armchair (zigzag) edges.

4.2.4.2 Edge of top-fcc stacking graphene

The different edge types of graphene on Ni(111) are shown in Figure 4.6. Graphene edges are illustrated in an ordered way, when moving leftwards the edge orientation is rotated by 30º with respect to the previous one, when moving downwards the edge orientations is rotated by 120º. Zigzag graphene edge placed on Ni(111) substrate follow different crystal directions $(1\bar{1}0)$, $(\bar{1}10)$, $(10\bar{1})$, $(\bar{1}01)$, $(01\bar{1})$ and $(0\bar{1}1)$. Armchair graphene edges placed on Ni(111) follow the crystal directions $(11\bar{2})$, $(\bar{1}\bar{1}2)$, $(1\bar{2}1)$, $(\bar{1}2\bar{1})$, $(\bar{2}11)$, and $(2\bar{1}\bar{1})$.

Zigzag edges loose the sixfold symmetry when placed on Ni(111) with top-fcc stacking. They can be dived in two groups, called zigzag hollow (zz_h) and zigzag top (zz_t). The zz_h edges, marked with a blue background, have the outer carbon atom placed on top of the 3rd (light grey) layer nickel atom, while the inner carbon atom is on top of the 1st (black) layer nickel atom. In contrast, Zz_t edges, marked with a yellow background, have the outer carbon atom placed on top of the 1st layer nickel atom, while the inner carbon atom of the edge is on top of the 3rd layer nickel atom.

Both zigzag edges types have threefold symmetry, and are rotated by 60º between them. The energy of each zigzag edge type differ significantly, as we will show below.

On the other hand, the symmetry of the armchair edges (green background in Figure 4.6) does not change when placed on Ni(111). Although armchair edges also divide in two groups with threefold symmetry, the two groups have the same structure with a different chirality. For this reason we will generally refer the two groups simply as armchair edges (ac).

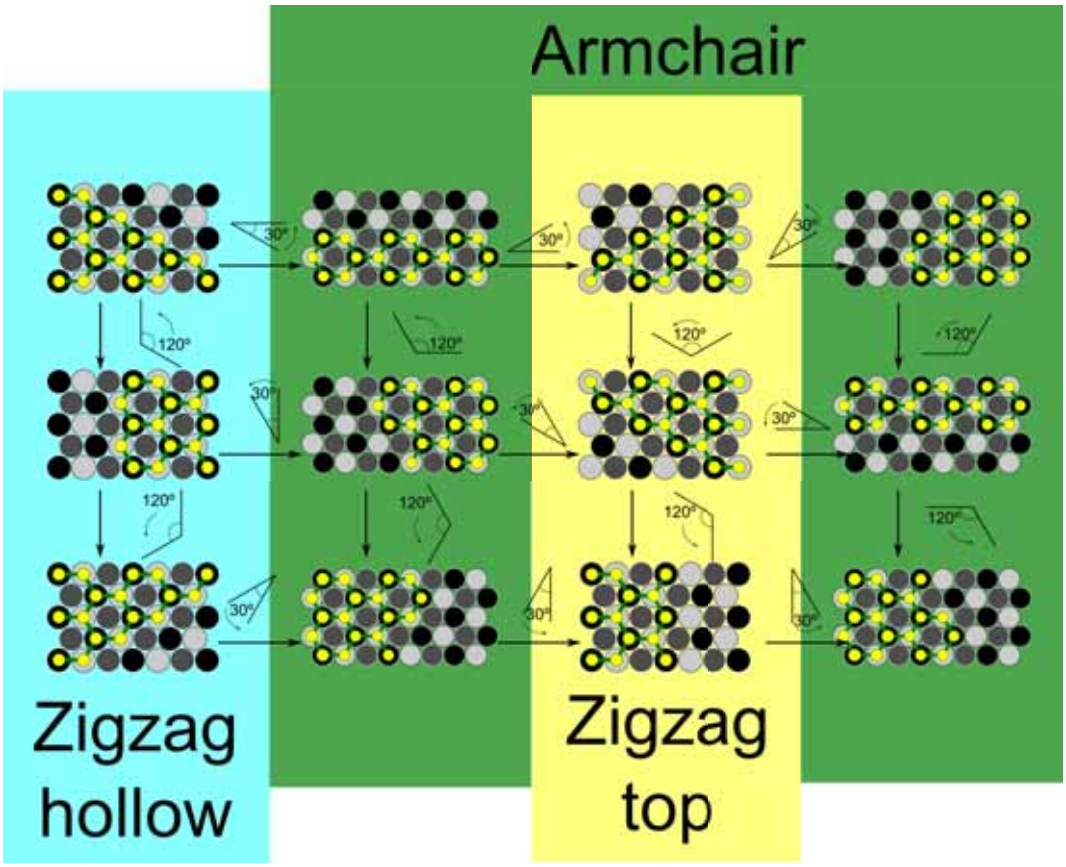

Figure 4.6: Graphene edges on Ni(111) with top-fcc stacking. Armchair edges are represented on a green background. Zigzag hollow (zz_h) edges are represented on a blue background. Zigzag top (zz_t) edges are represented on a yellow background.

4.2.4.3 Edge of top-hcp stacking graphene

The top-fcc and top-hcp stacking have the same symmetry. For this reason the resultant edge symmetries of graphene with top-hcp stacking are the same as in the case of top-fcc stacking. Figure 4.7 illustrates the structure of zz_t, zz_h and ac edges. The only difference with respect to top-fcc edges is the position of the "hollow" atom, which is situated on top of the 2nd layer nickel atom (dark grey) in top-hcp stacking.

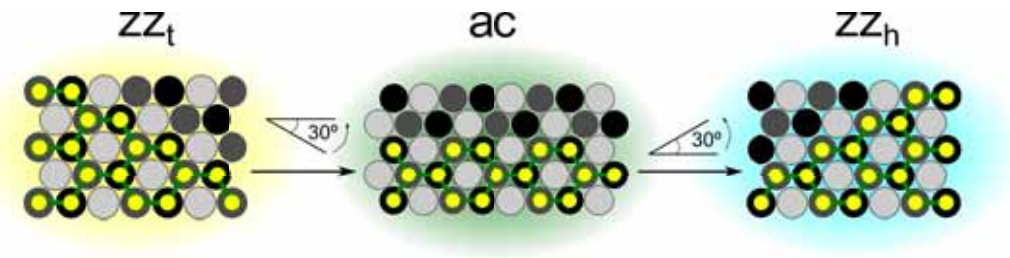

Figure 4.7: Graphene edges on Ni(111) with top-hcp stacking. Zz_t (yellow background), ac (green background)and zz_h (blue background) .

4.2.4.4 Edge of bridge-top stacking graphene

Graphene edges on Ni(111) with bridge-top stacking have different symmetries and atomic structures than in the cases of top-fcc and top-hcp stackings. Figure 4.8 shows all types of graphene edges, the color contour identifies edges with the same atomic structure (some times with different chirality). Zigzag edges type are named as zz_α (red contour), zz_β (blue contour) and zz_γ (purple contour). While both zz_γ edges are equal and have twofold symmetry, the two pair of edges grouped in zz_α and zz_β types have the same structure and different chirality. Armchair edges are named as ac_α (green contour), ac_β (yellow contour) and ac_γ (black contour). All three ac edges types are formed with pairs of edges with the same atomic structure and different chirality.

4.3 Triangular graphene nanoislands

Triangular graphene nanoislands were grown using the procedure described in detail in chapter 3. The parameters used to grow the triangular graphene nanoislands are D=1 L, T_R=500 ºC, t_R=5 min, T_A=500 ºC and t_A=20 min. In this section we discus the atomic structure of the islands, including their stacking with the substrate and edge configuration. The most stable configuration is experimentally and theoretically determined to be top-fcc stacking with zz_h edge type. First we will report experimental evidences and after that present DFT calculations to support the experimental result.

4.3.1 Experimental results

4.3.1.1 Possible structures of triangular graphene nanoislands on Ni(111)

When considering the structure of a graphene nanoisland on Ni(111), both, the stacking and edge type, have a determinant influence on its final shape. In nanostructured systems, the edge energy is an important part of the total energy and can

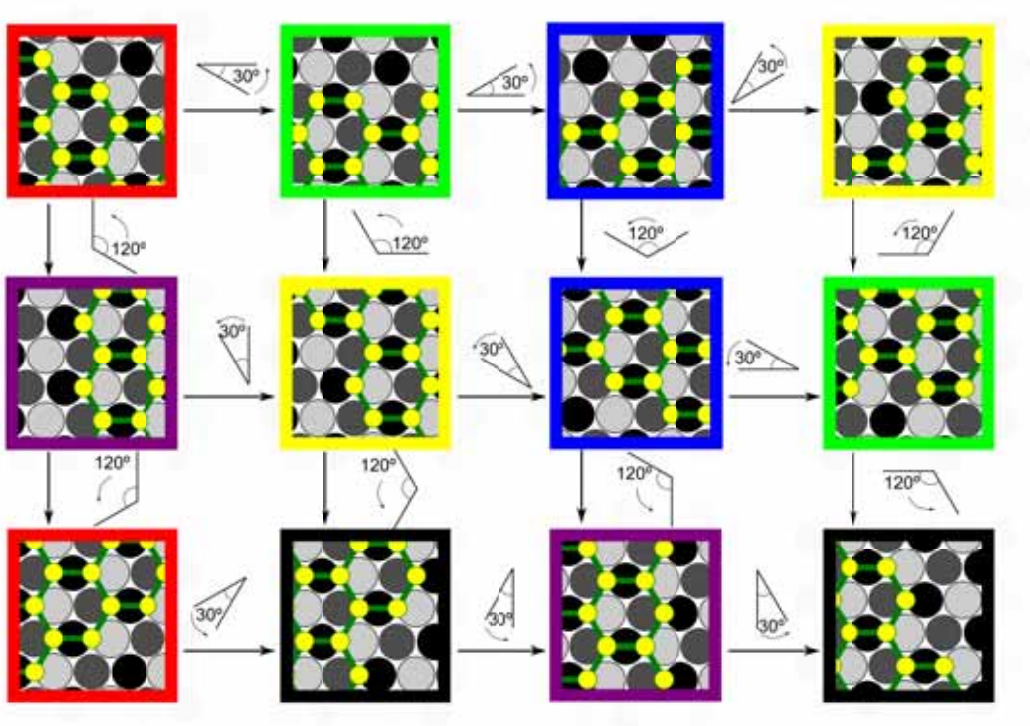

Figure 4.8: Graphene edges on Ni(111) with bridge-top stacking. Three types of zigzag edges named zz_α (red contour), zz_β (blue contour) and zz_γ (purple contour) and three types of armchair edges named ac_α (green contour), ac_β (yellow contour) and ac_γ (black contour).

affect the final stacking with the substrate. For this reason all possible combinations of stacking and edge have to be considered in order to determine the possible system structures.

Figure 4.9 shows the structure of triangular graphene nanoislands with top-fcc, top-hcp and bridge-top stacking. Other stackings, such as fcc-hcp, bridge-fcc, and bridge-hcp, have not been considered since it is unlikely that the energy cost can be compensated by most stable edge configuration. The islands presented here are considered to have zigzag edges, since no triangular graphene nanoisland with armchair edges has been observed in all the experiments realized.

Triangular graphene nanoislands with bridge-top stacking are composed of one zz_γ edge and two zz_α (or zz_β) edges. Considering the edges structure we would expect different properties for zz_γ and zz_α (or zz_β) edges, such as stability, growth rate, reactivity. However, there is no statistically relevant variation of the length of one edge with respect to the others in triangular islands and they posses a marked threefold symmetry, for that reason we discard bridge-top stacking as a possible candidate.

However triangular graphene nanoislands with top-fcc and top-hcp stacking have

edges of the same type, as observed in Figure 4.9. However, the orientation of a triangular graphene nanoisland depends on the combination of the stacking with the edge type. For example, islands with top-fcc stacking and zz_h edges have the same orientation than islands with top-hcp stacking and zz_t edges. Changing either the stacking or the edge type alone results in a change of the orientation of the triangular graphene nanoisland.

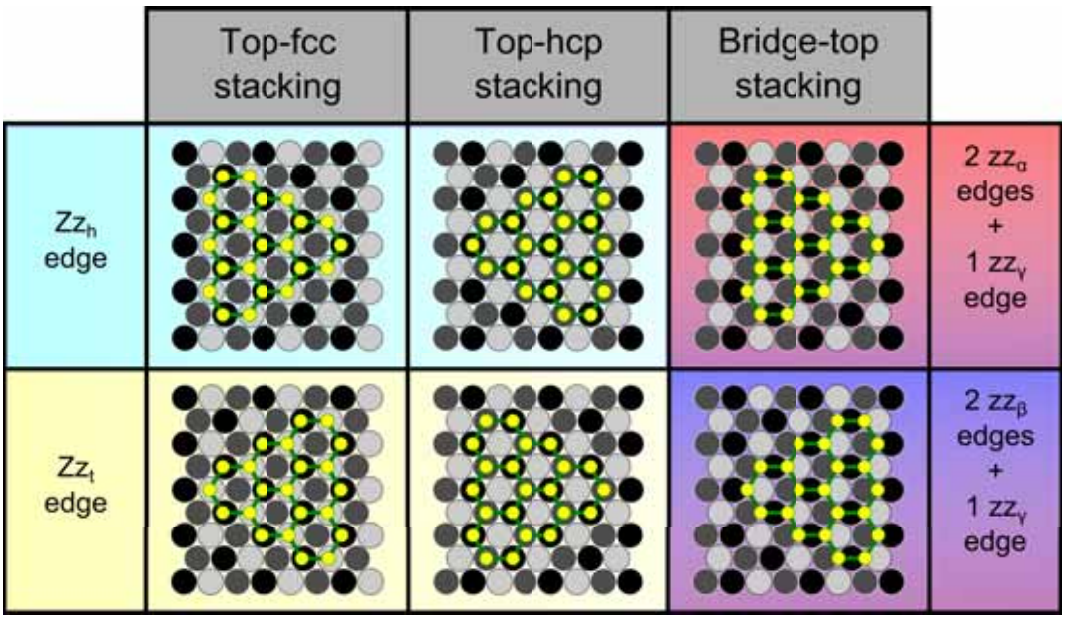

Figure 4.9: Structure of triangular graphene nanoislands depending on the stacking with the substrate and the edges type.

4.3.1.2 Edge influence on stacking and most stable configuration

As observed in Figure 4.10.a, most triangular graphene nanoislands grown on Ni(111) have the same orientation, indicating that they have the same stacking and edge configuration. However, when observing the sample in more detail (Figure 4.10.b), we observe some graphene nanoislands pointing to the opposite direction (marked with arrows). This change in orientation could be explained by a change in stacking or edge type. All triangular graphene nanoislands with inverted orientation observed have a small size, below 10 nm^2. Generally, the effect of the edge in the system energy is higher for small systems, which indicates that islands with inverted orientation maintain the edge type and change their stacking.

Atomically resolved STM images were obtained on a triangular graphene nanoisland with the most common orientation. Figure 4.11.a shows a derivative STM image obtained from the topography shown in the inset. The derivative image allows us to better observe the atomic structure of the system. Figure 4.11.b shows an enlarged area of the derivative image with a superposed graphene lattice and a

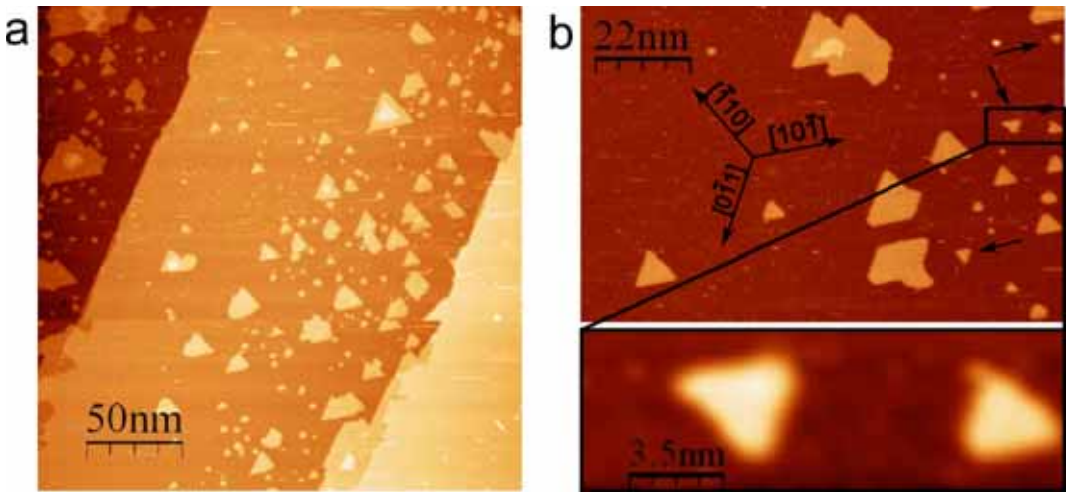

Figure 4.10: a) STM image of triangular graphene nanoislands on Ni(111) showing a preferred orientation of the triangular graphene nanoislands. b) STM image of triangular graphene nanoislands showing small nanoislands with opposite orientation (marked with arrows).

contour plot for illustrative purposes. In the left part of the image we can identify the atomic structure of graphene, in where the carbon atoms of both sublattices are observed forming the characteristic honeycomb structure..We can observe that the nanoisland show zigzag edge with no defects and that the carbon atoms situated at the outer part of the edge (red points) are situated on hollow positions on the Ni(111) surface, hence the edge are zz_h type. On the graphene structure, we observe that the carbon atoms marked with the blue points are brighter than the ones marked with red points. The "blue" atoms are situated on top of the 1st layer nickel atoms as observed on the nickel surface, hence are situated on a top position. Lahiri et. al. deduce in a indirect way than the brighter atoms correspond to hollow positions[77]. This statement is in contradiction with our results, but the evidence of the atomic resolved STM images is beyond doubt.

Figure 4.11.c shows a scheme of the structure of the system. For the zz_h edge type, the carbon atoms situated at the outer edge have the dandling bonds pointing to 1st layer nickel atoms situated close to them, which may stabilize the sp2 bond. On the contrary, zz_t edge type would have the dangling bonds pointing to a hollow position, making more difficult to saturate them and increasing the energy of the edge.

In conclusion, the majority of the islands have a top-fcc stacking because it reduce total system energy for complete monolayers (see subsubsection 4.2.3.1). Those islands that point to the opposite direction have a top-hcp stacking, what increase a little the system energy compared with the top-fcc stacking, but is compensated by the lower energy of the dominant edge type.

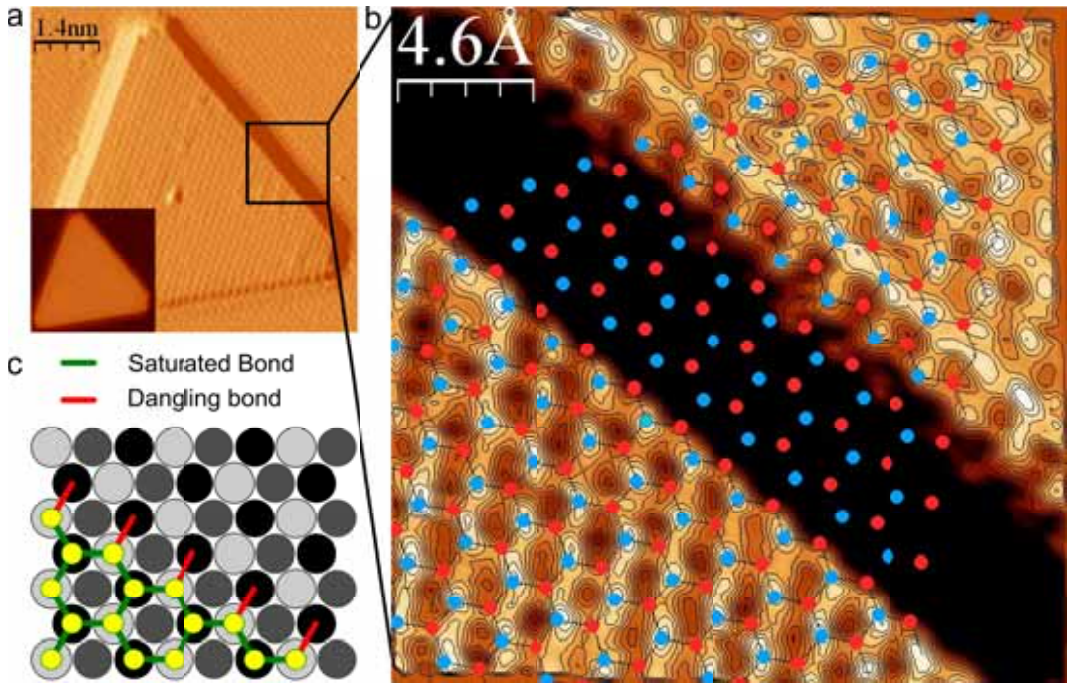

Figure 4.11: a) Derivative STM image of a triangular graphene nanoisland with the most common orientation. Original STM image is showed in the small inset. b) Zoomed image with a topographic contour and a superposed lattice to show the stacking of the graphene nanoislands with the substrate. c) Proposed model for the stacking and edge type of triangular graphene nanoislands. The model is top-fcc stacking with zz_h edges.

4.3.2 DFT calculation on triangular graphene nanoislands configuration

The coexistence of triangular graphene nanoislands with opposite orientation indicates that two types of islands coexist. A change in the stacking configuration of the island or the edge type produce a change in the orientation. Although the small size of the inverted islands indicate that the difference is probably due to a stacking change, theoretical calculations are needed to corroborate this hypothesis.

Here we present the theoretical calculations performed by Aran Garcia-Lekue[1] and Daniel Sanchez-Portal[2] from the Donostia International Physics Center (DIPC)[3].

The electronic structures and geometries were calculated using density functional theory (DFT) as implemented in SIESTA [91], using the generalized gradient approximation for exchange-correlation [92] and a cutoff of 310 Ry for the real-space

[1]Ikerbasque, Basque Foundation for Science, E-48011 Bilbao.
[2]Centro de Física de Materiales CFM-MPC, Centro Mixto CSIC-UPV, Apdo. 1072, San Sebastian.
[3]Paseo Manuel de Lardizabal 4, E-20018 San Sebastian.

grid integrations. The basis set consisted of double-zeta plus polarization orbitals for all the atomic species. All the systems investigated were relaxed until forces were smaller than 0.04 eV/Å.

For triangular graphene nanoislands on Ni(111) 7x7 supercell made of a three layer Ni(111) slab was used, with a vacuum region of more than 10 Å between both surfaces, and a graphene island containing 22 carbon atoms placed on one of the surfaces. A 4x4x1 Monkhorst-Pack mesh was used for the k-point sampling of the three-dimensional Brillouin zone. Islands with top-fcc or top-hcp stacking and zz_h or zz_t edges configuration were considered. The system energies obtained are listed in Table 4.1.

System structure	Total energy		ΔE (per C atom)
zz_h, top-fcc	-192338.7771 eV	E_0	$\hat{E}_0 = E_0/22$
zz_h, top-hcp	-192338.5348 eV	E_0+0.24 eV	$\hat{E}_0$+11.01 meV
zz_t, top-fcc	-192334.9143 eV	E_0+3.86 eV	$\hat{E}_0$+175.58 meV
zz_t, top-hcp	-192334.8637 eV	E_0+3.91 eV	$\hat{E}_0$+177.93 meV

Table 4.1: DFT calculated energies for triangular graphene nanoislands with different stacking and edge type.

The lowest energy corresponds to the triangular graphene nanoislands with zz_h edges and top-fcc stacking. The small energy difference with zz_h edges and top-hcp stacking explains why we observe small triangular graphene nanoislands pointing to the opposite direction. The zz_t edges cause a large increase in the system energy, in agreement with the fact that they are not observed experimentally.

A system with bridge-top stacking with one zz_γ and two zz_α edges have also been studied. The structure relaxed to a system with zz_h edge and top-fcc stacking. Therefore the system is considered to be unstable.

4.4 Hexagonal graphene nanoislands

Hexagonal graphene nanoislands were grown using the procedure described in detail in chapter 3. The parameters used to grow the hexagonal graphene nanoislands are D=2 L, T_R=500 ºC, t_R=5 min, T_A=650 ºC and t_A=10 min. In this section we discus the atomic structure of the hexagonal graphene nanoislands edges and their stacking with the substrate. Hexagonal graphene nanoislands have a top-fcc stacking with alternated zz_h and $zz_t(57)$ edges, a pentagon-heptagon reconstruction of the zz_t edge. In analogy to the study of triangular graphene nanoislands, we present experimental and theoretical evidences.

4.4.1 Experimental results

4.4.1.1 Possible structures of hexagonal graphene nanoislands on Ni(111)

Figure 4.12 illustrates the possible atomic structure of hexagonal graphene nanoislands. Independently of the stacking configuration, hexagonal graphene nanoislands have both types of edges, zz_h and zz_t. For this reason the minimum energy stacking should prevail, which is top-fcc stacking (see subsubsection 4.2.3.1).

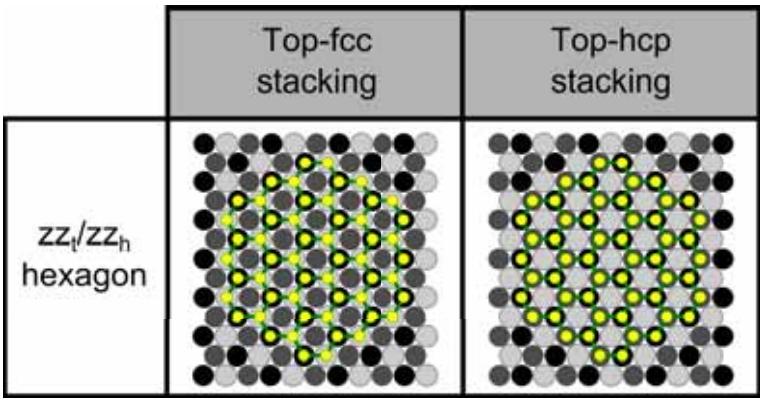

Figure 4.12: Structure of hexagonal graphene nanoislands depending on the stacking with the substrate. Both structures are composed of zz_h and zz_t edges.

4.4.1.2 Edge reconstruction on hexagonal graphene nanoislands

Figure 4.13.a shows an STM image of a hexagonal graphene nanoislands preparation. We observe isolated hexagonal-like graphene nanoislands with a similar size as expected from the preparation size distribution (subsection 3.3.1). As in the case of triangular graphene nanoislands, the hexagonal graphene nanoislands have their edges aligned with the high symmetry directions of the substrate. Because of this alignment, straight zigzag edges would be expected as shown in Figure 4.12. However the following analysis reveals the hexagonal graphene nanoislands are composed of three zigzag edges and three reconstructed edges, as can be seen in more detail in Figure 4.14.

Figure 4.13 shows a STM image of a hexagonal graphene nanoislands, note that the islands have two types of edges that can be distinguished by its structural quality. Figure 4.13.c,d shows STM images of the nanoisland edges obtained by zooming in the STM image shown in Figure 4.13.b. The edges show in Figure 4.13.c have a good structure quality and are assigned to zz_h edges, since they are known to be stable as demonstrated in subsubsection 4.3.1.2. Edges shown in Figure 4.13.d have the same orientation as zz_t, but the zoomed STM images reveal an atomic structure different of pure zigzag edges.

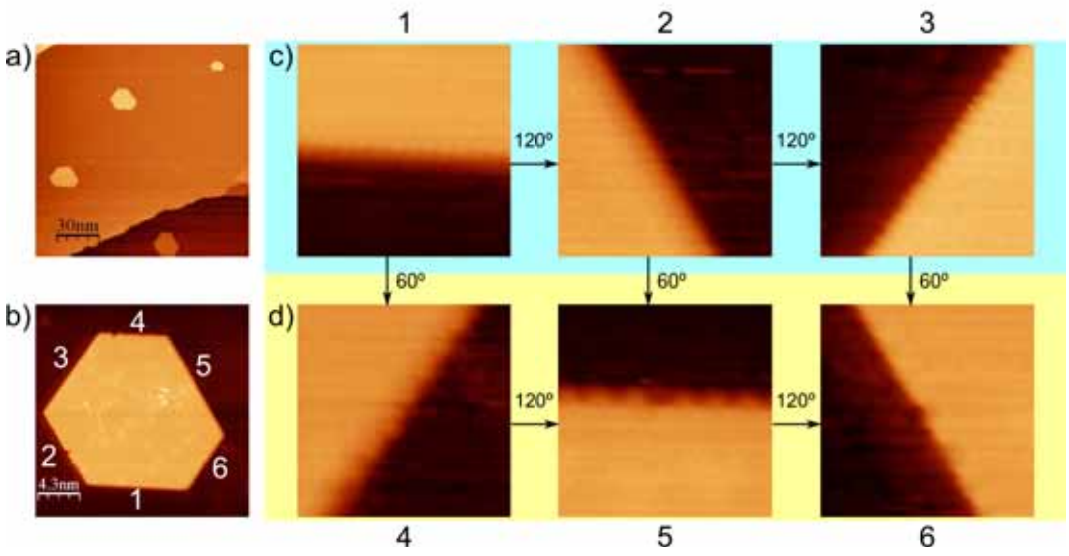

Figure 4.13: a) STM image of hexagonal graphene nanoislands on Ni(111). b) STM image of an hexagonal graphene nanoisland. Note that the island have zz edges with good structural quality, shown in (c), and edges with an atomic structure different than zigzag, shown in (d).

In Figure 4.14.a we observe a corner of a hexagonal graphene nanoisland showing the two types of edges. The edge at the upper part of the image has a zigzag structure with a very good structural quality as seen for triangular graphene nanoislands and corresponds to the zz_h edge. The edge at the lower part of the image corresponds to the edges with a different atomic structure. The atomic resolution STM image reveals an edge reconstruction with a periodicity of two benzene rings. Reconstruction of zz edges has been previously observed on free-standing graphene [93]. Koskinen et. al. [88] calculated the most stable reconstruction for zz edges on free-standing graphene and obtain a reconstruction formed by an pentagon-heptagon carbon rings named zz(57). The zz(57) edge has a periodicity of two benzene rings and perfectly matches the atomic structure observed in Figure 4.14.b.

Figure 4.14.c shows the proposed edge structure for hexagonal islands. As seen in Figure 4.11.c, the last carbon atom of the zz_h edges have their dangling bond pointing to the 1st layer nickel, which gives them a relative stability to avoid the reconstruction. Without reconstructing the zz_t edges would have the dangling bond pointing to a hollow site, but with the proposed $zz_t(57)$ edge, the dangling bonds point to the 1st layer nickel (Figure 4.14.c), which would be energetically more favorable. This model is valid for both top-fcc and top-hcp stacking.

Since all hexagonal islands have about the same length of $zz_t(57)$ and zz_h edges, the edge energy should have no effect on the stacking of the islands with the substrate and the most energy favorable stacking should prevail, which is top-fcc stacking. In any case, we have not found any experimental evidence to determine any of the two

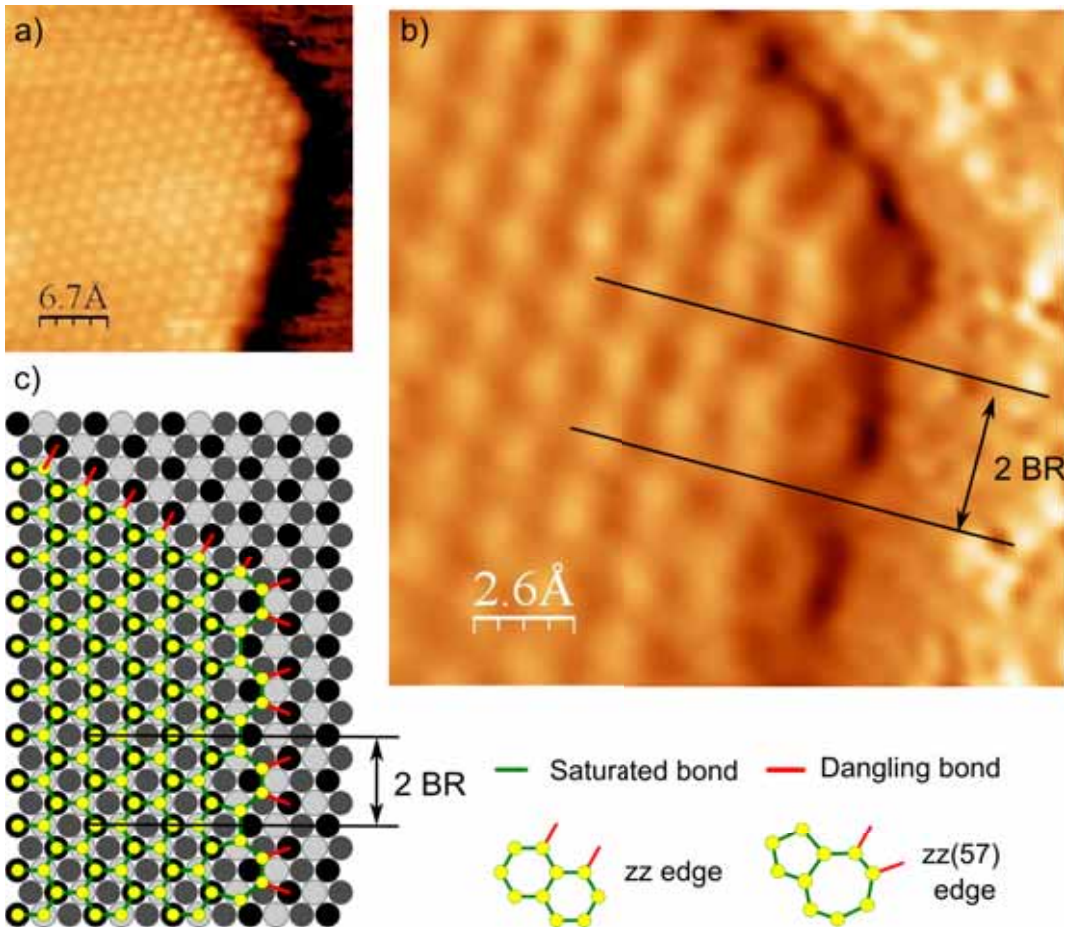

Figure 4.14: a) STM image of an hexagon corner showing an edge with zigzag structure (upper), identified as zz_h, and reconstructed zigzag edge (lower), identified as $zz_t(57)$. b) Derivative of the image shown in (a). The edge reconstruction shows a periodicity of two benzene rings. c) Proposed structure of the hexagonal graphene nanoisland stacking and edge. The $zz_t(57)$ consist of a pentagon-heptagon reconstruction of the zz_t edge.

models and both stacking could co-exist.

To summarize, hexagonal graphene nanoislands grown on Ni(111) substrate interact with the substrate strong enough to orientate all island edges with the crystallographic symmetry directions. Two different types of edges are observed and attributed to zz_h and $zz_t(57)$ edges.

4.4.2 DFT calculation on hexagonal graphene nanoislands configuration

As in the case of triangular nanoislands, to corroborate the experimental results obtained for hexagonal nanoislands we present the theoretical calculations performed by Aran Garcia-Lekue[4] and Daniel Sanchez-Portal[5] from the Donostia International Physics Center (DIPC)[6].

The edge energy of hexagonal nanoislands is more complex to calculate than the case of triangular nanoislands since the cell needed to properly define the structure would be too large and the system can not be calculated directly. In order to determine the stability of reconstructed and non-reconstructed edges the system energies of graphene nanoribbons with zigzag edges were calculated. A 4x8 supercell made up of a 3 layer Ni(111) slab was employed, with a vacuum region of more than 10A between both surfaces, and a graphene ribbon containing 40 C atoms placed on one of the surfaces. A 5x2x1 Monkhorst-Pack mesh was used for the k-point sampling of the three-dimensional Brillouin zone. In this case, only ribbons with top-fcc stacking were considered.

Four different structures are calculated, which consist on nanoribbons with zz_h/zz_t, $zz_h(57)/zz_t$, $zz_h/zz_t(57)$, and $zz_h(57)/zz_t(57)$. The system energies obtained are listed in Table 4.2.

Edge configuration	Total energy	
zz_h/zz_t	-129577.6442 eV	E_0+1.77 eV
$zz_h(57)/zz_t$	-129575.9845 eV	E_0+ 3.43eV
$zz_h/zz_t(57)$	-129579.4155 eV	E_0
$zz_h(57)/zz_t(57)$	-129577.9532 eV	E_0+1.46 eV

Table 4.2: hexagon energies

From the energies obtained it is clear that the lowest energy configuration is the $zz_h/zz_t(57)$, corroborating our experimental results.

[4]Ikerbasque, Basque Foundation for Science, E-48011 Bilbao.
[5]Centro de Física de Materiales CFM-MPC, Centro Mixto CSIC-UPV, Apdo. 1072, San Sebastian.
[6]Paseo Manuel de Lardizabal 4, E-20018 San Sebastian.

Additionally, if we consider the edges individually, the reconstruction of the zz_h increase the system energy 1.65 eV if the other edge is not reconstructed and 1.46 eV in case it is, hence it is not favorable. Nevertheless the reconstruction of zz_t decrease the system energy 1.77 eV if the other edge is not reconstructed and 1.97 eV in case it is, hence it is favorable.

4.5 Stacking rotation in graphene nanoislands

Triangular and hexagonal graphene nanoislands present a 1x1 stacking, minimizing its energy. However in some cases Moiré patters are observed on islands, indicating a rotation of the graphene lattice with respect to the Ni(111) surface.

Different Moiré patterns were observed in a preparation with D=1 L, T_R=500 ºC and t_R=20 min and no post-annealing treatment . Figure 4.15.a shows large graphene island, with dimensions of 50x90 nm, which contains a Moiré pattern, that we designate as pattern "A". Figure 4.15.b shows an enlarged image of the same area (black box). Although the Moiré is present in the majority of the nanoisland, some areas, which are separated by a grain boundary, exhibit the regular graphene topography with the 1x1 stacking. The Moiré maintains the same periodicity and orientation around the nanoisland. The periodicity of the Moiré pattern "A" is determined to be 1.33 nm and the corrugation 0.3 Å. Figure 4.15.c shows the Fast Fourier Transformation (FFT) of the Moiré pattern. Note that the FFT contains two groups of hexagonal spots with different periodicity and orientation. The spots marked with green circles correspond to the graphene lattice, while the spots marked with blue circles correspond to the Moiré pattern. The orientation angle between the Moiré pattern "A" and the graphene lattice can be determined experimentally by directly measuring it on the FFT image. The resulting value is γ=27º.

The lattice parameter of the Moiré pattern "A" observed in Figure 4.15.b is 1.33 nm, which results in reciprocal vector of $\left|\vec{k}_{MA}\right|$=4.72 nm^{-1}; nickel has a lattice parameter of 249 pm [75], resulting in $\left|\vec{k}_{Ni}\right|$=25.2 nm^{-1} and freestanding graphene has a lattice parameter of 246 pm [75], which results in $\left|\vec{k}_{Ni}\right|$=25.5 nm^{-1}. Since graphene and nickel have a very similar lattice parameter, we use a_{eff}=247.5 pm and $\left|\vec{k}_{eff}\right|$=25.39 nm^{-1} for simplifying the calculations. The resultant angles between the reciprocal vectors are $\alpha=\pm 84.7^{o}$, $\beta=\mp 10.7^{o}$. Both solutions will result in the same periodicity of the Moiré pattern, although the orientation will be different. We choose the positive value of β for simplicity reasons. Since the angles are conserved in reciprocal space, the rotation angle between the nickel and graphene lattice is 10.7º. The angle between the nickel lattice and the Moiré pattern "A" is α=-84.7º, which is equivalent to 35.3º due to the six-fold symmetry. The angle between the graphene lattice and the Moiré pattern "A" is $\gamma = \alpha - \beta$=-95.4º, equivalent to 24.6º due to six-fold symmetry. This measure of the rotation between the graphene lattice

and the Moiré pattern "A" has better resolution than the angle obtained directly measuring Figure 4.15.c due to the lens effect of the Moiré.

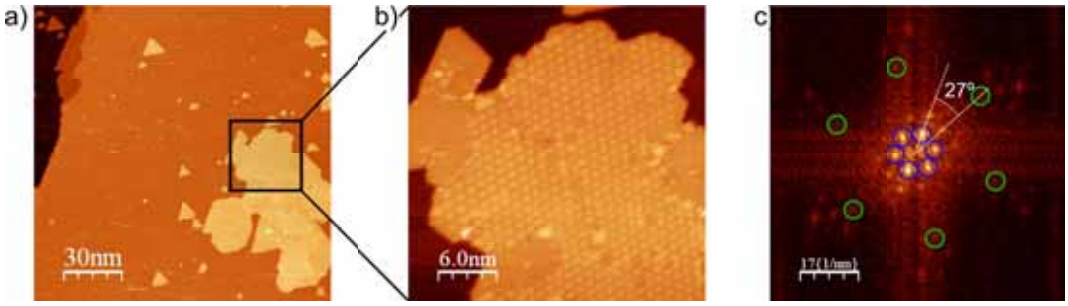

Figure 4.15: a) Graphene nanoislands preparation using D=1 L, T_R=500 ºC and t_R=20 min with no post-annealing treatment. b) Moiré pattern observed in a graphene nanoisland. c) FFT of the Moiré pattern. The green circles mark the sport corresponding to the graphene lattice, the blue circles mark the spots corresponding to the Moiré lattice.

In the same preparation (D=1 L, T_R=500 ºC and t_R=20 min) two additional Moiré structures are observed on graphene attached to a Ni(111) terrace step. Figure 4.16.a shows an STM image containing a Ni(111) terrace step on the right (bright area) which is surrounded by a graphene layer (light brown). In the left part of the image we can observe the Ni(111) surface (dark brown) with some graphene nanoislands. The graphene layer contains two Moiré patterns with different periodicity, indicating a difference in the orientation of the graphene atomic structure. The Moiré situated in the lower part of the graphene layer, which we will call Moiré pattern "B", has a periodicity of 1.02 nm. These periodicity implies a rotation of 13.9º of the graphene lattice with respect to the nickel surface and an angle of 36.9º between the nickel surface and the Moiré pattern. Note that these value is more precise than the 35º obtained directly by measuring the STM images (Figure 4.16.b). The Moiré pattern observed in the central part of the graphene layer, which we will call Moiré pattern "C", has a periodicity of 1.80 nm. Equation 4.9 gives a rotation between the graphene lattice and the nickel surface of 7.8º, and Equation 4.10 gives an angle between the nickel surface and the Moiré pattern of 33.9º, which is close to 31º obtained by STM.

Figure 4.17 shows an illustration of the three Moiré patterns observed. Note that not any angle is possible. Similarly to what occurs in the center of the schemes shown in Figure 4.17, the coincidence of carbon and nickel atoms repeats in the symmetry points of the Moiré pattern. Tacking as a reference the lattice vectors

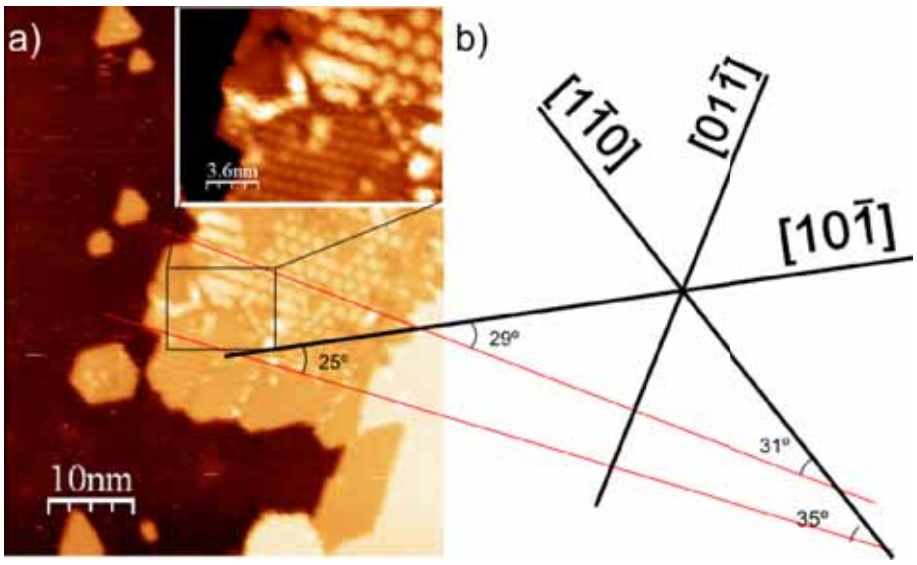

Figure 4.16: a) Two Moiré patterns observed in graphene on Ni(111). The small inset is a zoom with increased contrast of the region inside the black box containing the two Moiré patterns. b) The Moiré patterns are rotated rotated 31º and 35º respect to the Ni(111) surface.

of the rotated graphene lattice ($\vec{a}_{g,1}$ and $\vec{a}_{g,2}$) and and the nearest neighbor of the nickel surface ($\vec{a}_{Ni,1}$ and $\vec{a}_{Ni,2}$) the Moiré superstructure show here correspond to a displacement of

$$3\vec{a}_{g,1} + 3\vec{a}_{g,2} = 2\vec{a}_{Ni,1} + 4\vec{a}_{Ni,1}$$
$$3\vec{a}_{g,1} + 2\vec{a}_{g,2} = 2\vec{a}_{Ni,1} + 3\vec{a}_{Ni,1}$$
$$5\vec{a}_{g,1} + 4\vec{a}_{g,2} = 4\vec{a}_{Ni,1} + 5\vec{a}_{Ni,1}$$

for Moiré patterns A, B, and C respectively.

Moiré patterns of graphene on nickel were previously observed by Murata et. al. [94] on Ni(111) and Ni(110) facets of a nickel island grown on an HOPG substrate. Moiré patterns were also reported on graphene on single crystal Ni(111) samples [39, 95, 77, 89]. Jacobson et. al. investigated the origin of graphene Moiré patterns on Ni(111) [89]. They found that the presence of Ni_2C on the Ni(111) surface prevents graphene from adopting the 1x1 stacking configuration and leads to grain rotation. The Moiré patterns reported in this study show periodicities of 9.5 Å and 6 Å with rotation angles of 14.6º and 23.8º respectively. An alternative mechanism to obtain rotated graphene on Ni(111) is proposed by Lahiri et. al. [39]. They obtained a Moiré pattern with a periodicity of 2.7-3 nm and a rotation of 3º. They stated that this small angle misalignment have its origin in the growth of graphene from Ni_2C that occurs at 400 ºC in the time scale of hours. In the case of the graphene nanoisland preparations shown in this thesis, the formation of Ni_2C occurs during the

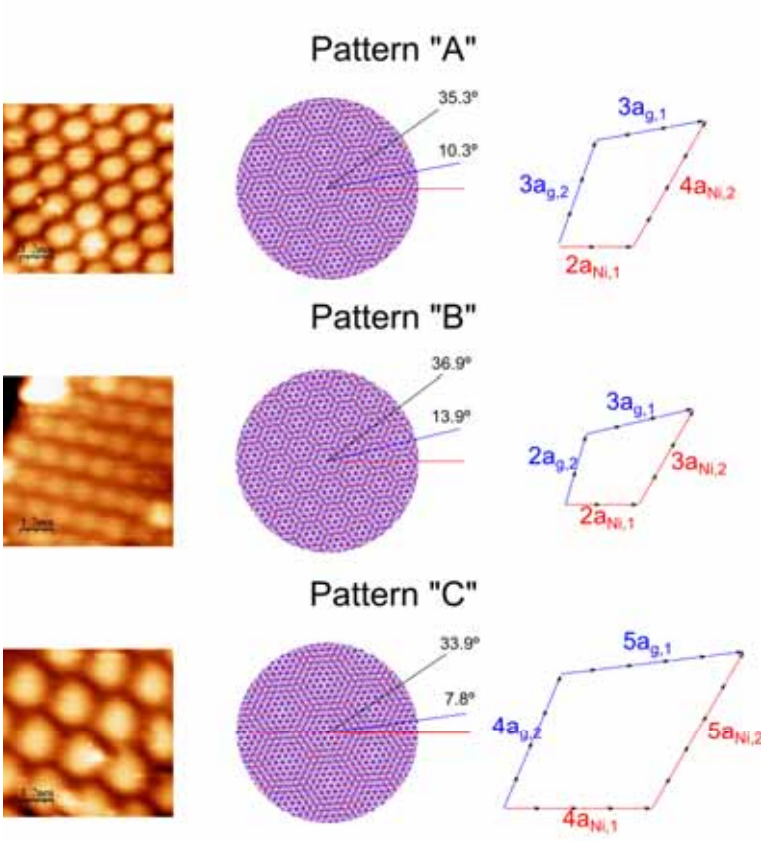

Figure 4.17: Scheme of Moiré patterns "A", "B" and "C" respectively. Red (blue) represent the nickel (graphene) lattice and latticevectors.

heating ramp and could explain the observed graphene rotation. Since the sample is maintained at T_R=500 ºC for several minutes, Ni_2C dissolves into bulk because it is unstable at 500 ºC (see Figure 3.4 and subsection 6.2.3) and no graphene growth by direct transformation from Ni_2C is expected. Also the periodicities observed correspond to higher angles, in the same range than the observed by Jacobson et. al. For those reason we believe than our rotated domains have the same origin than the obtained by Jacobson et. al.

The existence of Moiré patterns with different orientations demonstrates the weak adsorption of graphene on Ni(111). However, the presence of Moiré patterns in the system is very limited, indicating that the lowest energy configuration for graphene on Ni(111) is the 1x1 stacking.

4.6 Summary

Graphene nanoislands on Ni(111) usually present a 1x1 stacking with the substrate. Moiré patterns occasionally found on large graphene nanoislands on Ni(111) indicate a small interaction of the graphene layer with the substrate. This means that the graphene edge interaction with the substrate plays a dominant role in determining its atomic structure.

Atomic resolution STM images show triangular and hexagonal graphene nanoislands on Ni(111) with good structural quality and 1x1 stacking with the substrate. Island edges are zigzag-like and no armchair edges are observed in any case. Depending on the position of the last carbon atom, zigzag edges can be divided in hollow (zz_h) and top (zz_t) type.

Triangular graphene nanoislands are composed only of zz_h edges. Although both stacking configurations were observed in triangular graphene nanoislands, due to the small energy difference, top-fcc stacking is by far more frequent. Hexagonal graphene nanoislands show zz_h and $zz_t(57)$ edges alternated. The $zz_t(57)$ edge is a pentagon-heptagon reconstruction of the zz_t edge. Although top-fcc stacking is expected to be more frequent due to its lower energy, no experimental evidence has been found to corroborate this statement. DFT calculations corroborate the experimental results obtained and assign the lowest energy configuration to the structures observed experimentally.

Moiré patterns are observed on some graphene nanoislands. Three different periodicities are observed, which correspond to different rotations of the graphene lattice with respect to the Ni(111). The rotation angles are determined to be 27º, 31º and 35º. The existence of rotated domains is attributed to the presence of Ni_2C domains in the surface during the growth mechanism. Its stability demonstrates the weak absorption of graphene on Ni(111), and the prevalence of the minimum energy edge configuration in the final system structure, also supported by DFT calculations.

5 Dynamics of the graphene nanoislands growth

The electrical properties of graphene strongly depend on its crystalline quality. For that reason understanding and controlling the growth mechanism is of a crucial importance to obtain graphene layers with enough good quality. Although graphene growth on metals has been studied for long time [96], few is know about the growth mechanism that drives the reaction. On Ni(111) the growth of graphene has been studied by different techniques. Grüneis et. al. studied the reaction with photoemission [81]. They found that graphene growth does not start immediately when the crystal is exposed to carbon containing gas. Images obtained with low energy electron microscopy [41, 97] show the growth of the graphene layer and multilayer in real time, but the spatial scale does not allow to determine the atomic mechanism. Measurements performed with Raman spectroscopy [42] demonstrate that on Ni(111) the carbon is dissolved into the bulk and then incorporated to the graphene layer, in contrast to the case of Cu(111) where the carbon stays at the surface. The growth mechanism of graphene on Ni(111) have also been studied theoretically by means of molecular dynamics [84], density functional theory [98, 99] and Monte Carlo simulations [100, 101]

Although several efforts have been devoted to the study of graphene growth, a little is know about the growth of graphene on Ni(111). Up to date, no conclusive studies have been done at the nanoscale and the theoretical models are on their initial stages. In section 3.3 we observed an evolution of the irregular graphene nanoislands when annealing the sample at a temperature T_A during a certain time t_A. The changes observed consist in shape changes and an area increase of the nanoislands. In this chapter, we present a real time study of the growth and reshaping of graphene nanoislands on Ni(111) when annealed, which takes place by incorporation of new carbon to the islands. This system is ideal for the study of carbon incorporation to graphene edges since the carbon concentration is low and the reaction occurs in measurable time scales, also graphene nanoislands offer a system with edge abundance. We found that different growth modes are found depending on the temperature.

5.1 Experimental details

All the experiment described in this chapter were performed in the high temperature experimental setup (subsection 2.3.2). In this series of experiments a clean Ni(111)

sample was used. The Ni(111) crystal was cleaned by repeated cycles of Ar^+ sputtering followed by annealing at 800 ºC for 1 minute until the surface presents no traces of carbon contamination by means of STM inspection. Topographic STM images of the surface were obtained using the Aarhus 150 STM HT STM and processed using the WSxM software [79].

Figure 5.1 describes the procedure used to prepare the sample used in the experiments described in this chapter. Irregular graphene nanoislands were grown on the clean Ni(111) sample using the method described in section 3.2. The parameters used for the growth of the irregular nanoislands are T_R=500 ºC, t_R=5 min and a dose D of propene which varies depending on the preparation (Figure 5.1). No annealing treatment was done on the sample prior to the STM measurements.

Once the nanoislands are formed the sample is introduced on the STM. The sample is heated in-situ in the STM at a temperature T'_A while measuring to recreate the conditions of the post-annealing process performed after the graphene nanoislands formation (Figure 3.1.c) , as observed in Figure 5.1.c. It is important to mention that to obtain STM images at high temperature the temperature of the sample has to be very stable to minimize the thermal drift. During this process we obtain STM images at time t'_A, with t'_A=0 being defined as the starting moment of the first STM image with a manageable thermal drift. The duration of the heating ramp varies from preparation to preparation with a period of time that ranges from 10 to 15 min.

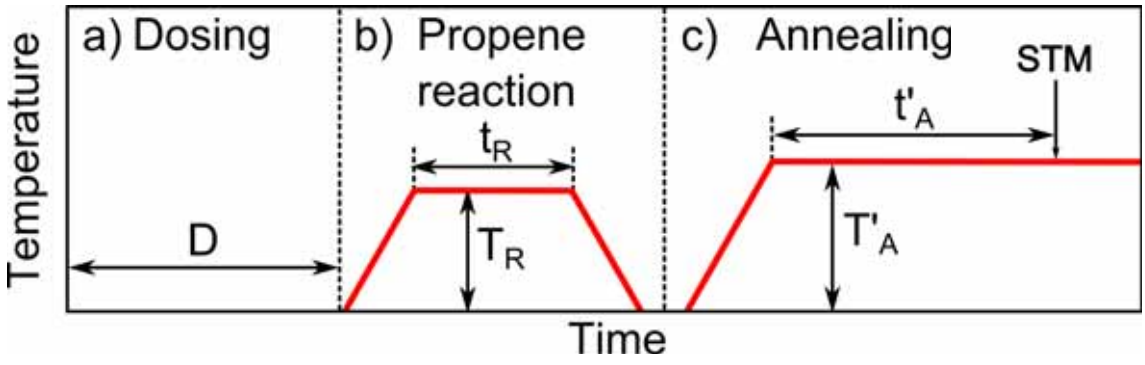

Figure 5.1: Scheme of the preparations to study the growth of graphene nanoislands on Ni(111) used in this chapter. a) The dosing phase consist in exposing the clean Ni(111) sample to a propene pressure. b) At the reaction phase the sample is heated to a temperature T_R during a time t_R. The sample is cooled RT at the end of that phase. c) The annealing phase consist of annealing the sample at T'_A. In this chapter the STM images are obtained during the annealing process using a high temperature STM. t'_A represents the acquisition time of repeated STM images.

Due to the impossibility of obtaining the surface temperature with the pyrometer

(T_p) while heating, the temperature was measured using a thermocouple(T_{tc}) integrated in the sample holder. A calibration function $f(T_{tc}) = T_p$ was determined experimentally between the two temperature values by measuring simultaneously with the thermocouple and the pyrometer the temperature of a sample when cooling from 800 ºC to RT. The different thermalization speed of the sample and the sample holder could induce and systematic error in the calibration function that, in expenses of the results obtained in the experiments, could result in an underestimation of $\leq$20 ºC of T_p. For clarity reasons, the temperature values in all chapters in this thesis are given using the pyrometer scale (T_p).

In order to study the evolution of the system while heating the sample at T'_A, most of the STM images shown in this chapter are obtained in the same area of the sample consecutively. These sets of images can be interpreted as frames of a movie showing the time evolution of the sample. The complete movies can be found in [102].

For clarity reasons, the images which belong to a movie are numbered with white roman numbers in figures.

5.2 Annealing at 450 ºC

When annealing irregular graphene nanoislands at T_A=450 ºC, no shape evolution is observed, although this fact does not imply that the system remains stable at this temperature. In the following section, we discuss the evolution of the irregular graphene nanoislands on Ni(111) when annealed at 450 ºC for different periods of time.

5.2.1 Experiment description

To study the evolution of the graphene nanoislands on Ni(111) during annealing, we perform in-situ STM measurements on a sample with previously prepared irregular graphene nanoislands and annealed at T'_A=450 ºC. The irregular graphene nanoislands were prepared following the procedure described in section 3.2 using D=1.8 L, T_R=500 ºC and t_R=5 min. We perform in situ STM measurements on two areas of the sample with the following characteristics:

- *First set:* Contains 15 STM images with a size of 50 X 50 nm with an acquisition time of 52.6 s, obtained with a bias voltage of 0.4 V. The first STM image was obtained at t'_A=2 min 40 s and the last at t'_A=16 min 42 s, hence the set covers a time period of 14 min 2 s. This set illustrates the **early evolution** of the system.
- *Second set:* Contains 31 STM images with a size of 150 X 150 nm with an acquisition time of 157.6 s, obtained with a bias voltage of 0.4 V. The first STM image was obtained at t'_A=19 min 16 s and the last at t'_A=98 min 7 s,

hence the set covers a time period of 78 min 51 s. This set illustrates the **late evolution** of the system.

5.2.2 Early evolution of the growth

In this subsection we show the early evolution of the system. To do so, a preparation of irregular graphene nanoislands is heated at T'_A=450 ºC and maintained at this temperature while obtaining the STM images. Figure 5.2.a shows a group of STM images which belong to the first set described in subsection 5.2.1. The STM images are obtained using a bias voltage of 0.4 V. Each image has an acquisition time of 52.6 s and are obtained non consecutively at time t'_A=5 min 56 s, 8 min 34 s, 11 min 26 s, 14 min 4 s and 15 min 49 s respectively. The whole set of images shown in Figure 5.2.a covers a period of time of 9 min 53 s.

As observed in Figure 5.2.a, the irregular graphene nanoisland grow with time. The growth of the islands takes place by adding new carbon atoms to the edges. It is important to mention that no additional carbon is introduced in the system by dosing propene and no Ni_2C is observed in the surface. Therefore, the only sources of carbon must be the one from the previously dissolved in the nickel. The origin of this carbon can be the cracking of the hydrocarbon molecules or the intrinsic carbon impurities of nickel crystals . The diluted carbon emerges and propagates the graphene structure around the islands. The carbon density is an important factor for the nucleation of graphene nanoislands at the initial stages [100], but once the C atoms form the graphene nanoislands, they remain stable at the surface and act as C traps. Hence the graphene nanoislands will grow by incorporation of new carbon atoms, independently of the carbon concentration of the system. The growth takes place in an isotropic manner. The islands presents some structural defects observed as bright points, no changes in these defects is observed so we can conclude that no reorganization of the internal structure of the islands occurs at this temperature. Figure 5.2.b shows a scheme of the island growth followed by the nanoisland marked with a blue asterisk in Figure 5.2.a.I. The island growth in all directions until it encounters another nanoislands and merge with it. Figure 5.2.c shows the time evolution of the area of the islands marked with a green asterisk in Figure 5.2.a.I. As seen in the graph the nanoisland grows constantly with time and increases its area from 53 to 127 nm^2 in 520 s.

Recent theoretical studies [84] predict a growing mechanism for graphene nanoislands using a molecular dynamics model consisting on the addition of individual carbon atoms to the nanoislands. The addition of individual atoms induces defect formation at the edges, which would be solved by the addition of new carbon atoms and the time evolution of the system. This study considers time evolution periods lower than 100 ps, which is far below our time resolution. The annealing temperatures for this study range between 800-1400 K, which in our opinion are too high. It has been probed experimentally that graphene nanoislands are not stable at this

temperature (see section 3.3). In any case, graphene nanoislands at 450 ºC does not posses straight edges (zigzag), but rather rough edges. This implies a high concentration of defects on its edges which could act as carbon traps. The isotropical distribution of defect could explain the isotropical growth of graphene nanoislands at 450 ºC.

.

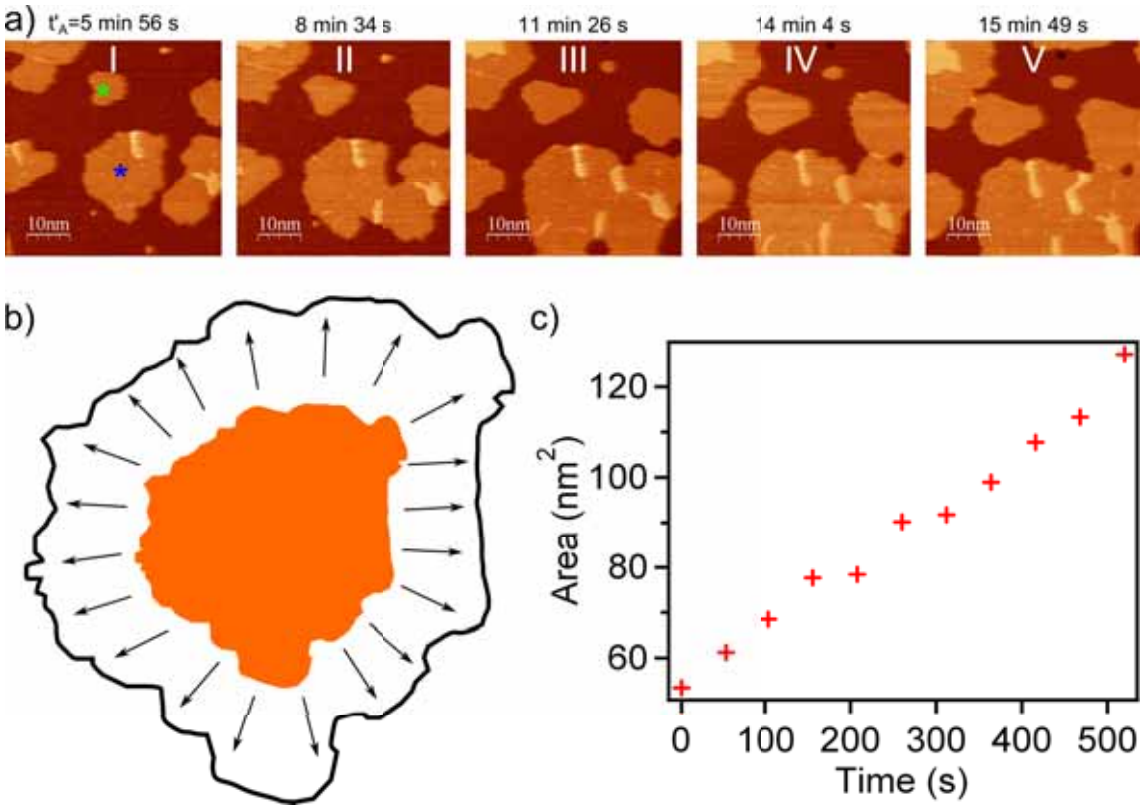

Figure 5.2: a)STM images of irregular graphene nanoislands on Ni(111) growth process at 450 ºC. b) scheme of the isotropic growth of graphene nanoislands at 450 ºC. c) areal increase with time of the graphene nanoislands marked with a green asterisk in (a)

5.2.3 Late evolution of the growth

At small time scales the growth of the islands occurs similarly in all directions; however, when the annealing is maintained for long enough time, the coalescence of islands starts to play an important role in the system evolution. In this subsection we show the processes that take place at long time scales. All STM images which contain graphene nanoislands shown in this section belong to the second set described in subsection 5.2.1.

Figure 5.3.a shows an STM image of a clean Ni(111) surface obtained at 450 ºC with a bias voltage of 0.4 V prior the preparation of graphene nanoislands. This STM image does not belong to the second set, but it is useful to show the substrate properties. The image contains a terrace step that cross the whole frame vertically. The horizontal blue line in Figure 5.3.a represents the height profile shown in Figure 5.3.c. The height profile is obtained along the scanline direction and shows a terrace step height of 2.1 Å, which is the same of a Ni(111) terrace step height at RT. The Ni(111) surface is relatively stable at this temperature and no significant terrace step mobility is observed.

Figure 5.3.b shows a group of four STM images of irregular graphene nanoislands while annealed at at T'_A=450 ºC. The images belong to the second set of images described in subsection 5.2.1. The images were obtained all in the same area, although the effect of the thermal drift displace the scanned area downwards. The STM images were obtained at t'_A=19 min 16 s, 35 min 2 s, 61 min 19 s and 98 min 7 s respectively. Hence the STM images shown in Figure 5.3.b represents the time evolution of the irregular graphene nanoislands on Ni(111) when maintained at 450ºC for a period of time of 78 min 51 s.

Figure 5.3.b.I shows a STM image of irregular graphene nanoislands on two terraces of a Ni(111) surface. The terrace step crosses the frame in the vertical direction as in Figure 5.3.a, although this is a different area of scanning. We observe irregular graphene nanoislands on both terraces with the same density, showing an homogeneous distribution. The horizontal blue line in the upper-left of Figure 5.3.b.I represents the height profile shown in Figure 5.3.d. The height profile shows a Ni(111) terrace step, with a height of 2.2 A, and a graphene nanoislands, with a height of 1.3 Å. The small difference of the height of the graphene nanoislands with respect to the value obtained in previous chapters (1.3 Å vs 1.5 Å) is due to the difference in the bias voltage of the STM measurements (see section 2.4).

As observed in the STM images of Figure 5.3.b the graphene nanoislands grow continuously until they merge (Figure 5.3.b.II-IV). This process culminates once the graphene covers the whole nickel terrace and forms a graphene monolayer (Figure 5.3.b.IV). It is important to mention that no graphene bilayer is formed with this process at this time scale as we will demonstrate below. Graphene growth occurs only by adding new material to the graphene edge as described in subsection 5.2.2. At the nickel terrace step, the graphene growth is stopped, and the graphene does not overcome the step as in the case of graphene growth on Ru [34] or Ir(111) [103], neither upwards nor downwards. We can also observe a dendritic structure intercalated in the graphene monolayer attributed to intercalated nickel clusters as we will demonstrate below. The nickel clusters have a random shape and appear during the graphene growth. As for the graphene, the nickel clusters are stable once formed. The horizontal blue line in the center of the STM image in Figure 5.3.b.IV represents the path of the height profile shown in Figure 5.3.e. The height profile crosses a small nickel cluster, with height of 1.0 A. The formation mechanism of the nickel cluster will be explained in subsubsection 5.2.3.1.

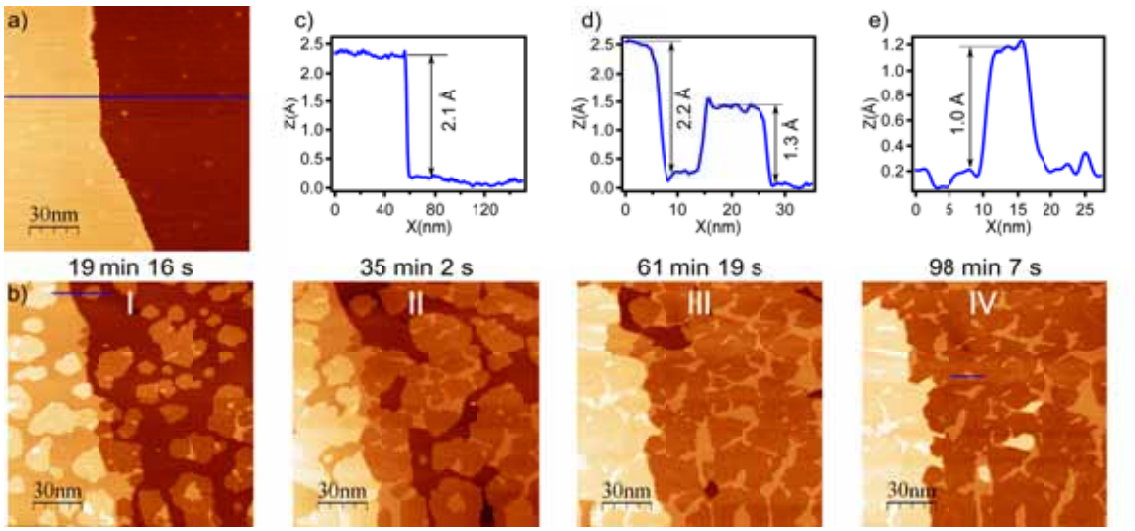

Figure 5.3: a) STM image of a Ni(111) surface at 450ºC. b) Four STM images of graphene nanoislands at 450 ºC showing the late evolution of the system. The nanoislands grow until a graphene monolayers covers the whole surface. c) Height profile along the blue line in a). d) Height profile along the blue line in (b.I). e) Height profile along the blue line in (b.IV).

5.2.3.1 Nickel trapped between graphene islands

The STM image shown in Figure 5.4.a was obtained in the same area represented in Figure 5.3.b at t'_A=29 min 47 s. The area inside the black box shows 5 graphene nanoislands that are about to merge. The process is illustrated in Figure 5.4.b, with three STM images of the same area that were obtained at t'_A=29 min 47 s, 32 min 24 s and 56 min 4 s respectively. Figure 5.4.b.I, the islands are about to merge. Note that in Figure 5.4.b.II, the small area that separated the nanoislands 1, 2, 3 and 5 in Figure 5.4.b.I is mostly covered by nickel trapped between graphene islands, although is it possible to observe some graphene that "connects" the nanoislands (except in the case of island 1 with 2) . Hence the nickel trapped between graphene islands, which we will name as nickel cluster, has a growth rate much faster than the acquisition time, contrary to the graphene growth, which occurs on the scale time of several minutes.

The blue horizontal line in Figure 5.4.b.II represents the path of the height profile shown in Figure 5.4.c. The height profile shows three regions. The sides of the height profile are attributed to the Ni(111) surface. The center-left layer is attributed to graphene, with a height of 1.3 Å respect to the nickel substrate. The center-right of the height profile is attributed to nickel cluster, since its height is 2.2 Å, the same height of the Ni(111) terrace step. Note that the height of the nickel cluster respects to the graphene layer is 0.9 Å, which is in the margin of error of the value obtained in subsection 5.2.3. Figure 5.4.d shows a scheme of the assignation of different height areas with the different compounds.

Gao et. al. [98] studied the energy cost of graphene edges on a Ni(111) surface. They found that the energy cost of zigzag and armchair edges is reduced when the graphene edge is situated on a metal step edge by about 3 eV/nm. This notable energy reduction could be the driving force of the formation of the nickel clusters. Note that the metal decorated graphene edge is not observed experimentally in graphene nanoislands on Ni(111) (see chapter 4) due to its instability [99]. It is important to remark that the nickel clusters are only formed when the graphene edges are very close. Also all the nickel clusters observed have most of their edges bounded to a graphene layer, hence we can think that the nickel edge formation energy is the limiting factor for the passivation of the graphene edges by Ni atoms.

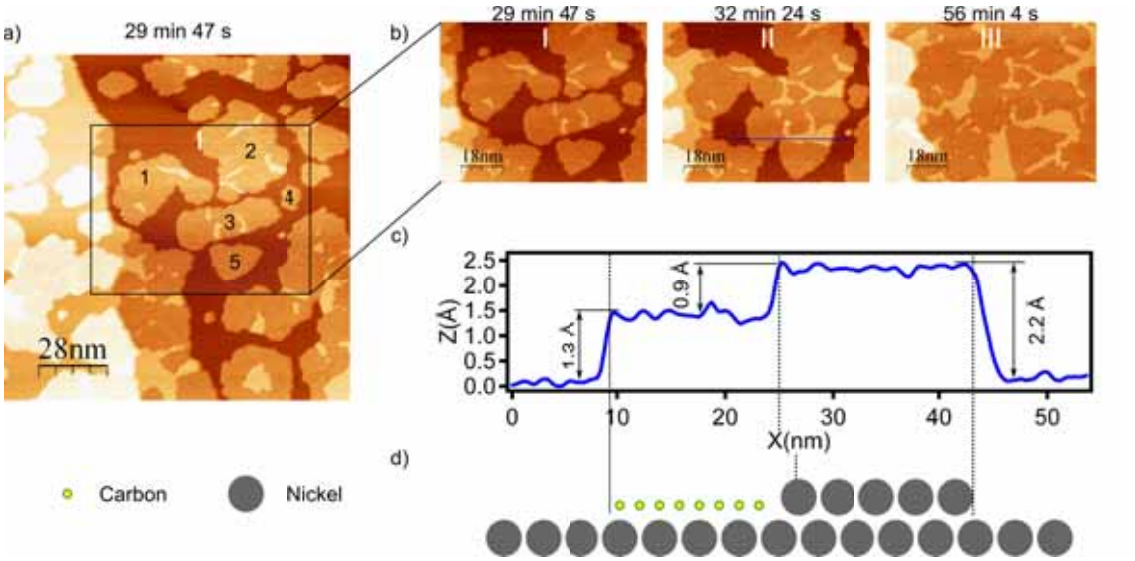

Figure 5.4: a) STM image of irregular graphene nanoislands at 450 ºC. The black box indicates the area zoomed in STM images shown in b). b) Three STM iamges representing the time evolution of the system. The frontier between island is filled with nickel cluster that appear suddenly. c) Heigh profile along the blue line in b.II). d)scheme of the atomic structure of the system compared to the height profile in c)

5.2.3.2 Impurities on nickel clusters

Once the graphene nanoislands have merged and stop their growth, the resultant layers is a mix of a monolayer graphene with trapped nickel clusters. In this situation the graphene appears stable for long time scales. However, the nickel clusters suffer an evolution induced by the apparition of impurities and its associated instabilities. Figure 5.5 shows the changes observed in three different nickel clusters in different periods of time. In Figure 5.5.a, we show an STM image of the graphene monolayers formed during the nanoisland merging process. The image contains three black boxes which situate the processes illustrated in Figure 5.5b-d. These three processes,

which are not unique, take place in different moments in the scanned region with a frequency of 8 observed events for 50 min 2 s, which corresponds to a frequency of $\sim 10^{-7}$ $s^{-1}nm^{-2}$. The STM images shown in Figure 5.5b-d are obtained by zooming in STM images with a size of 17.6x17.6 nm, for this reason the resolution is limited.

Figure 5.5.b shows three STM images obtained at t'_A=71 min 50 s, 74 min 27 s and 77 min 5s respectively. In Figure 5.5.b.I we can identify a nickel cluster surrounded by a graphene layer. The nickel cluster has a ribbon shape and crosses the frame in the horizontal direction. In Figure 5.5.b.II an impurity appears at the center of the nickel cluster. The horizontal blue line represents the path followed by the height profile shown in Figure 5.5.b.IV. The impurity height 1.8 Å with respect to the nickel cluster, although this measurement may have an additional error due to the low resolution of the zoomed images. In Figure 5.5.b.III we observe that the impurity has disappeared. In its place the nickel cluster has now a hole which is filled by graphene. Then, this process results in the partial destruction of the nickel cluster and substitution by graphene.

In Figure 5.5.c we observe a similar process. Figure 5.5.c shows three STM images obtained at t'_A=60 min 59 s, 63 min 57 s and 69 min 12 s respectively. In the first STM image we observe two nickel clusters, one in the lower-left part of the image and the other in the upper-right. In Figure 5.5.II two impurities appear on the cluster, one on each. The two horizontal blue and green lines represent the path of the height profiles shown in Figure 5.5.c.IV and Figure 5.5.c.V respectively. The two impurities have different height, a difference that could be due to the different size of the impurities and the error induced by the low resolution of the STM images. The different origin of the impurities is a fact that can not be discarded since the two impurities evolve in a different manner as seen in Figure 5.5.c.III. The impurity on the nickel cluster in the lower-left part of the image evolve as in the previous cases, disappearing and creating a hole in the nickel cluster which is filled by graphene. Nevertheless the impurity on the nickel cluster in the upper-right part of the image acts as a nucleation center of a new layer of graphene that grows on the nickel cluster as explained in detail in the next subsection.

5.2.3.3 Graphene growth on nickel clusters

As discussed in the previous section, the nickel clusters trapped in the monolayer graphene are not stable for long scale times. In this section we illustrate the growth on a graphene monolayer on a nickel cluster induced by an impurity. Figure 5.6.a shows an almost complete graphene monolayer with intercalated nickel clusters as a result of the process illustrated in subsection 5.2.3. The images proceed from a zoom realized in the area marked by a black box in Figure 5.6.b. The STM images shown in Figure 5.6.b are obtained with a bias voltage of 0.4 V at t'_A=60 min 59 s, 63 min 57 s, 74 min 27 s, 84 min 58 s and 98 min 07 s respectively. They show the process that initiates in Figure 5.5.d. As explained in the previous section, two impurities appear, which evolve differently. The first one, situated in the lower

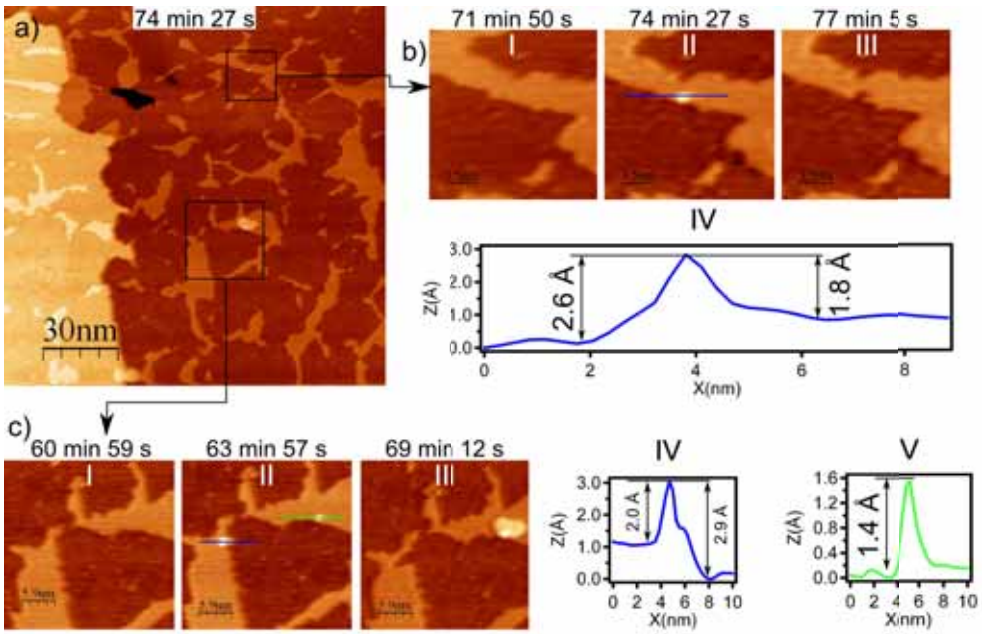

Figure 5.5: a) STM image of a graphene monolayer at 450ºC formed from irregular graphene nanoislands growth. The black boxes represent the area zoomed in b), c) and d). b,c,d) Impurities evolution on nickel clusters and their height profile along the color lines in STM images.

left part of the STM image disappears creating a hole in the nickel cluster. The second one acts as a nucleation center for the growth of a graphene monolayer on the nickel cluster, as seen in Figure 5.6.b.III. The graphene monolayer grow through the nickel cluster until it is completely covered, as seen in STM images shown in Figure 5.6.b.IV-V. The growing of this graphene never extends over the limits of the nickel cluster growing of top of the original graphene monolayer, hence no graphene bilayer is observed in this experiment. At the same time, the growth of graphene monolayers on nickel clusters occurs in other areas, as observed in Figure 5.6.b.IV-V. From the eight impurity events observed, three evolve as a graphene monolayer. Therefore this process is quite common and is expected to cover all the nickel clusters if the sample is held at 450ºC for enough time. The horizontal blue line drawn in Figure 5.6.b.III represents the path of the height profile shown in figure Figure 5.6.c. In the height profile we observe that the graphene layer on the nickel cluster has a height of 1.2A with respect to the nickel cluster, which is comparable to that of the

graphene nanoislands with respect to the Ni(111) surface.

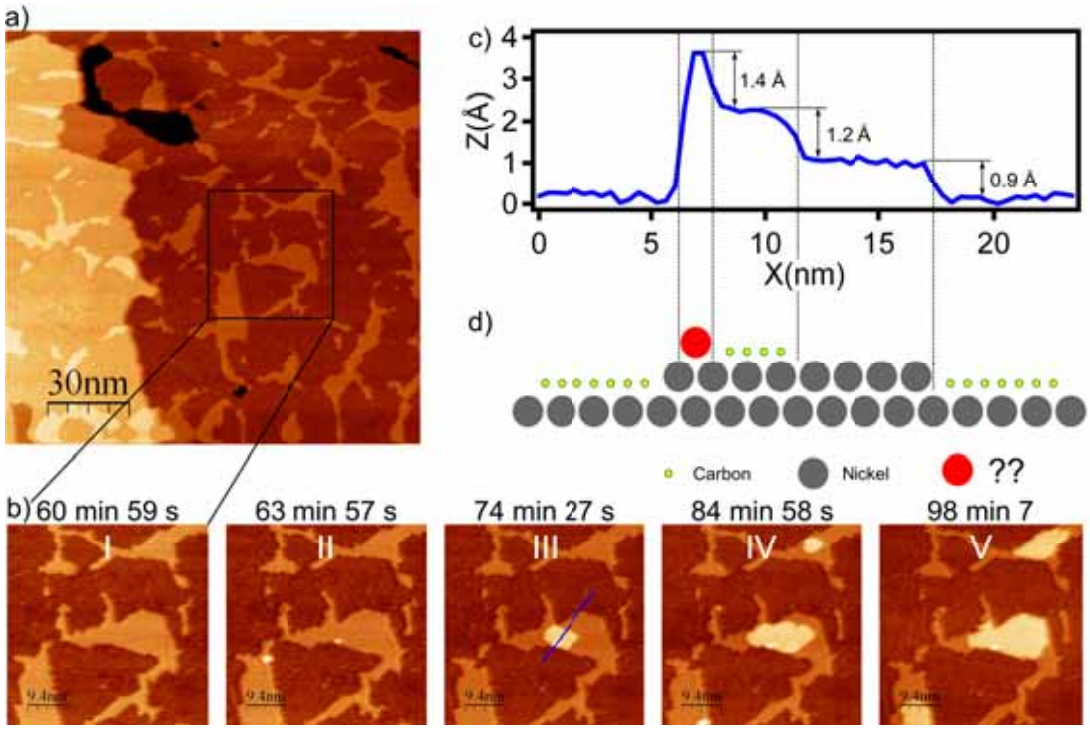

Figure 5.6: a) STM images representing the time evolution of an impurity on a nickel cluster and the formation of a graphene monolayer on it. b) STM image of the graphene monolayer formed from irregular graphene nanoisland growth. The black box represents the area zoomed in a). c) Height profile along the blue line in a.III). d) Scheme of the atomic structure of the system in comparison of the height profile show in c).

5.3 Annealing at 500ºC

As described in section 3.3, the irregular graphene nanoislands undergo several changes when annealed at 500ºC for a certain time. One is the increase of the area of the nanoislands. This process occurs in the same way when annealing the irregular graphene nanoislands at lower temperatures as explained in section 5.2, for this reason it will not be explained again in this section.

Another important change when annealing at 500ºC, is the shape variation of the nanoislands. In experiments performed in subsection 3.3.1 the shape parameter of the islands shows a clear peak around the triangular value (see Figure 3.11). This indicates that irregular graphene nanoislands adopt a triangular shape when annealed at 500 ºC. In this section we study the changes that take place in the irregular graphene nanoislands when annealed at 500ºC in detail.

5.3.1 Shape evolution of irregular graphene nanoislands

The growth of the islands at T'_A=450 ºC is isotropic as seen in subsection 5.2.2. When increasing the temperature to at T'_A=500 ºC or higher the growth becomes anisotropic, leading to a preferred shape of the nanoislands.

In order to study the transformations of the islands at T'_A=500 ºC we prepare a sample with graphene nanoislands on Ni(111) by following the method described in detail in section 3.2. A clean Ni(111) crystal was dosed with D=1.8 L of propene at RT and then heated at T_R=500 ºC for t_R=5 min. This results in the formation of irregular graphene nanoislands. Once the nanoislands are formed the sample is transferred to the STM, where it is heated at T'_A=500 ºC, and STM images were acquired sequentially to study in detail the processes that take place at this temperature.

In Figure 5.7.a we show three STM images obtained at T'_A=500 ºC with a bias voltage of 1.1 V. The images have an acquisition time of 105 s and were obtained at t'_A=17 min 32 s, 42 min 56 s and 93 min 49 s respectively. The images are part of a set of 46 STM images obtained consecutively in the same area to study the time evolution of the irregular graphene nanoislands when annealed. The complete movie can be found in [102]. In Figure 5.7.a.I-III we observe a Ni(111) terrace that covers almost the entire image. In the upper-right part of the image a higher Ni(111) terrace is observed. The main Ni(111) terrace contains 7 graphene nanoislands with irregular shape and different sizes. In Figure 5.7.a.I we observe a double tip effect, which does not affect the interpretation of the data. All the graphene nanoislands increase their size by adding new graphene to the edges and the nanoislands approach a triangular shape. It is important to remark that all the triangular nanoislands are oriented in the same manner, which indicates an effect of the substrate in this process. Hence, the addition of new material to the nanoislands does not take place in a random manner as in the case at T'_A=450 ºC. This difference is due to the edge structure. At T'_A=500 ºC, the triangular graphene nanoislands had zigzag edges, what decrease its reactivity and partially inhibits the addition of single carbon atoms. The growth of the zz_h and zz_tedges is explained in detail in Figure 5.9.

Note that Figure 5.7.a shows STM images that cover a period of time of 76 min 17 s. This annealing time is much longer than the 20 minutes annealing studied in section 3.3 necessary to obtain triangular graphene nanoislands. Also, the annealing times required to obtain shape selected graphene nanoislands in next sections are shorter, in agreement with the results obtained in section 3.3. The need of longer annealing times here can be attributed to a specially lower carbon concentration in this preparation as indicated by the low graphene coverage. The minimum coverage obtained in the reproducible regime is 0.1 ML (section 3.2), while in this experiment we measure a coverage of 0.05 ML (in Figure 5.7). This unusually low carbon concentration could be due to a different sample history or an undetected error in the sample preparation procedure.

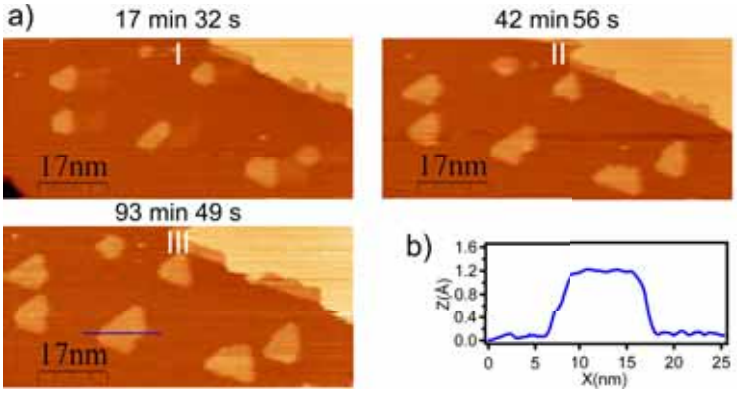

Figure 5.7: a) Evolution of a group of irregular graphene nanoisland to triangular graphene nanoislands at 500 ºC. b) Height profile along the blue line in (a.III)

5.3.2 Growth mechanism of a single graphene nanoisland at T'_A=500ºC

In the previous subsection we have seen the evolution of a group of graphene nanoislands at T'_A=500ºC. In this section the evolution of a single graphene nanoislands is studied in more detail.

A set of irregular graphene nanoislands is prepared by using the method described in section 3.2. The parameters used are D=1.8 L, T_R=500 ºC, and t_R=5 min. Once the irregular graphene nanoislands are formed, the sample is introduced in the STM an annealed at T'_A=500 ºC while acquiring STM images. In order to study the time evolution of the graphene nanoislands when annealed, we recorded 22 consecutive images of the same nanoislands with an acquisition time of 56 s and a bias voltage of 0.4 V. These images form a movie with a duration of 19 min 14 s which can be seen in [102].

Figure 5.8.a shows three STM images obtained at t'_A=16 min 12 s, 24 min 07 s and 32 min 55 s respectively. The images cover a period of time of 16 min 43s. Figure 5.8.a.I shows the graphene nanoisland with its initial shape at t'_A=16 min 12 s. The nanoisland has two defects that are visible as two bright points in the STM image. These defects can be used to determine the drift of the STM images. In Figure 5.8.a.II-III we observe the growth process of the nanoisland. At this temperature the nanoisland edges are straight, in contrast to the T'_A=450 ºC case where we observed irregular edges.

Figure 5.8.b shows an image that is the result of the superposition of the three STM images shown in Figure 5.8.a. As observed in the composed image, the growth of the nanoisland takes place maintaining the edge direction. The long edges are parallel to the symmetry directions $(1\bar{1}0)$, $(10\bar{1})$ and $(01\bar{1})$ of the Ni(111) surface as explained in detail in chapter 4.

The area of the island is represented in the graphic shown in Figure 5.8.c. The area

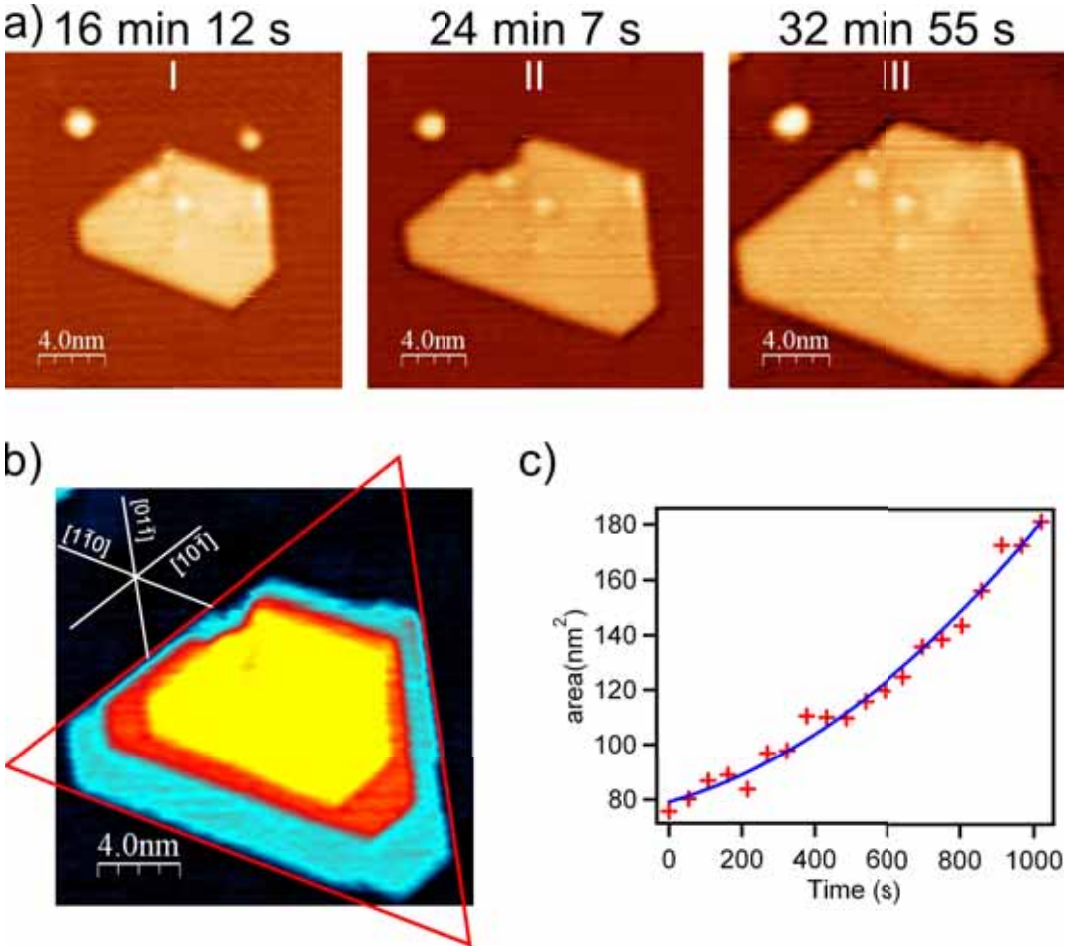

Figure 5.8: a) Three STM images showing the growth of a single graphene nanoisland at T'_A=500ºC. b) Superposition of the three STM images shown in (a), The colors represent the island area in different periods of time. c) Areal evolution with time of the graphene nanoisland. The blue line represents a quadratic fit.

has a quadratic behavior with time, as shown by using a polynomial curve of second order. This behavior is expected for a 2D growth with a constant growth rate at edges. In this case the perimeter of the nanoislands increases linearly with time, implying a quadratic increase of the area. Hence we can determine that the growth rate is constant with time. The island increase its size from 76 to 116 nm^2 in 530 s, which is very similar to the case of the graphene nanoisland grown at T'_A=450 ºC, where we observe a growth of 53 to 127 nm^2 in 520 s. The areal increase observed between 0 s and 500 s could be identified as linear, although the measurements obtained for further time reveal its quadratic nature. This explains why the areal increase observed in Figure 5.2.c appear to be linear. Also other factors such as neighboring islands proximity, which reduce the number of diffusing atoms, could affect.

It is important to mention that the preparation with T'_A=450 ºC was realized the day before the preparation with T'_A=500 ºC and no other experiments were realized in the Ni(111) crystal between them. Hence the history of the sample is almost the same.

5.3.2.1 Row-by-row growth of zigzag edges

Contrary to the T'_A=450 ºC case, at T'_A=500 ºC the edges of the nanoislands are straight and are supposed to have a zigzag structure as explained in chapter 4. These edges are chemically stable on a Ni(111) surface, and their reactivity is lower than the reactivity of irregular edges. In Figure 5.9 we show the growth mechanism of nanoislands with zigzag edges, which differs significantly from the growth mechanism of irregular edges.

The structure of the graphene nanoislands and their edges was studies in detail in chapter 4. As demonstrated, top-fcc is the most common stacking. Zigzag edges in top-fcc stacking can be divided in two groups with three-fold symmetry called zigzag hollow (zz_h) and zigzag top (zz_t) edges (Figure 4.6). Zz_h and zz_t edges are oriented 60º to each other. The zz_h edges have the outer carbon atom of the edge on top of the 3rd layer nickel atom and its dangling bond is pointing to the 1st layer nickel atom, giving some stability (Figure 4.11). In contrast, zz_t edges have the outer carbon atom of the edge on top of the 1st layer nickel atom and its dangling bond is pointing to the 1rd layer nickel atom, this structure is unstable and lays to the reconstruction observed at RT called $zz_t(57)$ (Figure 4.14). Due to the lower resolution of STM images obtained at high temperature no $zz_t(57)$ edges were observed at high temperature, but we can not discard its existence.

Growth of zz_h edges Figure 5.9.a shows a STM image obtained with a bias voltage of 1.1 V at T'_A=500 ºC and t'_A=30 min 16 s. The image has an acquisition time of 52.6 s and a resolution of 512 X 512 pixels. In the STM image we observe a graphene nanoisland with zigzag edges which is growing as illustrated in subsection 5.3.2. On the right of the island, marked with an arrow, we observe two kinks. The scanning direction of the STM tip is upwards, suggesting that the kink represents an increase of at least one row of hexagons in the nanoisland edge with respect to the previous lines. The two kinks observed in the image have the same orientation, hence they represent the same phenomena. All the images obtained in the growth process of this nanoisland have the same scanning direction and all the kinks observed in the STM images represents an increase of the island area. No kinks representing a decrease of a row of hexagons were observed during the growth process. We thus suppose that the growth of the nanoisland takes place by adding an entire row on a scale time much lower than the acquisition time of the STM images. Shu et. al. [99] studied the kinetics of graphene edges on transition metals and proposed a growth mechanism for zigzag edges in Cu(111). They observe that the addition of a carbon

hexagon to a zigzag graphene edge produces two armchair edges on each side of the hexagon. Due to the higher reactivity of armchair edges the graphene grows parallel to the zigzag edges propagating the graphene line though the nanoisland edge. Armchair graphene edges on Ni(111) are also highly reactive, as deduced from its absence in all graphene nanoislands (see chapter 4), for these reason we think that the growth mechanism of zigzag edges on Ni(111) could be a similar process.

The proposed mechanism is illustrated in Figure 5.9.b. The island show zigzag edges with low reactivity, but once a benzene ring is incorporated to such an edge two armchair edges are created, one on each side. The high reactivity of armchair edges induces the formation of another benzene ring on each armchair edge in an iterative process, which produces a growth along the edge with a velocity that is at least as fast as the scanning velocity in the vertical direction. The growth velocity is determined to be faster than 0.47 nm/s (the angle between the edge and the vertical direction is almost 0^{o}). However, the low probability of the incorporation of a benzene to the zigzag edge results in a small growth rate of the island in the perpendicular direction to the edge.

Growth of zz_t edges The incorporation of a benzene ring to the zigzag edge is a limiting factor of the growth. Obviously, the probability of the incorporation will depend on the type of zigzag edge. At T'_A=500^{o}C, the triangular shape of the graphene nanoislands indicates that the growth velocity of the zz_t edge is considerably higher. Figure 5.10 illustrates the formation mechanism of a triangular island from an hexagonal island. The growth velocity along the edge direction is considered to be much higher than in the perpendicular direction. For illustrative purposes the perpendicular growth velocity of the zz_t edge (v_t) has been considered to be the double of that of the zz_h edge (v_h). We can observe how the hexagonal island evolves in a triangular island with time. Note that the edges of the triangular island will always be truncated as long as the zz_h edge has a non zero growth velocity. This conclusion is valid for any initial shape, although stranger shapes will require more time to acquire a triangular form.

Inhibition of edge propagation by edge defect An additional proof of the nature of the growth mechanism described in this subsection is shown in Figure 5.11. It contains eight STM images obtained with a bias voltage of 1.1 V at T'_A= 500 ^{o}C. The first image is obtained at t'_A=24 min 07 s and the following images are obtained consecutively. Each image have an acquisition time of 53 s and the whole set of images covers a period of time of 6 min 8 s. In the first image we observe a graphene nanoisland with straight zigzag edges. In the second image a defect is created in the center of the lower edge, marked with an arrow. This defect has not the same nature of the kinks observed previously, since it does not generates an increase of the nanoisland area. As seen in the following images this defect does not act as a nucleation center, but acts as a barrier for the growth propagation along the edge.

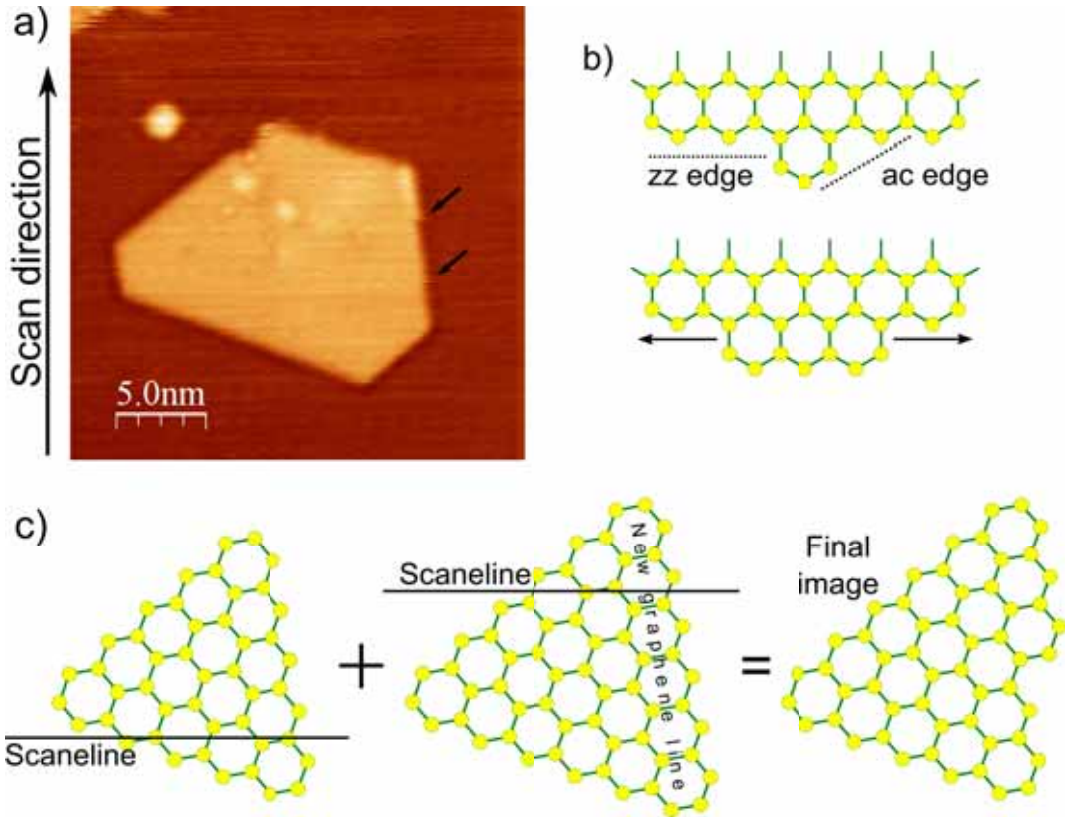

Figure 5.9: a) STM image of a graphene nanoisland at 500 ºC. The scanning direction of the image is upwards, each scanning line being horizontal. The two arrows indicate kinks in the edge of the nanoisland. b) Proposed growth mechanism for zigzag edges. c) Effect of the instant edge growth and the finite scanning time. At the beginning of the image acquisition the island has a certain area. Before the STM image is complete the island increases its area in a time interval much faster than the acquisition time. The resulting STM image is an island with a kink on its edge.

This results in a unbalance in the growth between the two sides of the defect due to the random nature of the edge growth, as observed in STM images from III to VI. However this barrier has a resistance limit and once the growth overflows the defect (image VII), the edge recovers its straightness quickly as seen in image VIII.

5.4 Annealing at 650 ºC

We have seen in section 3.3 that the annealing temperature has an important effect on the morphology of the nanoislands. The changes of the edge structure provoke a change in the growth mechanism that influences the growth rate and the final shape of the islands. By increasing the temperature from T'_A=450 ºC to T'_A=500 ºC the

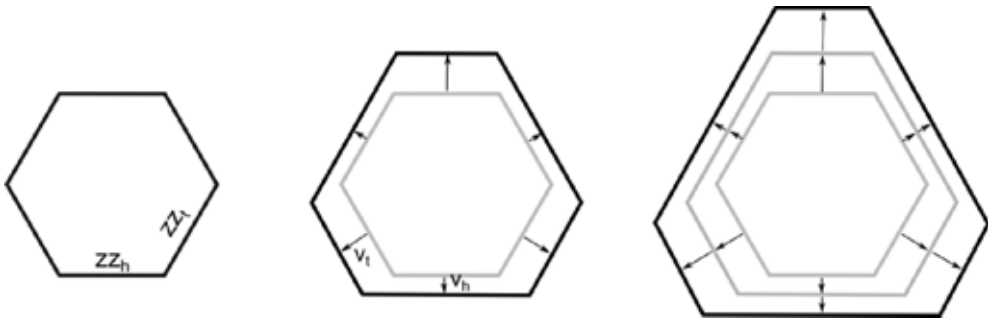

Figure 5.10: Effect of the different growth velocity of edges zz_h and zz_t on the island shape .

nanoislands adopt a triangular shape. As I will explain in this section, by increasing further the temperature the graphene nanoislands can adopt an hexagonal shape.

5.4.1 Growth mechanism of a single graphene nanoisland at T'_A=650ºC

We prepared a sample of graphene nanoislands on Ni(111) by following the method described in section 3.2. A clean Ni(111) single crystal was dosed with D=6 L of propene at RT. Once the dosing process is finished we heated the sample at T_R=500 ºC for t_R=5 min. This results in irregular graphene nanoislands on Ni(111). Then the sample is transferred to the STM and heated at T'_A=600 ºC while acquiring STM images to follow the evolution of the nanoislands at this temperature. Figure 5.12.a shows three STM images obtained with a bias voltage of 1.3 V. The images were obtained at t'_A=8 min 31 s, 9 min 26 s and 12 min 18 s respectively. In Figure 5.12.a.I we observe a graphene nanoisland. Although the nanoislands has an irregular shape, it maintains straight edges characteristic of the high temperature regime. In Figure 5.12.a.II-III we observe the evolution of the island with time, which leads to the hexagonal shape.

In Figure 5.12.a.III, we observe two kinks marked with arrows. Since the scanning direction of the STM image is downwards, these kinks are the result of the growth process as explained in detail in subsubsection 5.3.2.1. Hence the growth mechanism is expected to be the same as in the T'_A=500 ºC case. Note that the kinks are situated on consecutive edges, of zz_h and zz_t type. Hence the growth of the two zigzag edges takes place in a row-by-row manner. The adoption of a hexagonal shape by the nanoisland indicates that the growth velocity in the perpendicular direction of the zz_t and zz_h is very similar as we discuss in detail in the next subsection.

Figure 5.12.b represent the time evolution of the shape parameter of the nanoislands. The shape parameter is a measurement of the shape of the nanoislands, as explained in detail in subsection 3.3.1. As observed, the shape parameter evolves from a value of Σ=0.058, which corresponds to an irregular shape, to a value of Σ=0.064. The

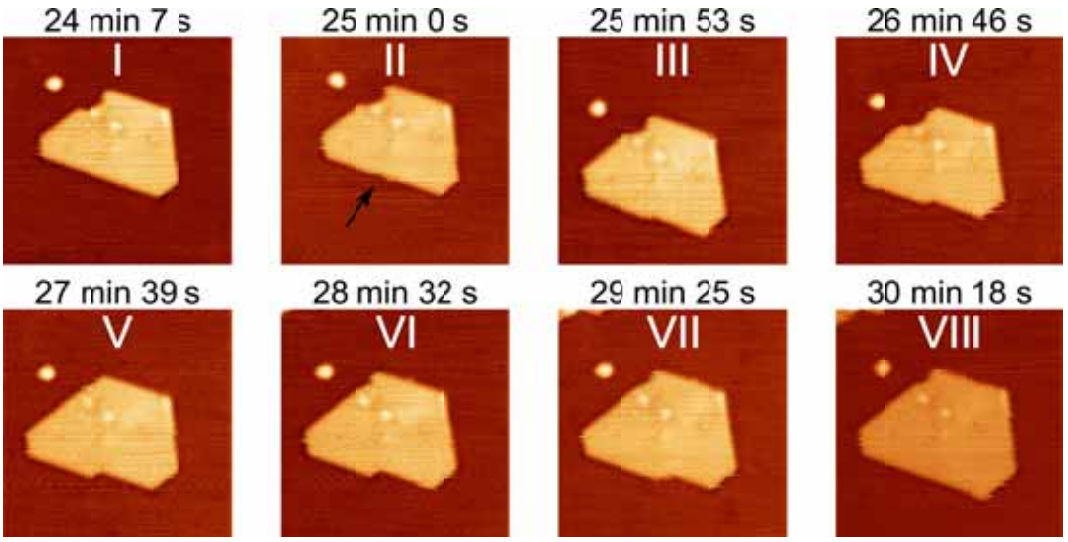

Figure 5.11: STM images of a graphene nanoisland evolution at 500ºC. In II a defect is created at the middle of the lower edge. This effect inhibits the propagation of the graphene growth along the edge resulting in a imbalance of the growth of the two sides of the edge. After a certain time the triangular shape is recovered.

final value of the shape parameter remains practically constant with time, which indicates a stability of the adopted shape of the nanoisland. The value of the shape parameter for a perfect hexagon is Σ=0.072. Our value is 11% smaller. This deviation is attributed to the different size of the edges that compose the hexagonal nanoislands, hence the island is not perfectly hexagonal, but close to it.

Note that the island has an intercalated nickel cluster in the left part. It is interesting to mention that the cluster grows with the nanoisland and contributes to maintain the hexagonal shape of the island. This phenomenon is in agreement with the observation in subsubsection 5.2.3.1, where we observe that the nickel clusters form only when most nickel atoms are surrounded by graphene.

5.5 Thermodynamical shape selection

The island shape and growth dynamics strongly depends on T'_A, as seen in previous sections. At T'_A=450 ºC, no zigzag edges are observed and the islands grow isotropically. At T'_A =500 ºC, zigzag edges are observed and the island edges grow with different velocities ($v_h < v_t$), which results in the adoption of a triangular shape as seen in Figure 5.10. At T'_A =650 ºC, zigzag edges are also observed, and the growth of different zigzag edges types occurs with the same velocity ($v_h = v_t$), which results in the adoption of an hexagonal shape. Therefore here we have to processes that determine the shape of the islands: the zigzag edge formation and the growth velocities of zz_h and zz_t edges.

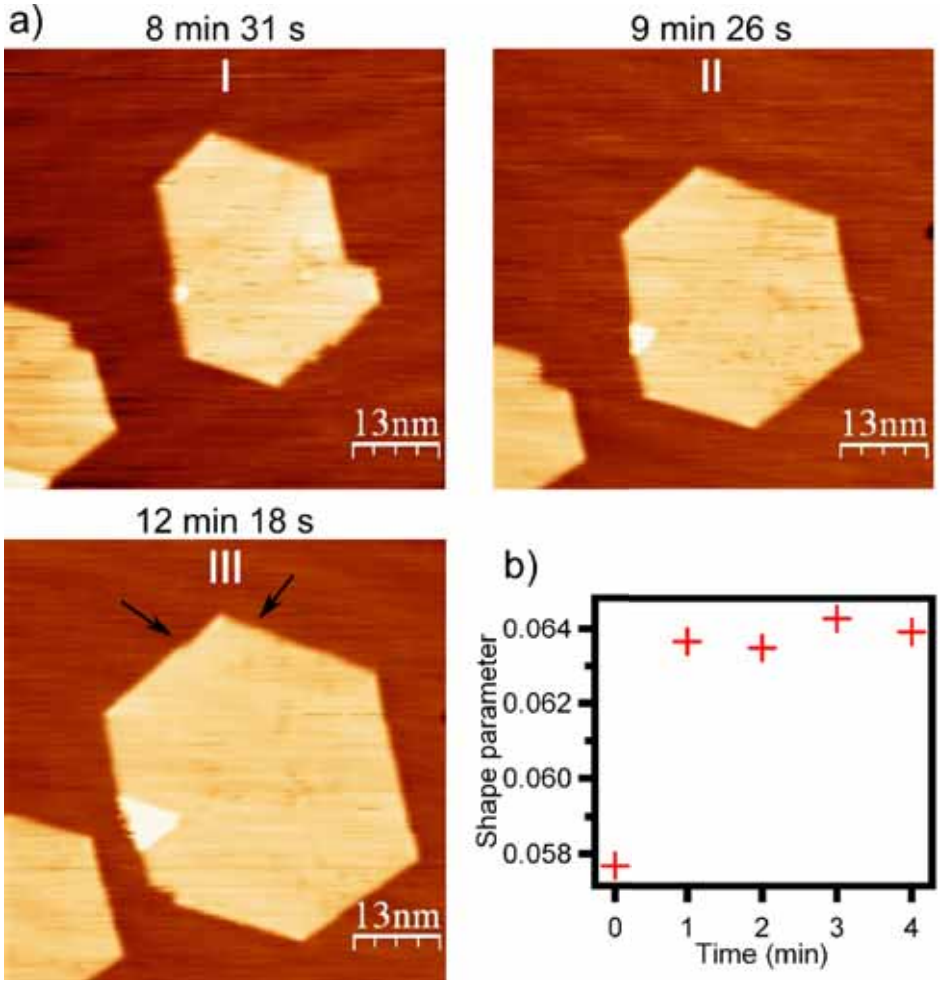

Figure 5.12: a) STM images of a graphene nanoisland evolution at 650 ºC. The nanoisland evolves from an irregular shape to an hexagonal shape. b) Time evolution of the shape parameter of the island.

Michely et. al. [104] studied the growth of Pt islands on Pt(111) surface. They observe a dependence with the temperature of the shape of the islands. Similarly to our system, they observe Pt islands that change its shape to triangular or hexagonal depending on the temperature. Jacobsen et. al. [105] explain the theoretical background of the phenomena. Their Monte-Carlo simulations obtain a good agreement with the experimental results. Their model was based on several temperature activated phenomena such as step diffusion, dimer dissociation, kink dissociation, etc, Those phenomena directly influence in a differentiated way the growth velocity of the different types of edges, and determines the shape of the islands. Graphene nanoislands on Ni(111) differ from metallic islands since carbon adatoms experience a large energy barrier to attaching to graphene edges, but we think that the system can be kinetically described in a similar way.

Suppose the probability of incorporating a new carbon hexagon to the system behave

as

$$P \propto d \cdot A$$

where P is the probability of incorporation, d i the carbon density and A the absorption probability.

At T'_A=450 ºC, the islands have irregular edges and the incorporation of new carbon atoms is dependent on the local geometry of each point. This leads to an isotropic growth resulting from many different absorption possibilities. When the temperature is increased the local defects of the edges heal [84] and the island adopts its lower configuration energy with zigzag edges.

At T'_A=500 ºC, the island has zigzag edges, but their grow velocity is different depending on its type. The zz_t edges are weakly bonded to the nickel substrate and the incorporation of carbon hexagons (see subsubsection 5.3.2.1) has a small energy barrier (E_t) [99]. If $E_t > k_BT$, where k_B is the Boltzmann constant, the energy barrier is overcame by the temperature, what results in a high growth velocity. On the other hand, zz_h edges are strongly bonded to the nickel substrate and the incorporation of carbon hexagons should have a high energy barrier (E_h). If $E_h > k_BT$, the incorporation of new carbon hexagon takes place by tunneling the barrier and is relatively rare, what results in a low growth velocity. The differences in the growth velocity of the edges is the reason for the triangular shape of the island.

When increasing the temperature to T'_A=650 ºC, the energy barriers are both overcame by system thermal energy ($E_h, E_t > k_BT$) and both edges have the same growth rate.

Note that the growth of the system is limited by the carbon density d, since the growth velocity observed is not increased when increasing the temperature (see Figure 5.2.c and Figure 5.8.c).

5.6 Summary

The growth and shape of graphene nanoislands on Ni(111) when heated was studied dynamically by high temperature STM. The growth occurs by incorporation of carbon segregated from the bulk to the surface. The incorporation of carbon has a temperature dependent behavior, which determined the growth mode and the final island shape. At 450 ºC, the carbon is incorporated isotropically and the islands grow uniformly. Increasing the temperature at 500 ºC leads to the formation of zigzag edges, which incorporate carbon selectively depending on its stacking with the substrate. Zz_h edges have a slow growth velocity, while zz_t edges grow fast, what results in the triangular shape of the islands. At 650 ºC the growth velocity of both zigzag edges is equal and the islands adopt an hexagonal shape.

When islands start to coalesce, nickel clusters appear between graphene islands. Those clusters have formation time below the time resolution of the STM and its growth mechanism was not determined. Graphene growth was also observed on nickel clusters.

6 Dynamics of the growth of a graphene monolayer on Ni(111)

The CVD growth on metals has been largely studied [96]. Graphene layers have been obtained on a wide variety of transition metals [96]. Ni(111) present the unique advantage to have a small lattice mismatch of only 1%. On Ni(111), the CVD growth have been obtained using different gas precursors such as methane, propene, ethylene, toluene, CO, etc. The crystal is heated and exposed to those gases, which supply the crystal with the necessary carbon that dilutes into the bulk[42] The graphene formation occurs by carbon segregation when decreasing the crystal temperature [106, 107] or when the crystal reach the supersaturation limit at a constant temperature [108][76]. Several in-situ experiment studied the graphene formation on Ni(111) [41, 97, 109, 81, 110]. Although valuable data was obtained, there is a controversy in the interpretation of the obtained results.

Regarding the early stages of the graphene monolayer growing there are many references of carbide formation. Controlling the Ni_2C formation is is important because it can inhibit the graphene formation [111]. Grüneis et. al. studied the CVD growth by means of photoemission. They monitored the photoemission signal peak evolution when exposing a Ni(111) crystal to propene at 511 ºC and found a peak at 283 eV at the initial stages of the exposition, before the graphene growth. The peak was assigned to propene fragments, atomic carbon and graphene edges, although they consider the possibility of belonging to Ni_2C which has an energy peak at 284 eV. With LEEM and AES experiments, Addou et. al. observe changes in Ni(111) at 500 ºC at the initial stages of ethylene exposition, which they attribute to the formation of Ni_2C domains [97]. . Although Ni_2C could transform into graphene [39], it is only reported to occur at long timescales and at 460 ºC, which results in graphene films with a high defect density [112]. Note that heating a Ni_2C covered Ni(111) at 500 ºC in UHV conditions results in the dissolution of the carbide. Hence, there is a controversy in the products of initial stages of the CVD reaction, and the need of more conclusive studies is evident.

In this chapter we report STM measurements of all stages of the CVD growth of graphene on Ni(111) using propene as precursor gas at different temperatures. We found that Ni_2C layers form at the initial stages of the CVD reaction and cover the whole surface. Ni_2C is stable at temperatures below 600 ºC under propene atmosphere but unstable under UHV conditions. Graphene growth occurs in samples with enough carbon concentration after several minutes and does not need a

continuous exposure to propene.

6.1 Experimental details

All the experiment described in this chapter were performed in the high temperature experimental setup (subsection 2.3.2). In the experiments referred in this chapter a clean Ni(111) sample was used and maintained in UHV conditions. The Ni(111) crystal was cleaned by repeated cycles of Ar^+ sputtering followed by annealing at 800 ºC for 1 minute until the surface presents no traces of carbon contamination by means of STM inspection. Topographic STM images of the surface were obtained using the Aarhus 150 STM HT and processed using the WSxM software [79].

Figure 6.1 describes the procedure used to prepare the sample used in the experiments described in this chapter. The procedure can be summarized in 6 steps:

1. The clean Ni(111) crystal was placed in the Aarhus 150 STM HT and heated at a temperature T'_R (Figure 6.1.1).
2. Once the temperature was stabilized we performed STM measurements to check the surface clearness and find an area with the desired topography (Figure 6.1.2).
3. At time t=0 a leak valve was opened filling the chamber with propene at controlled pressure (Figure 6.1.3).
4. At t=t'_R the leak valve was closed and the chamber recovered its base pressure. The sample was maintained at temperature T'_R until the CVD reaction was finished. (Figure 6.1.4).
5. After that, at t=t_{RT} the heating was stopped and the sample cooled down to RT (Figure 6.1.5).
6. STM measurements were performed at RT to study the final effect of the CVD reaction (Figure 6.1.6).

The Aarhus 150 STM HT allows us to perform STM measurements in all the steps with constant temperature of the CVD reaction described in Figure 6.1.

The surface temperature was measured using a thermocouple integrated in the sample holder, which gives a temperature value T_{tc}. To use a single temperature scale in all experiment in this thesis, a calibration function $f(T_{tc}) = T_p$ was determined experimentally as explained in section 5.1. The temperature values in all chapters in this thesis are given using the pyrometer scale (T_p).

In previous chapters, the dose supplied to the sample was calculated by the time integration of the chamber pressure. In this chapter, the dose is calculated by directly multiplying the chamber pressure by t'_R due to technical limitations. Note that this procedure overestimated the final dose D, since the chamber pressure takes a certain time to reach the desired value once the leak valve is opened.

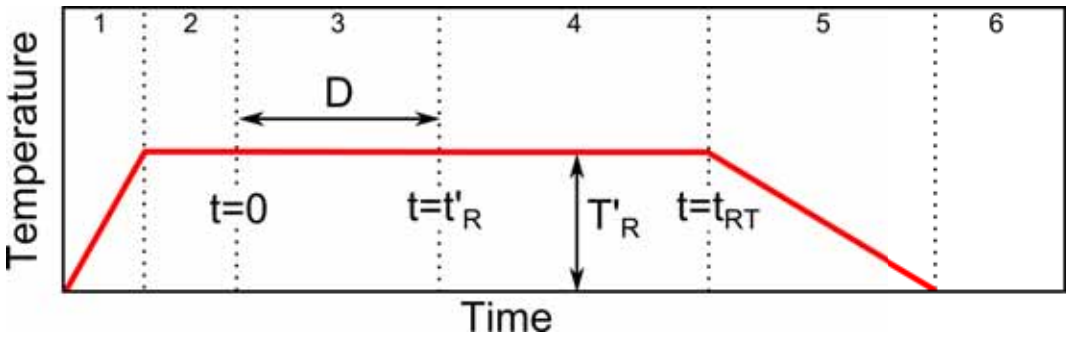

Figure 6.1: Scheme of the CVD reaction used. The preparation is divided in six main steps. 1) The clean Ni(111) surface is placed in the Aarhus 150 STM HT and heated to a temperature T'_R. 2) The sample temperature is stabilized. 3) The leak valve is opened (t=0) and the chamber is filled with propene at a defined pressure, 4) Once the desired dose D is reached, the leak valve is closed and the chamber recovers its base pressure. 5) Heating is turned off and the sample cools down. 6) The sample reaches RT. At all the steps with constant temperature (2,3,4 and 6) STM images were acquired.

6.2 CVD reaction at 500 ºC

In order to study the CVD reaction that takes place on the Ni(111) surface, we performed several in-situ STM measurements at different values of T'_R corresponding to the steps described in section 6.1. At T'_R=500 ºC, the CVD reaction results in the formation of both graphene and Ni_2C, which are the two possible reaction products. For that reason T'_R=500 ºC is a good temperature to study in detail the growth mechanism which produce both carbon phases. In this section we present a detailed study on the CVD reaction characteristics, as well as their dependence on parameters such as the propene pressure and dose.

6.2.1 The Ni(111) at 500 ºC

The behavior of the Ni(111) is an important factor in the study of CVD reactions on this surface, therefore it must be characterized previously. Figure 6.2 shows the characteristics of a Ni(111) surface at 500ºC. STM images showed in Figure 6.2.a,b are obtained in the same area with a time separation of 53 s. Thermal drift is observed but it is small enough to have no significant effect on our analysis. The fuzzy appearance of the step edges observed in the STM image obtained at 500 ºC (Figure 6.2.d) shows that the steps are mobile and that nickel atoms continuously attach and detach to the steps, although no significant modification of the shape of the terraces is observed. In comparison, Figure 6.2.e shows an STM image of a Ni(111) step at RT where we can observe that the step edge is well delimited.

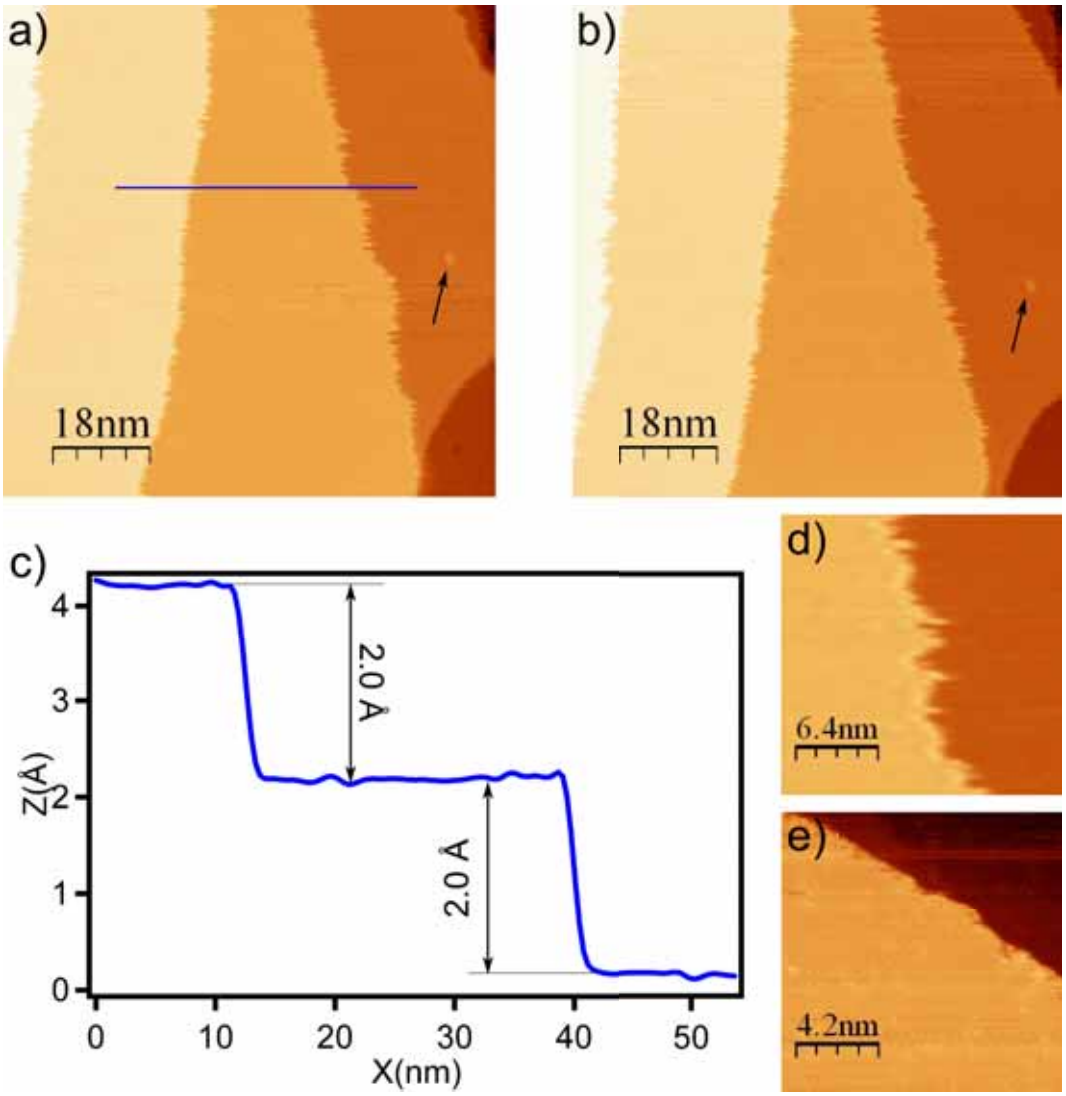

Figure 6.2: Mobility of nickel steps at 500 ºC. a,b) STM images of a clean Ni(111) surface at 500 ºC obtained in the same area with a time separation of 53 s. The arrow indicates an adsorbate used to determinate the thermal drift. c) Height profile obtained along the blue line in (a). d,e) STM image of a nickel step edge at 500ºC (d) and RT (e). The arrow indicates a contamination trace.

6.2.2 Ni_2C formation at 500 ºC

The first step of the CVD reaction observed at 500 ºC is the formation of a Ni_2C layer. Although Ni_2C is not stable at 500 ºC in UHV conditions (see chapter 3)[39] we find it to be stable in a propene atmosphere. The identification of Ni_2C can be easily done by observing its characteristic stripped pattern [80, 89].

Figure 6.3 shows the dependence of the Ni_2C-nickel topography on the STM bias voltage at RT. STM topography at high temperature presents the same bias dependence. STM images shown in Figure 6.3.a,b are obtained at a bias voltage of 70 mV and 1 V respectively. For a bias voltage of 70 mV, the height profile obtained along the blue line in Figure 6.3.a shows an apparent height of 0.16 Å. When increasing the bias voltages up to 2 V a decrease of the height of Ni_2C with respect to nickel is observed, as expected for an insulating material such as Ni_2C. At a bias voltage of 1 V the apparent height of the Ni_2C with respect to nickel is of -0.33 Å.

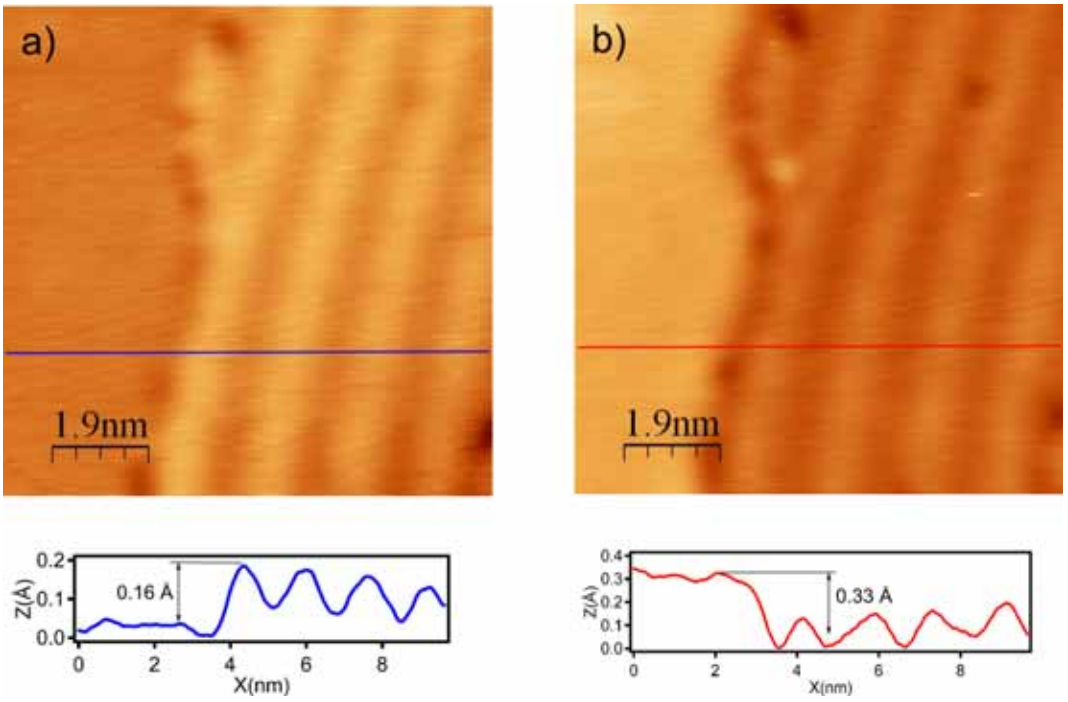

Figure 6.3: Bias dependent topographic contrast of Ni_2C layers. a) STM image obtained with a bias voltage of 70 mV of the lateral interface between a Ni(111) terrace and the Ni_2C layer. b) STM image of the same area obtained with a bias voltage of 1 V.

In the following , we describe the reactions that take place during step 3 of the preparation process. In the first instants of the dosification process (step 3), the surface reacts and forms a Ni_2C layer. The details of the Ni_2C layer formation are described below.

6.2.2.1 Reaction at terraces

Figure 6.4 shows STM images acquired during the formation of the Ni_2C layer. All STM images in Figure 6.4 are obtained using a bias voltage of 0.8 V. STM images shown in Figure 6.4 have an acquisition time of 26 s. The drift of the system was determined by measuring the position of the adsorbates in consecutive images. The STM image shown in Figure 6.4.a corresponds to a Ni(111) surface in UHV environment at t=0. The bright dots observed in the image correspond to adsorbates. During the image acquisition we open the leak valve and increase the propene pressure up to $1 \cdot 10^{-6}$ mbar. Figure 6.4.b shows an STM image started at t=26 s (D=26 L) with STM tip scanning downwards (the upper lines of the image are acquired previous to the lower lines); we can observe a decrease of the surface height in certain areas of the surface. This decrease is due to a chemical reaction attributed to the formation of a Ni_2C layer. The image inset in the right of Figure 6.4.b shows a zoomed in area with increased contrast where we can distinguish the characteristic structure of Ni_2C [80, 89] with a periodicity of 16.5 Å. The chemical reaction starts at point 1 (t=28.9 s, D=28.9 L). As the tip moves downwards we observe that the reacted surface propagates. At point 2 we observe the creation of another Ni_2C domain, which indicates that the reaction can start simultaneously in more than one point. Note that the starting point of the reaction takes place in the middle of a terrace, without a terrace step. . At point 3 we observe a new nickel terrace step emerging from the left part of the image, which was not there before the reaction as seen in Figure 6.4.a. Figure 6.4.c shows and STM image of the same region started at t=52 s with the STM tip scanning upwards. The new nickel step does not change position or shape with respect to the image in Figure 6.4.b, and remains unchanged in STM images obtained up to 3 minutes later (not shown). At t=58.9 s we observe a small unreacted area, marked with an asterisk, which disappears at t=116s (image not shown), hence the completion of the Ni_2C layer in the scanned area takes places in 87±29 s. Figure 6.4.d shows a height profile along the red line in Figure 6.4.d. The reacted surface (attributed to Ni_2C) decreases its height with respect to a nickel by 0.5 Å, which is consistent with the height decrease observed when scanning at high bias voltages (Figure 6.3). The step situated in the lower part of the image has a height of 2.5 Å. This height difference is attributed to a jump between a double nickel step and a Ni_2C layer.

After the reaction of propene with the nickel surface two main changes are observed. The formation of Ni_2C in some areas of the surface, which results in lower apparent height; and a nickel mass transport due to the formation of Ni_2C, which implies a 20% reduction of the nickel density on the surface top layer [80]. Note that the reaction starts in multiple points almost simultaneously and then propagates through the surface. Ni_2C formation on a Ni(111) surface was also observed by Addou et. al. [97] in the initial stages of the reaction when dosing ethylene at a pressure of $1.3 \cdot 10^{-6}$ mbar on Ni(111) at a temperatures ranging from 500 ºC to 600 ºC.

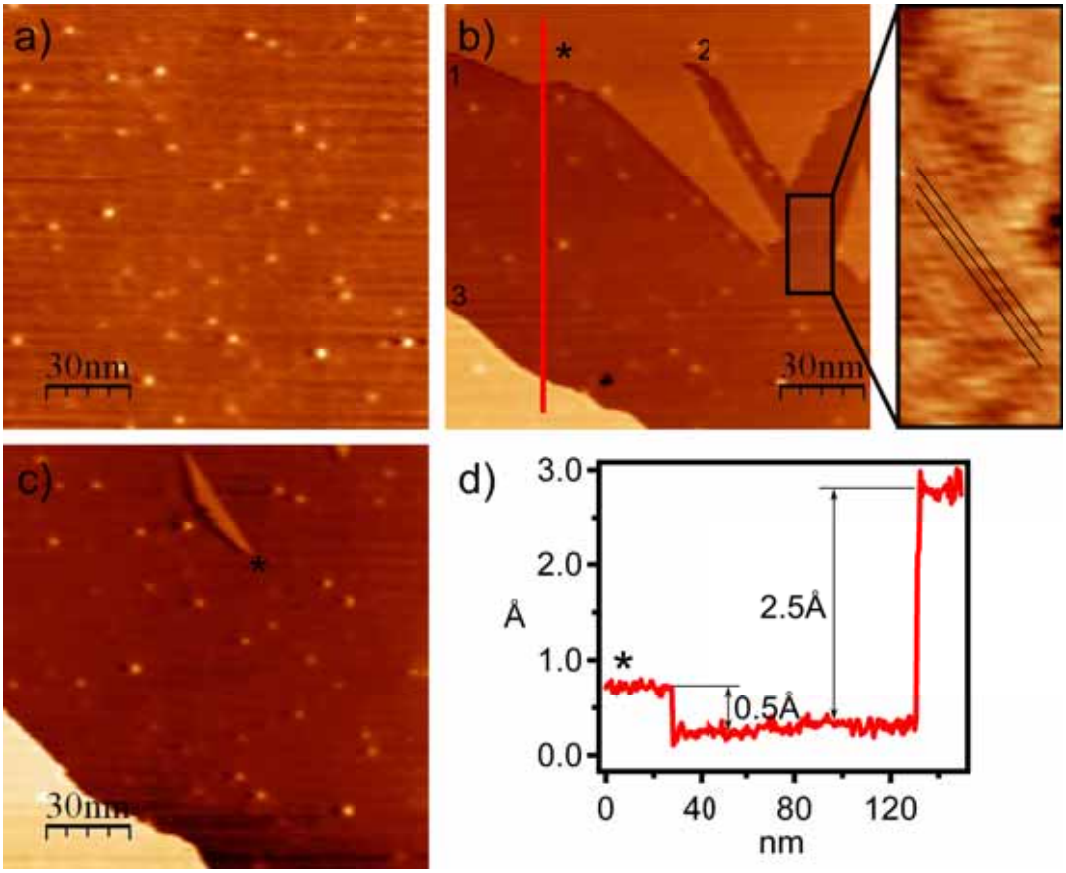

Figure 6.4: Real time growth of Ni_2C on flat nickel terraces. Consecutive STM images are obtained on the same area during propene dosing at $1 \cdot 10^{-6}$ mbar at T'_R=500 ºC using a bias voltage of 0.8V. The acquisition time is 26 s. Image (a), started at t=0 s with scanning direction upwards, shows the unreacted Ni(111) surface, with some adsorbates used to characterize the thermal drift. Image (b), started at t=26 s with scanning direction downwards, shows a Ni(111) surface (upper part) that reacts with propene and forms a Ni_2C layer (point 1 and 2) while the tip is scanning. The enlarged image on the right shows the striped pattern typical of Ni_2C. A nickel terrace appears in the lower part of the image. Image (c), started at t=52 s with scanning direction upwards, shows a surface mostly covered by a Ni_2C layer, except in the region marked with an asterisk. d) Height profile obtained along the red line in (b).

6.2.2.2 Nickel mass transport at the surface

The mass transport observed in Figure 6.4 indicates that the carbon atoms supplied by propene penetrates the first nickel atomic layer during the CVD reaction to form a Ni_2C monolayer. Figure 6.5 illustrates the mass transport induced by the CVD process.

Figure 6.5.a shows a STM image of a clean Ni(111) surface at 500 ºC in UHV conditions. Figure 6.5.b shows an STM image of the same area once the leak valve was opened and the propene partial pressure reached $1 \cdot 10^{-6}$ mbar (t=0). The scanning direction is upwards. Figure 6.5.c shows the same STM image with increased contrast in order to observe the Ni_2C striped pattern. The acquisition time of the STM image is 52.6 s. At t=18.7 s (D=18.4 L) the Ni_2C growth starts. At the same time, a notable step mobility is observed. The dashed lines drawn in Figure 6.5.b shows the position of the terrace step edges prior to the reaction. Figure 6.5.d shows an STM image of the same area, as demonstrated by the defect marked with an arrow in Figure 6.5.b and d, started at t=187 s where the terrace has expanded and all the scanned area is covered by Ni_2C. It is important to mention that the Ni_2C growth does not occur on all terraces at the same time.

Note that the clean Ni(111) surface showed in Figure 6.5.a do not show adsorbates comparing with the one described in subsubsection 6.2.2.1, however the Ni_2C growth occurs in the same manner, which supports the statement that the adsorbates observed by STM do not act as nucleation centers for Ni_2C.

6.2.2.3 Pressure threshold

Ni_2C was reported to be unstable at 500 ºC [39] and its growth was not expected at 500 ºC due to the results obtained in previous experiments (see section 3.2) . These experiments were performed in UHV conditions. However the Ni_2C layers grown in the experiments performed in this chapter were observed while exposing the Ni(111) surface to a propene atmosphere of $1 \cdot 10^{-6}$ mbar. Also Amara et. al. [100] predict a stability of the carbidic layer depending on the chemical potential, which should increase with the propene dose. To demonstrate the dependence of the Ni_2C layer formation and stability to propene pressure and dose we exposed a hot Ni(111) sample at different propene pressures.

Figure 6.6 shows the evolution of clean Ni(111) at 500 ºC when exposed to a controlled dose of propene. All STM images in Figure 6.6 were obtained with a bias voltage of 0.8 V. The thermal drift was compensated following the impurity marked with an asterisk in Figure 6.6.a and Figure 6.6.b (observable when increasing image contrast). Figure 6.6.a shows an STM image of clean Ni(111) at 500 ºC in UHV conditions (no propene) started at t=-105 s. Just after finishing this STM (t=0 s), we dose propene at a pressure of $1 \cdot 10^{-8}$ mbar. No changes in the surface were observed after 9 minutes, which corresponds to a dose exposure of D=5.4 L. After

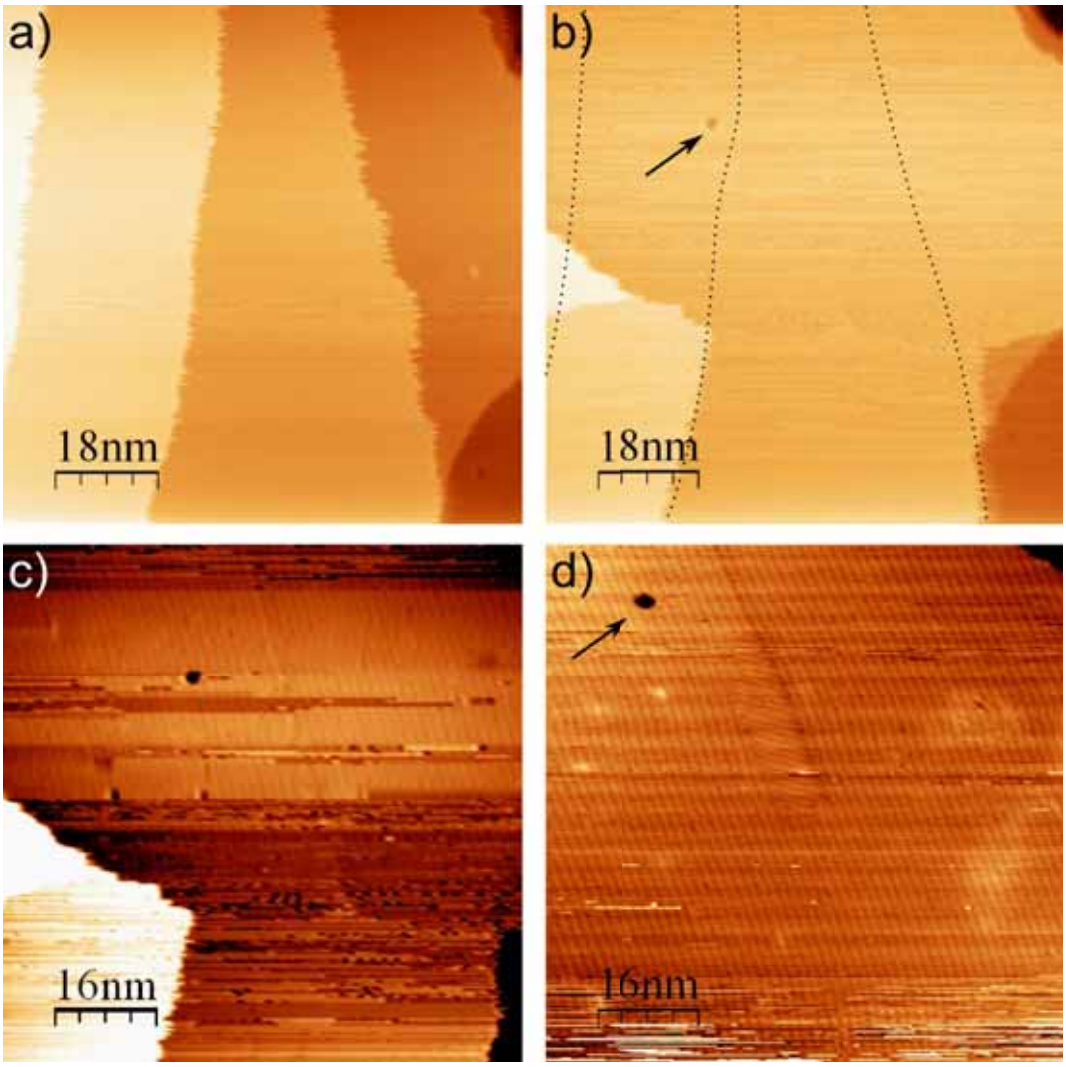

Figure 6.5: Nickel mass transport during Ni_2C formation. Consecutive STM images are obtained on the same area during propene dosing at $1 \cdot 10^{-6}$ mbar at T'_R=500 ºC using a bias voltage of 1 V. Image (a), started before the leak valve was opened, shows the unreacted Ni(111) surface. Image (b), started at t=0 s with a scanning direction upwards and an acquisition time of 52.6 s, shows the Ni_2C formation reaction in the middle of the STM image acquisition characterized by the terrace steps mobility. The dashed lines show the position of the terrace steps prior to the reaction start. c) The same STM image showed in b) with increased contrast to observe the striped pattern. Image (d), started at t=187 s, shows the surface completely covered by a Ni_2C layer. The arrow indicates a defect also present in (b) used to identify the surface area.

that we increased the propene pressure up to $2 \cdot 10^{-7}$ mbar. This pressure change was not abrupt and the pressure increased smoothly from $1 \cdot 10^{-8}$ mbar.

Figure 6.6.b shows an STM image of the same area started at t= 946 s (accumulated dose D=87 L). As observed in the STM image no changes are observed. Figure 6.6.c shows an STM image started at t=1051 s. The tip position is the same than in Figure 6.6.b and only a small displacement caused by thermal drift is observed due to the small time difference between the two images. Starting at t=1099 (accumulated dose D=118 L) s we observe a change in the Ni(111) surface attributed to the Ni_2C growth reaction. The dashed line in Figure 6.6.c indicates the expected position of the terrace step if no mass transport would occur. Note that the expansion of the Ni_2C terrace stops when it reaches the next terrace step.

Figure 6.6.d shows a height profile obtained from the STM image in Figure 6.6.b. The height of each step is 2.0 Å, confirming that the surface has not reacted when exposed to a propene atmosphere of $1 \cdot 10^{-8}$ mbar. Figure 6.6.e show a height profile through the blue line in Figure 6.6.c. We can identify the effect of the Ni_2C growth in the apparent height of 0.5 Å. Figure 6.6.f shows the height profile along the green line in the left part of Figure 6.6.c. The height changes of 2.0 Å, 1.5 Å and 3.5 Å are attributed to a nickel terrace step, a Ni_2C layer, and a Ni_2C layer on a nickel terrace respectively.

The experiments performed in this subsection suggest that a Ni_2C layer does not form when the propene pressure is equal or lower than $1 \cdot 10^{-8}$ mbar. However, increasing the propene pressure up to $2 \cdot 10^{-7}$ (for 9 minutes) results in the formation of a Ni_2C layer on the Ni(111) surface. Hence we can conclude than the formation of the Ni_2C layer does not occur spontaneously when the crystal is exposed to propene, but it needs to reach a certain carbon concentration on the surface to start the growth reaction and make Ni_2C stable at 500 ºC. This phenomena was also reported on ethylene CVD reaction on Ni(111) in similar conditions [97]. Note that the dose at which the reaction starts is highly dependent on the propene pressure. While the doses needed for propene pressure of $1 \cdot 10^{-6}$ mbar are 28.9 L and 18.4 L (at subsubsection 6.2.2.1 and subsubsection 6.2.2.2 respectively), for lower propene pressure of $2 \cdot 10^{-7}$ mbar a considerable higher dose is required (118 L), what demonstrates that propene pressure is a determinant factor. At 500 ºC the surface concentration of carbon depends largely on the propene pressure and is determined by the difference between propene molecules supplied from the gas phase and those that desorb from the surface (see subsection 3.2.1) and the carbon diffusion to the bulk. This dynamic equilibrium situation makes Ni_2C stable only where there is an excess of carbon at the surface.

6.2.3 Ni_2C dilution to bulk

As demonstrated above, the growth and stability of the Ni_2C layer depends on the propene pressure and dose at which the crystal is exposed. In this subsection, we

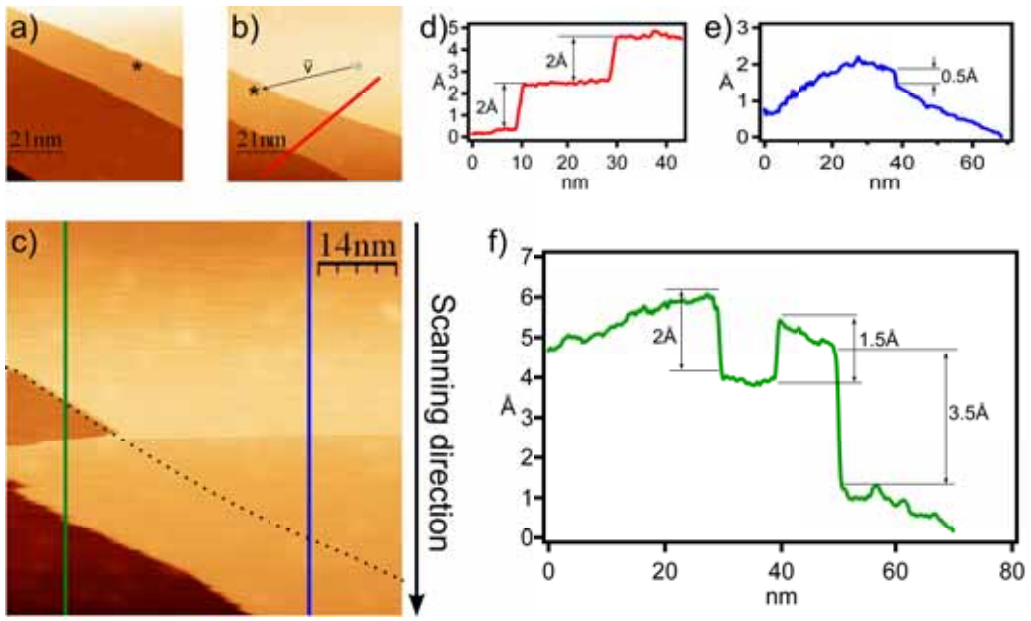

Figure 6.6: Dependence of Ni_2C reaction with the propene partial0 pressure. a) STM image of a clean Ni(111) surface started at t=-105 s. When the image end (t=0s) we fill the chamber with propene at a pressure of $1 \cdot 10^{-8}$ mbar for 9 minutes. At t=50 s the pressure is increased up to $2 \cdot 10^{-7}$ mbar. b) STM image started at t=946 s. No reaction is observed. c) STM image started at t=1051 s. At the middle of the image the Ni_2C formation is observed. The dashed line indicates the position of the terrace edges prior to the CVD reaction. d) Height profile obtained along the red line in figure (b). e) Height profile obtained along the blue line in figure (c). f) Height profile obtained along the green line in figure (c)

present the results obtained in the first instants of the step 4 of the preparation procedure (see section 6.1). After closing the propene leak valve, the chamber recovered UHV conditions, which resulted in the dissolution of the Ni_2C layer to the bulk. The dissolution of the Ni_2C was studied by means of high temperature STM. Figure 6.7 shows the results obtained.

All STM images shown in Figure 6.7 were obtained using a bias voltage of 1 V, at a sample temperature of 500 ºC and with upwards scanning direction. Figure 6.7.a shows an STM image of a Ni_2C layer at 500 ºC in a propene atmosphere of $1 \cdot 10^{-6}$ mbar . At t=360 s (D=360 L) the leak valve was closed and the chamber recovers its base pressure. Note that the pressure decrease toke place smoothly. STM image shown in Figure 6.7.b was started at t=652 s. At this moment the sample underwent an abrupt change. In the STM image we observe two distinct regions. The right part of the image is assigned to a Ni_2C layer, thanks to its characteristic striped pattern, while the bright region in the left of the image is attributed to nickel due to its relative height of 0.4 Å with respect to the Ni_2C layer. Normally the

nickel-Ni_2C interface follows the same direction of the striped pattern observed in the Ni_2C layer (see Figure 6.3), however in that case the nickel-Ni_2C interface has an oblique direction with respect to the striped pattern, which could indicate an interface mobility while scanning. Note that the scanning direction is upwards, hence the image suggests that the nickel is substituting the Ni_2C layer, in agreement with the fact that the Ni_2C phase is unstable at 500 ºC in UHV conditions [39]. Figure 6.7.c shows an STM image of the same area started at t=796 s. The surface, previously covered by Ni_2C, has completely transformed in a clean Ni(111) surface with no traces of Ni_2C. The Ni_2C phase is indeed not stable at 500 ºC if no propene is continuously offered to the surface.

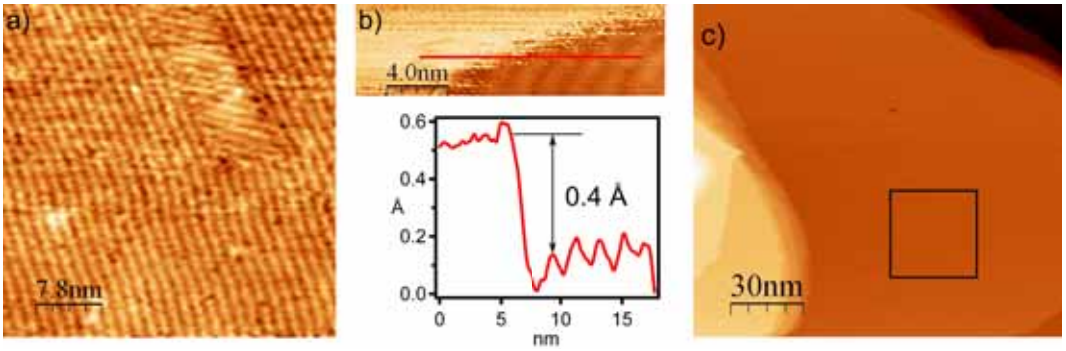

Figure 6.7: Dissolution of Ni_2C into bulk. a) STM image of the sample surface fully covered by a Ni_2C layer at T_R=500 ºC. b,c) STM images of a nickel-Ni_2C interface obtained at t=652 s and t=711 s respectively. The images were obtained after closing the propene leak valve in UHV conditions, using a bias voltage of 1 V. The scanning direction is upwards, indicating a dilution of the Ni_2C layer. Height profiles are obtained along the lines in STM images. d) Ni(111) surface obtained at t=796 s. no traces of Ni_2C are observed The black box indicates the area in where (a) was obtained.

6.2.4 Graphene growth at 500 ºC

Graphene is known to grow on samples kept in a propene atmosphere [113], hence the graphene growth is driven by a combination of the carbon concentration and the time at which the sample is heated. However the presence of a carbon-containing atmosphere is not a necessary condition to growth graphene, but the presence of carbon diluted in the bulk.

In this subsection we show the growth of a graphene monolayer on a Ni(111) sample by means of in-situ high temperature STM measurements. We show the evolution of a Ni(111) sample when maintained at 500ºC in UHV conditions for a long period of time after the dosing process and dissolution of the Ni_2C layer, corresponding to the late step 4 of the CVD reaction showed in section 6.1. After 5 minutes of dosing

propene at a pressure of $1 \cdot 10^{-6}$ mbar (D=300 L), the propene dosing is stopped and the sample is maintained at 500 ºC in a UHV environment. All STM images showed in this subsection are obtained in the same preparation.

The growth mode of graphene nanoislands when heated (chapter 5) indicate that graphene act as a "trap" for free carbon atoms. The growth of graphene monolayer seem to follow a similar behavior as we will show in this section. For that reason we believe that the growth of graphene monolayer is driven by the availability of free carbon which incorporates at the graphene edges and not by the incorporation of carbon coming directly from the propene molecules. This incorporation has a potential barrier that has to be overcome[99], for that reason the incorporation of carbon to graphene edges only occurs at high temperature.

6.2.4.1 Growing front

STM images in Figure 6.8 are obtained once the chamber has recovered its base pressure and using a bias voltage of 0.5 V. Each STM image shown in Figure 6.8 has an acquisition time of 65.7 s, and all images were obtained consecutively. Figure 6.8.a shows an STM image started 7 minutes after the dosing end (t=12 min) once the Ni_2C layer has completely dissolved into the bulk. In the images sequence shown in Figure 6.8.c we observe a new phase growing with an average velocity of 0.35 nm/s. This new phase is attributed to a graphene monolayer. Figure 6.8.d shows a STM image obtained at t=18 min. The graphene layer has a height of 1.2 Å (Figure 6.8.b) and a granulated fine structure due to the combination of the graphene layer imperfections and a multiple tip effect. The detailed atomic structure cannot be identified due to the multiple tip effect. (see Figure 6.9). Since the STM image shown in Figure 6.8.a was obtained 7 min after the dosing ends (t=12 min), we can conclude that the graphene growth does not need a continuous dose offered to the crystal but to hold the sample at high temperature. The carbon necessary to form the graphene layer have to come from the crystal bulk, because its the only carbon source available. Hence the crystal has to have a certain amount of carbon dissolved into the bulk obtained during the dosing process. The heating of a Ni(111) sample without previous dosing of propene does not result in the formation of graphene. Once the surface is fully covered by graphene no changes are observed in a scale time of several minutes.

One could think that the initial surface is covered by a Ni_2C layer that transforms directly to graphene as observed by Lahiri et. al. at 400 ºC[39]. However this statement is highly improbable due to the fast dilution of the Ni_2C at 500 ºC as observed in subsection 6.2.3, also observed in the Lahiri's experiments. Anyway, the carbon density in the surface in the graphitic phase is 5 times the carbon density in the carbidic phase. Since the graphene covers the whole surface, an additional carbon source would be necessary, which implies that the carbon diluted in the bulk has an indispensable role in the graphene growth on Ni(111) in any case, in agreement with previous experiments using isotope labeling of carbon [42]. A

similar graphene growth behavior have been previously reported with higher growth velocities [97, 41] in experiments with higher carbon availability, which indicates that in our CVD reaction the graphene growth velocity is limited by the availability of free carbon atoms.

6.2.4.2 Surface stability and bias dependent structure

Once graphene growth terminates, the surface remains stable and no changes are appreciated after several minutes allowing us to determinate the bias dependent structure of the graphene monolayer.

Figure 6.9 shown STM images of the graphene layer obtained at different bias voltages. Figure 6.9.a-c were obtained consecutively. In the STM image shown in Figure 6.9.a and obtained at 2 V we observe that the surface is all covered with graphene. The fine structure of the graphene layer shows some imperfections in the form of impurities with a height of ≈0.5 Å. Figure 6.9.b shows an STM image of the same region obtained with a bias voltage of 3 V and show a dendritic structure of the layer, which has been observed previously for such voltages *[114]*. Note that the dendritic structure is also observed in the surface holes. Figure 6.9.c shows an STM image of the same region obtained with a bias voltage of 4 V. We observe that the dendritic structure vanishes, suggesting that it is related to an electronic state around 3 V as observed by Mugarza et. al. [114] .Figure 6.9.d shows the area market with a black rectangle in Figure 6.9.a measured at 2 V and 3 V. We can observe that the nickel intercalated atoms, which appear as bright point at 2 V, are situated in the dark areas measured at 3 V. However, the dendritic structure does not invert its contrast as nickel atoms does, what indicates it is not related with nickel impurities. Mugarza et. al. [114] realized spectroscopic measurements on this dendritic structure and found that it is related to the stacking of the graphene with the nickel substrate. Areas with a on-top stacking (see chapter 4) have a surface state around 2.5 V, which increase its conductivity at higher bias voltages. Areas with a different stacking does not have this state, what results in a lower conductivity.

6.2.5 Sample surface after cooling to RT

In previous subsections we have seen that the products of the CVD reaction are the formation of a Ni_2C layer in the initial instant of the propene exposition and a graphene monolayer that grows several minutes later than the carbide phase. Although the surface seems stable at 500 ºC after the graphene monolayer growth, we found that the cooling process could introduce further changes. For these reason STM measurements were performed at RT on a sample resulting from the preparation with T'_R=500 ºC, t'_R=6 min and D=360 L, t_{RT}=41 min 24 s. In this preparation the heating was turned off at the same time that we closed the leak valve. The results obtained correspond to the step 6 explained in section 6.1 and are shown in

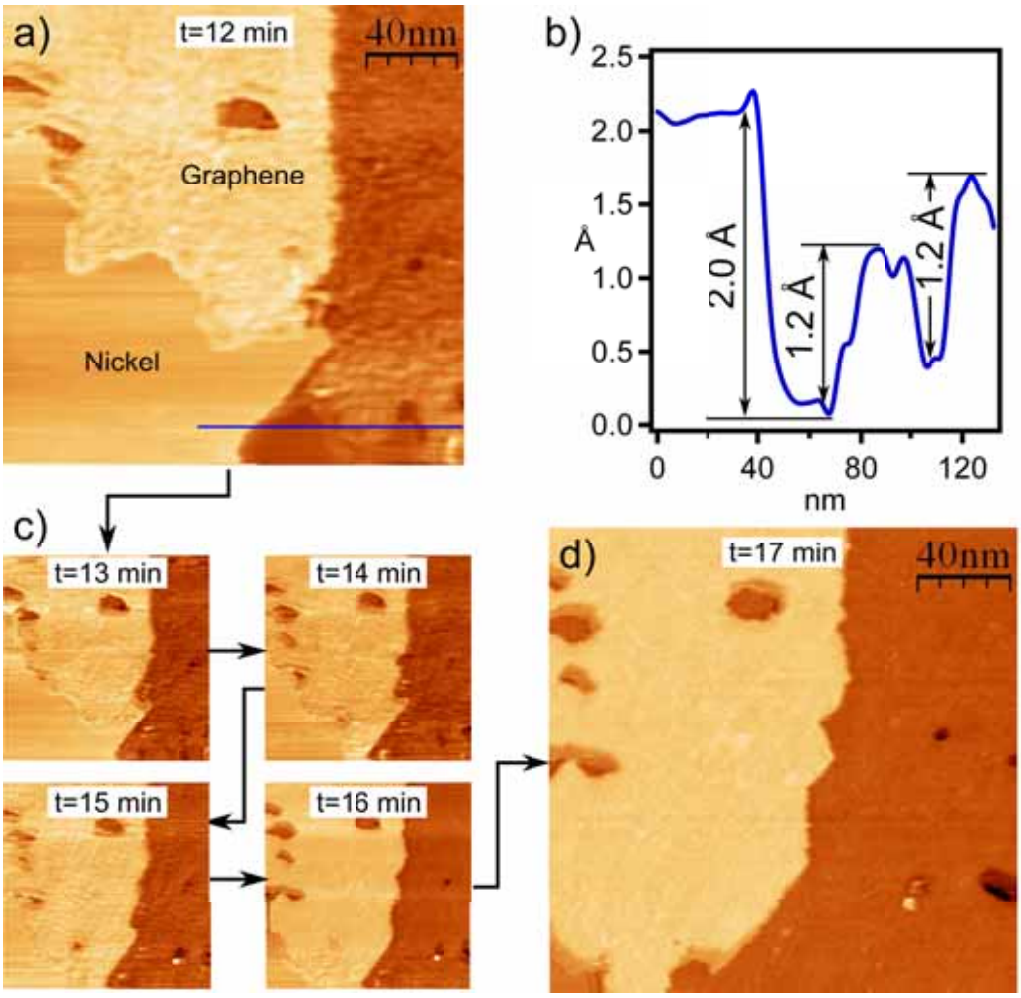

Figure 6.8: Graphene growth front. STM images obtained at 0.5 V with multiple tip. The STM images suffer from multiple tip effect, which does not hide the important physical information. a) STM image showing the graphene layer (top) and the Ni(111) surface (bottom), obtained at t=12 min. b) Height profile obtained along the blue line in image (a). c) Growth of the graphene layer thought the nickel surface obtained at t=13, 14 ,15 and 16 min respectively. d) STM image of a graphene covered nickel surface obtained at 18 min.

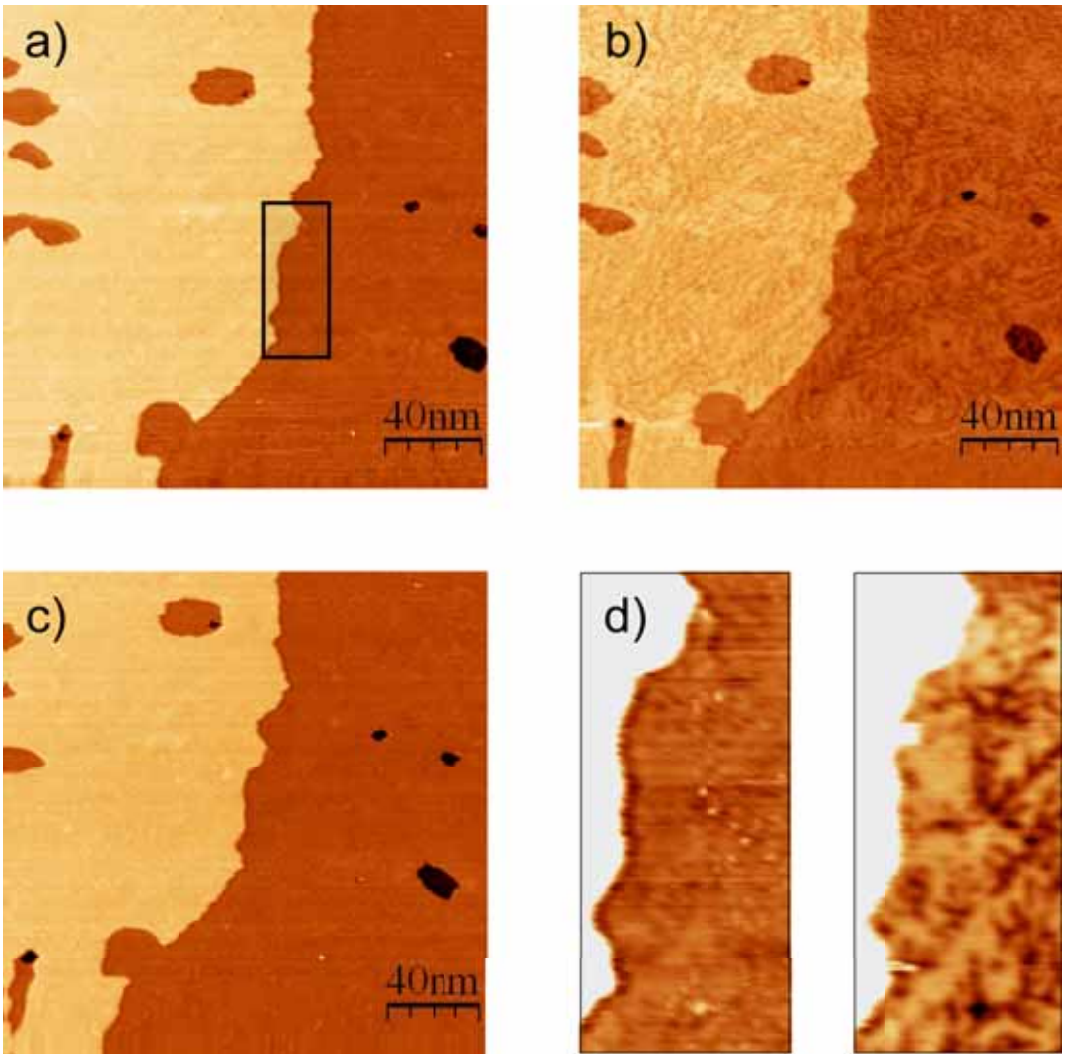

Figure 6.9: Bias contrast of graphene/Ni(111). STM image of a graphene monolayer on Ni(111) obtained with a bias voltage of a) 2V. b) 3 V. c) 4 V. d) Two zoom image of the area marked with a black box in (a) obtained with a bias voltage of 2V (left) and 3 V (right).

Figure 6.10. Note that the cooling process produce a huge thermal drift in the STM system and the STM images are obtained in a different region that Figure 6.8 and Figure 6.9.

The cold surface shows different areas when measured by means of STM, as shown in the central image in Figure 6.10, obtained at RT and using a bias voltage of 1 V. Several zooms have been performed in this image in order to study the topography of the surface in the areas marked with a black box. Figure 6.10.a shows two regions. The left one corresponds to a graphene layers while the right part corresponds to nickel, as demonstrated by its relative height of 0.7 Å. The same case is observed in Figure 6.10.c. Hence graphene is found as a result of the CVD process, although its density is quite low, indicating that the optimum temperature to produce a complete graphene monolayer is higher than 500 ºC, as also stated by Addou et. al.[97]. Figure 6.10.b shows us a zoom performed on the large island in the center of the image. Note that the surface of the island shows the stripped pattern characteristic of Ni_2C. The height profile shows a relative height of 1.8 Å, corresponding to the height of a Ni_2C island on nickel with respect to the underlying nickel terrace. Note that the island presents the same edge morphology as the Ni_2C islands observed in Figure 3.2.a, although its height is smaller due to the difference in the bias voltage of the STM image (see Figure 6.3). A Ni_2C layer intercalated in a nickel terrace is observed in Figure 6.10.d with a relative height of -0.2 Å with respect to the surrounding nickel.

In conclusion, graphene, Ni_2C and nickel coexist, which indicates that graphene formation is incomplete. Note that graphene grows by propagation of a graphene layer [97] which could result in areas of the sample with no graphene and other covered by graphene several microns away. Further investigation of the resultant reaction products is needed to extract a solid conclusion.

6.3 CVD reaction at 600 ºC

In previous section we have studied the formation and stability of the products of the CVD reaction of propene on Ni(111) at 500 ºC. We found that the stability of compounds such as Ni_2C is highly dependent on the sample temperature and propene pressure. Graphene formation is driven by the carbon concentration as well as the sample temperature. The dependence of the CVD reaction products on the temperature seems obvious. In this section a CVD reaction with T'_R=600 ºC is studied in-situ by means of high temperature STM.

6.3.1 Stability of Ni(111) at 600ºC

As in the case of STM imaging at 500 ºC, the Ni(111) surface appears usually stable at 600 ºC, although the step edges are mobile at this temperature. Figure 6.11

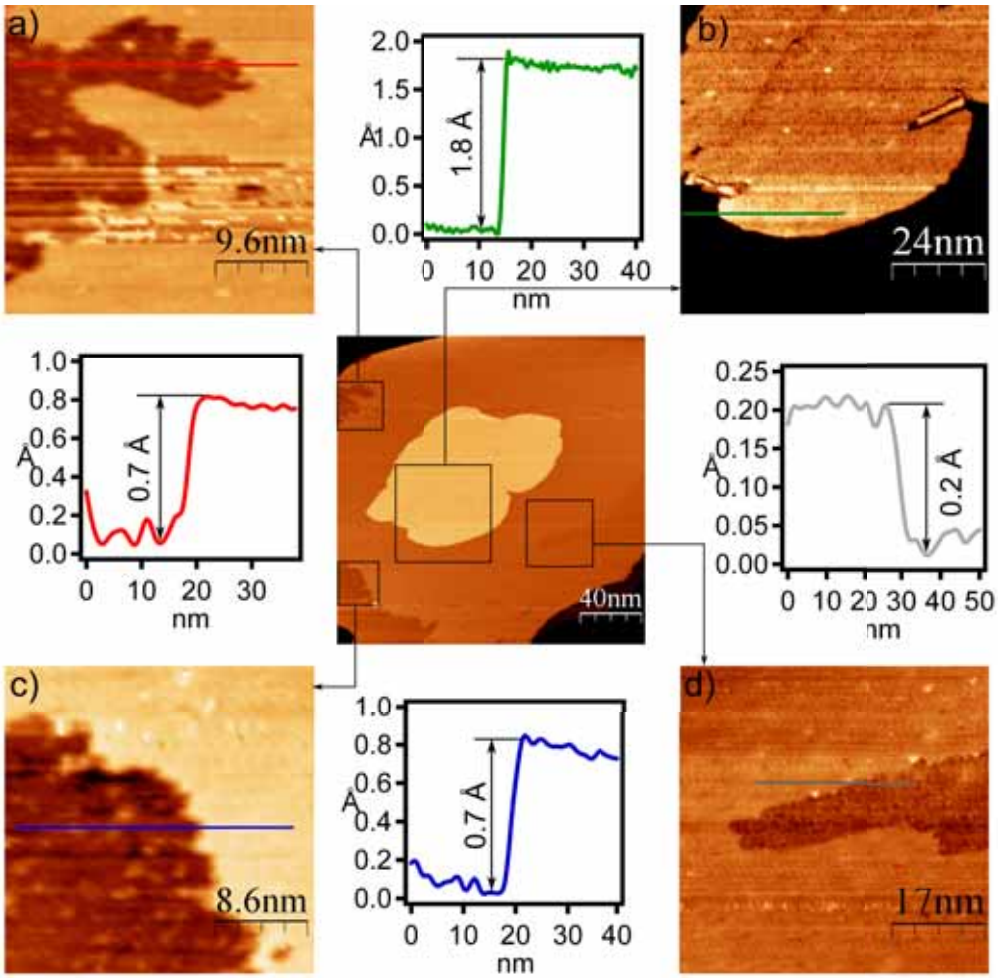

Figure 6.10: Coexisting C phases after cooling to RT. The central image is a STM image obtained after the CVD reaction at RT. Four enlarge regions are shown with their respective height profiles. The zooms show a a) a graphene-Nickel interface. b) Ni_2C on nickel. c) a graphene-Nickel interface. d) a nickel-Ni_2C interface.

shows two STM images obtained on a clean Ni(111) surface at 600 ºC. The images were both obtained at a bias voltage of 1 V. The second image was acquired 1 min 20 s after the first. The thermal drift is compensated by comparing the position of the adsorbates.

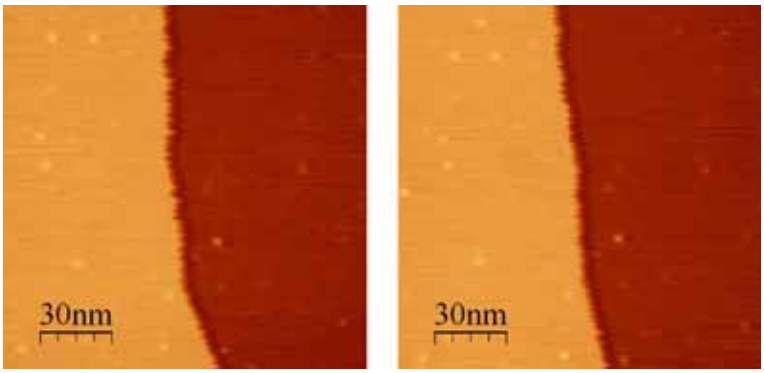

Figure 6.11: Consecutive STM images of Ni(111) at 600 ºC. The images were obtained with a time difference of 1 mi 20 s.

6.3.2 Ni_2C formation at 600 ºC

As demonstrated in section 3.2 Ni_2C becomes unstable at temperatures around 450-500 ºC in UHV conditions [39]. However, exposing the sample to a propene atmosphere can stabilize the surface compound at 500 ºC as seen in the previous section. In what follows, we present a study of the growth and stability of Ni_2C on Ni(111) at 600 ºC when exposed to a propene atmosphere.

All STM images shown in Figure 6.12 are obtained at 600 ºC using a bias voltage of 1 V. Figure 6.12.a shows a sequence pf STM images taken prior to propene dosing (a, downwards scanning), at the start of dosing propene at $1 \cdot 10^{-6}$ mbar (b, started at t=26 s, upwards scanning) and during the dosing (c, t=52s, downwards scanning). At the center of Figure 6.12.b (t=41 s) we observe an expansion of the terrace and a decrease of its apparent height from 2.1 Å to 1.7 Å with respect to the underlying nickel terrace. This change is attributed to the formation of a Ni_2C layer, identically to the phenomena observed at 500 ºC. Figure 6.12.c shows an STM image obtained just after Figure 6.12.b. We can observe than the terrace expansion continues, as demonstrated by the change in the apparent terrace step orientation.

Once all the surface is covered by Ni_2C, no changes were observed on the surface. The sample remains under a propene atmosphere at 600ºC for 5 minutes. O No graphene formation was observed.

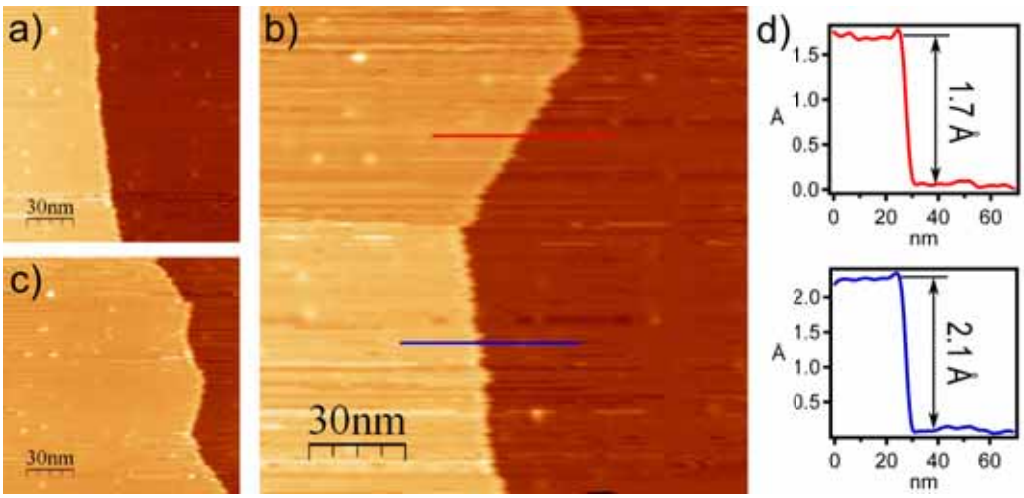

Figure 6.12: Formation of Ni_2C at 600 ºC. a) STM image of Ni(111) in UHV conditions. b) STM image of the surface started at t=26.3 s and obtained with a bias voltage of 1 V. The scanning direction is upwards. At the center of the image the growth of a Ni_2C layer starts. c) STM image of the surface obtained just after (b). The scanning direction is downwards, indicating a terrace expansion. d) Height profiles along the lines in (b).

6.4 CVD reaction at T'_R=730 ºC

The stability of Ni_2C at 600 ºC with a propene atmosphere of $1 \cdot 10^{-6}$ mbar was an unexpected observation. In order to check the dependence on T'_R of the resultant products of the CVD reaction a preparation using T'_R =730 ºC was realized. In this section we expose the obtained results.

6.4.1 Nickel surface and CVD reaction at 730 ºC

Figure 6.13 shows four STM images that illustrate the CVD reaction of propene on Ni(111) at 730 ºC. Also at 730 ºC, the nickel surface does not show a significant evolution with time (not shown), apart of the step mobility. At t=0 s we open the leak valve and fill the chamber with propene at a pressure of $1 \cdot 10^{-6}$ mbar. Figure 6.13.a shows an STM image started at t=7 min (D=420 L). No traces of Ni_2C such as the stripped pattern or the characteristic height decrease of the terrace were observed. The characteristic step expansion of the Ni_2C growth was neither observed. The ratio between absorption and desorption of propene molecules is reduced and the carbon dilution to bulk is increased when increasing the temperature. Those conditions make Ni_2C unstable on Ni(111) at those propene pressure and temperature conditions. The reduction of Ni_2C formation when increasing the temperature was also reported by Addou et. al. [97].

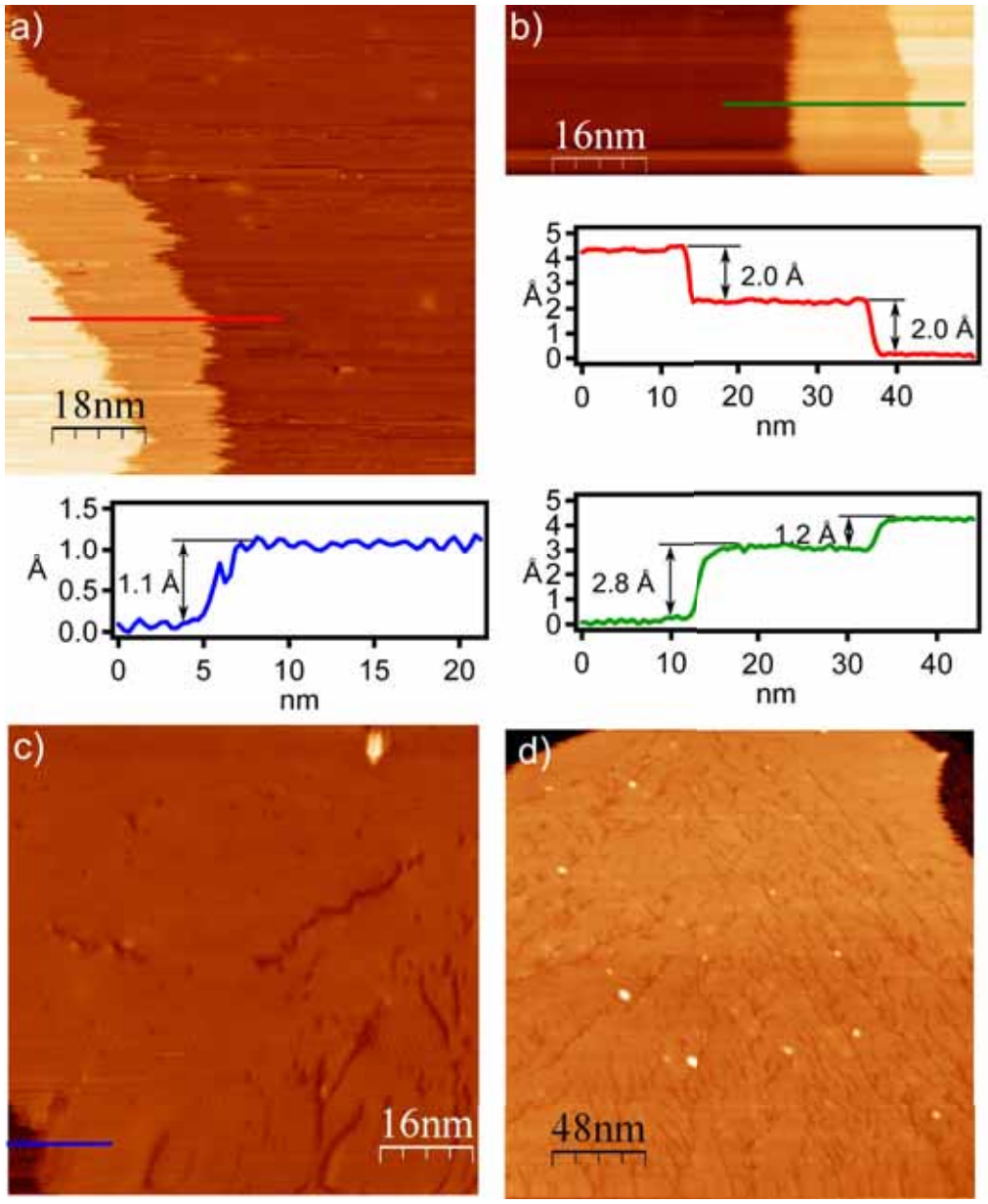

Figure 6.13: Graphene growth at 730 ºC. All STM images were obtained with a bias voltage of 1.5 V. a) STM image of a Ni(111) unreacted surface exposed to a propene atmosphere of $1 \cdot 10^{-6}$ mbar at 730 ºC obtained at t= 7 min. b) STM image of graphene layers (left and right) covering a nickel terrace (center) obtained at t=12 min with a bias voltage of . c,d) Graphene monolayer on Ni(111) obtained at t=14 min and t=35 min respectively. Height profiles are obtained along the lines in the STM images.

Figure 6.13.b was started at t=12 min 11 s with a bias voltage of 1.5 V; it shows two step terraces. As observed in the height profile obtained along the green line, the two terrace steps have a height difference of 2.8 Å and 1.2 Å respectively. The height increase of 2.8 Å corresponds to a height difference from a graphene layer (dark region) to a double nickel step ($2.0 \times 2 - 1.2 = 2.8$). The height difference of 1.2 Å is the characteristic height of a graphene monolayer on top of Ni(111), hence we can identify the right part of the STM image as a graphene monolayer. Figure 6.13.c shows an STM image started at t=13 min 51 s with a bias voltage of 1.5 V of a graphene monolayer that grows on a nickel terrace. The growth of the graphene monolayer occurs as described in subsubsection 6.2.4.1. The underlying nickel terrace can be observed in the lower-left part of the STM image. The height profile along the blue line shows a height difference of 1.1 Å, as expected for graphene monolayer. Some structural defects are observed in the STM image, and are distributed homogeneously in the surface as observed in Figure 6.13.d. These defects have a similar structure of the defects showed on graphene in Figure 6.9. Note that no significant defects have been observed in nickel nor Ni_2C surfaces. As in the cases of CVD reaction at lower temperature, once the graphene covers the nickel surface, it remains stable for periods of time of several minutes. After 30 minutes, and once the graphene formations has concluded, the leak valve was closed and the chamber recovers its base pressure. At the same time the sample heating was turned off and the sample recovers the RT.

6.4.2 Sample surface after cooling at RT

Once the sample temperature stabilized, we measured it by means of STM. Figure 6.14 shows STM images of the sample at RT obtained with a bias voltage of 1 V. In Figure 6.14.a we observe that the surface presents straight lines with and inclination of 60^{o} forming a superstructure. As observed in Figure 6.14.b, the superstructure has a height of 0.6 Å. The STM image observed in Figure 6.14.c shows a STM image of a wider area. As observed, the superstructure is spread all around the crystal surface. This structure was previously reported by Jacobson [89] and attributed to rotated graphene on Ni(111). The moire periodicity reported in [89] was not observed due to low image resolution, hence the graphene rotation respect to the substrate can not be determined.

6.5 Summary

In this chapter we present a first approach to the study of CVD reaction of propene on Ni(111) surface by means of high temperature STM. Due to the complexity of the reaction, further investigations are necessary to achieve solid conclusions.

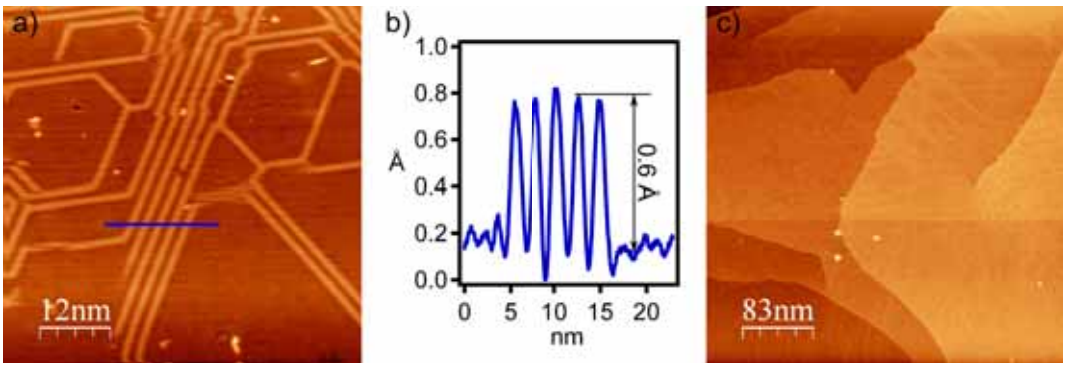

Figure 6.14: Rotated graphene domains after cooling to RT. a) STM image of the surface after the CVD reaction and cooling to RT. The straight lines form an angle of 60º. b) Height profile along the blue line in image (a). c) Wide area scanning of the pattern observed in (a), the STM image shows an homogeneous distribution of the pattern.

In the initial stages of the CVD reaction, the exposure of a Ni(111) surface to a propene atmosphere results in the growth of a Ni_2C layer. Ni_2C is stable in a dynamical situation that depends on the carbon concentration on the surface. The carbon concentration is determined by the absorbed propene molecules minus the desorbed propene molecules and minus the carbon diffusion into the bulk. All three contributions strongly depend on temperature and propene pressure. The formation of Ni_2C is observed at 500ºC at propene pressures above $2 \cdot 10^{-7}$ mbar and at 600 ºC at a propene pressure of $1 \cdot 10^{-6}$ mbar and not observed at 730 ºC at a propene pressure of $1 \cdot 10^{-6}$ mbar. The formation of Ni_2C is characterized by step expansion due to the lower nickel density of the Ni_2C with respect to Ni(111). Heating the sample after stopping the propene dosing results in the dissolution of Ni_2C into the bulk in a time scale of a few minutes. The growth and stability of Ni_2C is then governed by the carbon concentration at the surface and the temperature.

Graphene growth occurs in a second stage. The growth of graphene takes place by propagation of the graphene layer, in contrast to the growth of Ni_2C, which takes place in different places simultaneously. In contrast with Ni_2C, graphene does not need a propene atmosphere to growth but a certain carbon concentration in the bulk.

7 Conclusions

Graphene has arisen as a promising material for future applications due to its extraordinary properties. Special attention deserve the properties arising from its edges, that has recently been studied in graphene nanoribbons. There is a growing interest in producing and controlling its properties The epitaxial growth of graphene on metal substrates is a promising route to obtain high quality graphene sheets industrially. Ni(111) is an ideal substrate since its low lattice mismatch with graphene allows the production of graphene layers with 1x1 stacking. On Ni(111), graphene is produced by a CVD reaction, using as a precursor carbon containing gases such as propene, ethylene, CO, etc. In this thesis we presented a study of the growth mechanism of graphene layers and nanoislands on Ni(111).

A new mechanism to grow graphene nanoislands on Ni(111) by dosing propene at RT and heating the sample to a controlled temperature is presented in chapter 3. We observe that the reaction has a narrow temperature range were graphene nanoislands are formed. Heating the sample below 400 ºC produce Ni_2C and heating the sample above 500 ºC propene desorption. The crystal exposure to propene is also controlled. Our finding indicate that there is a minimum dose of 1 L by then graphene nucleation does not occur. A saturation value of 5 L is also observed, where the graphene formation does not increase. The annealing time is also an important factor. Too short reaction times can result in the incomplete diffusion of the Ni_2C domains formed during the heating ramp, and too long reaction times can result in uncontrolled growth of islands due to carbon precipitation from the bulk. The irregular graphene nanoislands obtained in this reaction can be shape modeled by applying an annealing treatment. Annealing at 500 ºC during 20 min results in a triangular shape of the islands while annealing at 650 ºC during 10 minutes results in an hexagonal shape.

The structure of the islands is studied experimentally and theoretically in chapter 4. The island interact weekly with the substrate, as demonstrated by the occasional observation of rotational Moiré patterns in some islands. The majority of the islands have a 1x1 stacking. Triangular and hexagonal islands have straight edges with the crystallographic orientation of zigzag edges. However the stacking with the substrate divide the edges in two types, zz_h and zz_t, which have the outer atom on a hollow or top position respectively. All triangular islands observed have zz_h edges, which turn out to be more energetically favorable than zz_t. Zigzag edges are not reported in free-standing graphene, however on Ni(111) the substrate interaction makes zz_h stable. Top-fcc stacking is the prevalent stacking in the graphene nanoislands, since

it is more energetically favorable than top-hcp stacking. However, the interaction of the edges with the substrate is stronger than the interaction of the layer and some islands with zz_h and top-fcc are observed occasionally. Hexagonal graphene nanoislands have the two type of edges. Zz_h edges with good crystalline quality were observed, however zz_t edges are unstable and a pentagon-heptagon reconstruction was observed, named $zz_t(57)$.

Graphene edges have also an important role in the growth of islands. In-situ high temperature STM measurements presented in chapter 5 show three growth modes depending on the temperature. At 450 ºC islands have a rough edges, what produces an isotropic growth of the islands. Increasing the temperature at 500 ºC allows the formation of zigzag edges. At this temperature islands adopt a triangular shape due to the different growth velocity of zz_h and zz_t. The zz_t grow faster and tend to disappear, while zz_h edges has a small growth velocity and remain. The growth velocity of the edges is driven by a potential barrier in the incorporation of carbon to the edge, and it can be modified by adjusting the temperature. At 650 ºC both edge types have the same growth velocity and islands adopt an hexagonal shape.

Lastly, we studied the growth of a monolayer graphene on Ni(111) by in-situ high temperature STM in chapter 6. We found that the formation of Ni_2C occurs homogeneously in all the surface at higher temperature than expected, since the propene atmosphere stabilize it up to 600 ºC, while in UHV it is unstable above 400 ºC. Once the crystal has enough carbon diluted, the graphene growth starts. Graphene grows by front propagation, and can cover a wide surface of the crystal, while another region separated several microns is still uncovered. Graphene growth was observed in a wide range of temperatures, from 500 to 730 ºC.

Acknowledgments

I would like to show my gratitude to Pietro Gambardella, who give me the opportunity to work at the ICN. His always true comments and insights have teach me a lot. He has the gift of make me think with a short sentence and I appreciate that. I would also thank to Gustavo Ceballos for introducing me to the nano world. He has been a pleasant guide for the long journey that has been these thesis, with notes of humor, sense, and reflection. I have tried hard and I almost made him mad, but I didn't succeed.

I also would like to thank to David Serrate for giving me the opportunity to perform experiment in the extraordinary facilities of the INA, which represent an important part of this thesis. He made my stance in Zaragoza really pleasant. I am very grateful to Carlos Martín for helping me with those experiments and sharing moments of laugh in the lab. I was fortunate to collaborate with Aran Garcia and Daniel Sanchez from DIPC, two very professional theoreticians who did the DFT calculations shown in this thesis. Their rapidness and the quality of their work surprised me.

I share those years with excellent workmates, people who has taught me a lot and to whom I am very grateful. I would like to thank to Aitor Mugarza for sharing scientific knowledge and squash court; Cornelius Krull for innumerable moments in the lab and outside it; Alberto Lodi for lots of recipies and the invention of Frosties Cookies®; Jerald Kavich for showing me how to defend your ideas, even when everybody disagrees; Kevin Garello for lots of funny moment, and also the language exchange; Can Our Avci for being such a nice and easygoing person; Sylvie Godey for not killing me when I start saying stupid things; Corneliu Nistor for those timid and brilliant comments; Marc Maymó for make me feel like home (although I am already there); Raoul Piquerel for his always positive attitude; Mihail Miron for saying the thinks as they are; and Jorge Lobo for those passionate squash games and one or two scars. Also I would like to thank Santos Alvarado, Gina Peschel and Sonia Matencio for sharing their time and laughs with me.

Special mention deserve my parents, who support me in any action I toke, even when it is wrong, and help me stand up after every defeat; Neus, who has been cleaning the way since I was born; and Emma, who is Emma.

Bibliography

[1] P. R. Wallace, "The band theory of graphite," *Phys. Rev.*, vol. 71, p. 622, 1947.

[2] R. E. Peierls, "Bemerkungen über umwandlungstemperaturen," *Helv. Phys. Acta*, vol. 7, p. 81, 1934.

[3] ——, "Quelques proprietes typiques des corpses solides," *Ann. Inst. Henri Poincare*, vol. 5, p. 177, 1935.

[4] L. D. Landau, "Zur theorie der phasenumwandlungen ii." *Phys. Z. Sowjetunion*, vol. 11, p. 26, 1937.

[5] K. S. Novoselov, A. K. Geim, S. V. Morozov, D. Jiang, Y. Zhang, S. V. Dubonos, I. V. Grigorieva, and A. A. Firsov, "Electric field effect in atomically thin carbon films," *Science*, vol. 306, p. 666, 2004.

[6] J. C. Meyer, A. K. Geim, M. I. Katsnelson, K. S. Novoselov, T. J. Booth, and S. Roth, "The structure of suspended graphene sheets," *Nature*, vol. 446, p. 60, 2007.

[7] [Online]. Available: http://wps.prenhall.com/wps/media/objects/724/741576/index.html

[8] [Online]. Available: http://openclipart.org/detail/29143/graphene-by-j_alves

[9] P. Recher and B. Trauzettel, "A defect controls transport in graphene," *Physics*, vol. 4, p. 25, 2011.

[10] M. Mecklenburg and B. C. Regan, "Spin and the honeycomb lattice: Lessons from graphene," *Phys. Rev. Lett.*, vol. 106, p. 116803, 2011.

[11] E. Fradkin, "Critical behavior of disordered degenerate semiconductors. ii. spectrum and transport properties in mean-field theory," *Phys. Rev. B*, vol. 33, p. 3263, 1986.

[12] E. Abrahams, P. W. Anderson, D. C. Licciardello, and T. V. Ramakrishnan, "Scaling theory of localization: Absence of quantum diffusion in two dimensions," *Phys. Rev. Lett.*, vol. 42, p. 673, 1979.

[13] P. A. Lee, "Localized states in a d-wave superconductor," *Phys. Rev. Lett.*, vol. 71, p. 1887, 1993.

[14] K. Ziegler, "Delocalization of 2d dirac fermions: The role of a broken supersymmetry," *Phys. Rev. Lett.*, vol. 80, p. 3113, 1998.

[15] K. S. Novoselov, A. K. Geim, S. V. Morozov, D. Jiang, M. I. Katsnelson, I. V. Grigorieva, S. V. Dubonos, and A. A. Firsov, "Two-dimensional gas of massless dirac fermions in graphene," *Nature*, vol. 438, p. 197, 2005.

[16] C. Toke, P. E. Lammert, V. H. Crespi, and J. K. Jain, "Fractional quantum hall effect in graphene," *Phys. Rev. B*, vol. 74, p. 235417, 2006.

[17] K. S. Novoselov, Z. Jiang, Y. Zhang, S. V. Morozov, H. L. Stormer, U. Zeitler, J. C. Maan, G. S. Boebinger, P. Kim, and A. K. Geim, "Room-temperature quantum hall effect in graphene," *Science*, vol. 315, p. 1379, 2007.

[18] X. Du, I. Skachko, A. Barker, and E. Y. Andrei, "Approaching ballistic transport in suspended graphene," *Nat. Nano.*, vol. 3, p. 491, 2008.

[19] N. Tombros, C. Jozsa, M. Popinciuc, H. T. Jonkman, and B. J. van Wees, "Electronic spin transport and spin precession in single graphene layers at room temperature," *Nature*, vol. 448, p. 571, 2007.

[20] S. Cho, Y.-F. Chen, and M. S. Fuhrer, "Gate-tunable graphene spin valve," *App. Phys. Lett.*, vol. 91, p. 123105, 2007.

[21] C. Lee, X. Wei, J. W. Kysar, and J. Hone, "Measurement of the elastic properties and intrinsic strength of monolayer graphene," *Science*, vol. 321, p. 385, 2008.

[22] A. B. Kuzmenko, E. van Heumen, F. Carbone, and D. van der Marel, "Universal optical conductance of graphite," *Phys. Rev. Lett.*, vol. 100, p. 117401, 2008.

[23] [Online]. Available: http://www.scientificamerican.com/slideshow.cfm?id=diy-graphene-how-to-make-carbon-layers-with-sticky-tape

[24] M. Choucair, P. Thordarson, and J. A. Stride, "Gram-scale production of graphene based on solvothermal synthesis and sonication," *Nat. Nano.*, vol. 4, p. 30, 2009.

[25] S. Stankovich, D. A. Dikin, R. D. Piner, K. A. Kohlhaas, A. Kleinhammes, Y. Jia, Y. Wu, S. T. Nguyen, and R. S. Ruoff, "Synthesis of graphene-based nanosheets via chemical reduction of exfoliated graphite oxide," *Carbon*, vol. 45, p. 1558, 2007.

[26] P. Sutter, "Epitaxial graphene: How silicon leaves the scene," *Nat. Mater.*, vol. 8, p. 171, 2009.

[27] J. Jobst, D. Waldmann, F. Speck, R. Hirner, D. K. Maude, T. Seyller, and H. B. Weber, "Transport properties of high-quality epitaxial graphene on 6h-sic(0001)," *Sol. Stat. Comm.*, vol. 151, p. 1061, 2011.

[28] S. Hagstrom, H. B. Lyon, and G. A. Somorjai, "Surface structures on the clean platinum (100) surface," *Phys. Rev. Lett.*, vol. 15, pp. 491–493, 1965.

[29] H. B. Lyon and G. A. Somorjai, "Low-energy electron-diffraction study of the clean (100), (111), and (110) faces of platinum," *J. Chem. Phys.*, vol. 46, p. 2539, 1967.

[30] A. Morgan and G. Somorjai, "Low energy electron diffraction studies of gas adsorption on the platinum (100) single crystal surface," *Surface Science*, vol. 12, pp. 405 – 425, 1968.

[31] J. W. May, "Platinum surface leed rings," *Surface Science*, vol. 17, pp. 267 – 270, 1969.

[32] J. Grant and T. Haas, "A study of ru(0001) and rh(111) surfaces using leed and auger electron spectroscopy," *Surface Science*, vol. 21, pp. 76 – 85, 1970.

[33] S. Helveg, C. Lopez-Cartes, J. Sehested, P. L. Hansen, B. S. Clausen, J. R. Rostrup-Nielsen, F. Abild-Pedersen, and J. K. Norskov, "Atomic-scale imaging of carbon nanofibre growth," *Nature*, vol. 427, pp. 426–429, 2004.

[34] P. W. Sutter, J.-I. Flege, and E. A. Sutter, "Epitaxial graphene on ruthenium," *Nat. Mater.*, vol. 7, p. 406, 2008.

[35] A. Grüneis and D. V. Vyalikh, "Tunable hybridization between electronic states of graphene and a metal surface," *Phys. Rev. B*, vol. 77, p. 193401, 2008.

[36] Y. Pan, H. Zhang, D. Shi, J. Sun, S. Du, F. Liu, and H.-j. Gao, "Highly ordered, millimeter-scale, continuous, single-crystalline graphene monolayer formed on ru (0001)," *Adv. Mat.*, vol. 21, p. 2777, 2009.

[37] L. Gao, J. R. Guest, and N. P. Guisinger, "Epitaxial graphene on cu(111)," *Nano Lett.*, vol. 10, p. 3512, 2010.

[38] S. Günther, S. Dänhardt, B. Wang, M. L. Bocquet, S. Schmitt, and J. Wintterlin, "Single terrace growth of graphene on a metal surface," *Nano Lett.*, vol. 11, p. 1895, 2011.

[39] J. Lahiri, T. Miller, L. Adamska, I. I. Oleynik, and M. Batzill, "Graphene growth on ni(111) by transformation of a surface carbide," *Nano Lett.*, vol. 11, p. 518, 2011.

[40] A. K. Geim, "Graphene: Status and prospects," *Science*, vol. 324, p. 1530, 2009.

[41] G. Odahara, S. Otani, C. Oshima, M. Suzuki, T. Yasue, and T. Koshikawa, "In-situ observation of graphene growth on ni(111)," *Surf. Sci.*, vol. 605, p. 1095, 2011.

[42] X. Li, W. Cai, L. Colombo, and R. S. Ruoff, "Evolution of graphene growth on ni and cu by carbon isotope labeling," *Nano Lett.*, vol. 9, p. 4268, 2009.

[43] I. Pletikosić, M. Kralj, P. Pervan, R. Brako, J. Coraux, A. T. N'Diaye, C. Busse, and T. Michely, "Dirac cones and minigaps for graphene on ir(111)," *Phys. Rev. Lett.*, vol. 102, p. 056808, 2009.

[44] K. S. Kim, Y. Zhao, H. Jang, S. Y. Lee, J. M. Kim, K. S. Kim, J.-H. Ahn, P. Kim, J.-Y. Choi, and B. H. Hong, "Large-scale pattern growth of graphene films for stretchable transparent electrodes," *Nature*, vol. 457, p. 706, 2009.

[45] L. A. Ponomarenko, F. Schedin, M. I. Katsnelson, R. Yang, E. W. Hill, K. S. Novoselov, and A. K. Geim, "Chaotic dirac billiard in graphene quantum dots," *Science*, vol. 320, p. 356, 2008.

[46] K. A. Ritter and J. W. Lyding, "The influence of edge structure on the electronic properties of graphene quantum dots and nanoribbons," *Nat. Mater.*, vol. 8, p. 235, 2009.

[47] S. K. Hämäläinen, Z. Sun, M. P. Boneschanscher, A. Uppstu, M. Ijäs, A. Harju, D. Vanmaekelbergh, and P. Liljeroth, "Quantum-confined electronic states in atomically well-defined graphene nanostructures," *Phys. Rev. Lett.*, vol. 107, p. 236803, 2011.

[48] D. Eom, D. Prezzi, K. T. Rim, H. Zhou, M. Lefenfeld, S. Xiao, C. Nuckolls, M. S. Hybertsen, T. F. Heinz, and G. W. Flynn, "Structure and electronic properties of graphene nanoislands on co(0001)," *Nano Lett.*, vol. 9, p. 2844, 2009.

[49] S.-h. Phark, J. Borme, A. L. Vanegas, M. Corbetta, D. Sander, and J. Kirschner, "Direct observation of electron confinement in epitaxial graphene nanoislands," *ACS Nano*, vol. 5, p. 8162, 2011.

[50] J. Fernández-Rossier and J. Palacios, "Magnetism in graphene nanoislands," *Phys. Rev. Lett.*, vol. 99, p. 177204, 2007.

[51] O. V. Yazyev and M. I. Katsnelson, "Magnetic correlations at graphene edges: Basis for novel spintronics devices," *Phys. Rev. Lett.*, vol. 100, p. 047209, 2008.

[52] H.-X. Yang, M. Chshiev, D. W. Boukhvalov, X. Waintal, and S. Roche, "Inducing and optimizing magnetism in graphene nanomeshes," *Phys. Rev. B*, vol. 84, p. 214404, 2011.

[53] H. Duan, J. Zhao, Y. Zhang, E. Xie, and L. Han, "Preparing patterned carbonaceous nanostructures directly by overexposure of pmma using electron-beam lithography," *Nanotechnology*, vol. 20, p. 135306, 2009.

[54] X. Liang, Y.-S. Jung, S. Wu, A. Ismach, D. L. Olynick, S. Cabrini, and J. Bokor, "Formation of bandgap and subbands in graphene nanomeshes with sub-10 nm ribbon width fabricated via nanoimprint lithography," *Nano Lett.*, vol. 10, p. 2454, 2010.

[55] R. K. Puddy, P. H. Scard, D. Tyndall, M. R. Connolly, C. G. Smith, G. A. C. Jones, A. Lombardo, A. C. Ferrari, and M. R. Buitelaar, "Atomic force microscope nanolithography of graphene: Cuts, pseudocuts, and tip current measurements," *App. Phys. Lett.*, vol. 98, p. 133120, 2011.

[56] S. Masubuchi, M. Ono, K. Yoshida, K. Hirakawa, and T. Machida, "Fabrication of graphene nanoribbon by local anodic oxidation lithography using atomic force microscope," *App. Phys. Lett.*, vol. 94, p. 082107, 2009.

[57] A. T. N'Diaye, J. Coraux, T. N. Plasa, C. Busse, and T. Michely, "Structure of epitaxial graphene on ir(111)," *New J. Phys.*, vol. 10, p. 043033, 2008.

[58] K. Donner and P. Jakob, "Structural properties and site specific interactions of pt with the graphene/ru(0001) moiré overlayer," *J. of Chem. Phys.*, vol. 131, p. 164701, 2009.

[59] J. M. Wofford, S. Nie, K. F. McCarty, N. C. Bartelt, and O. D. Dubon, "Graphene islands on cu foils: The interplay between shape, orientation, and defects," *Nano Lett.*, vol. 10, p. 4890, 2010.

[60] J. Cai, P. Ruffieux, R. Jaafar, M. Bieri, T. Braun, S. Blankenburg, M. Muoth, A. P. Seitsonen, M. Saleh, X. Feng, K. Mullen, and R. Fasel, "Atomically precise bottom-up fabrication of graphene nanoribbons," *Nature*, vol. 466, p. 470, 2010.

[61] B. Wang, X. Ma, M. Caffio, R. Schaub, and W.-X. Li, "Size-selective carbon nanoclusters as precursors to the growth of epitaxial graphene," *Nano Lett.*, vol. 11, p. 424, 2011.

[62] J. Lu, P. S. E. Yeo, C. K. Gan, P. Wu, and K. P. Loh, "Transforming c60 molecules into graphene quantum dots," *Nat. Nano.*, vol. 6, p. 247, 2011.

[63] Y. Cui, Q. Fu, H. Zhang, and X. Bao, "Formation of identical-size graphene nanoclusters on ru(0001)," *Chem. Comm.*, vol. 47, p. 1470, 2011.

[64] C. Johann, T. N. Alpha, E. Martin, B. Carsten, W. Dirk, B. Niemma, J. M. z. H. Frank, G. Raoul van, P. Bene, and M. Thomas, "Growth of graphene on ir(111)," *New J. Phys.*, vol. 11, p. 023006, 2009.

[65] A. Dinger, C. Lutterloh, J. Biener, and J. Kuppers, "Hydrogen atom reactions with graphite island edges on pt(111) surfaces: hydrogenation through eley-rideal and hot-atom processes," *Surf. Sci.*, vol. 421, p. 17, 1999.

[66] M. Olle, G. Ceballos, D. Serrate, and P. Gambardella, "Yield and shape selection of graphene nanoislands grown on ni(111)," *Nano Lett.*, vol. 12, p. 4431, 2012.

[67] M. Razavy, *Quantum theory of tunneling.* World scientify publishing Co., 2003.

[68] C. J. Chen, *Introduction to Scanning Tunneling Microscopy.* Oxford University Press, 1993.

[69] J. Bardeen, "Tunnelling from a many-particle point of view," *Phys. Rev. Lett.*, vol. 6, p. 57, 1961.

[70] J. Tersoff and D. R. Hamann, "Theory of the scanning tunneling microscope," *Phys. Rev. B*, vol. 31, p. 805, 1985.

[71] N. D. Lang, "Spectroscopy of single atoms in the scanning tunneling microscope," *Phys. Rev. B*, vol. 34, p. 5947, 1986.

[72] A. Selloni, P. Carnevali, E. Tosatti, and C. D. Chen, "Voltage-dependent scanning-tunneling microscopy of a crystal surface: Graphite," *Phys. Rev. B*, vol. 31, p. 2602, 1985.

[73] V. A. Ukraintsev, "Data evaluation technique for electron-tunneling spectroscopy," *Phys. Rev. B*, vol. 53, p. 11176, 1996.

[74] L. V. Dzemiantsova, M. Karolak, F. Lofink, A. Kubetzka, B. Sachs, K. von Bergmann, S. Hankemeier, T. O. Wehling, R. Frömter, H. P. Oepen, A. I. Lichtenstein, and R. Wiesendanger, "Multiscale magnetic study of ni(111) and graphene on ni(111)," *Phys. Rev. B*, vol. 84, p. 205431, 2011.

[75] W. Zhao, S. M. Kozlov, O. Höfert, K. Gotterbarm, M. P. A. Lorenz, F. Viñes, C. Papp, A. Görling, and H.-P. Steinrück, "Graphene on ni(111): Coexistence of different surface structures," *J. Phys. Chem. Lett.*, vol. 2, p. 759, 2011.

[76] R. Rosei, M. De Crescenzi, F. Sette, C. Quaresima, A. Savoia, and P. Perfetti, "Structure of graphitic carbon on ni(111): A surface extended-energy-loss fine-structure study," *Phys. Rev. B*, vol. 28, p. 1161, 1983.

[77] J. Lahiri, Y. Lin, P. Bozkurt, I. I. Oleynik, and M. Batzill, "An extended defect in graphene as a metallic wire," *Nat. Nano.*, vol. 5, p. 326, 2010.

[78] A. M. Shikin, G. V. Prudnikova, V. K. Adamchuk, F. Moresco, and K. H. Rieder, "Surface intercalation of gold underneath a graphite monolayer on ni(111) studied by angle-resolved photoemission and high-resolution electron-energy-loss spectroscopy," *Phys. Rev. B*, vol. 62, p. 13202, 2000.

[79] I. Horcas, R. Fernandez, J. M. Gomez-Rodriguez, J. Colchero, J. Gomez-Herrero, and A. M. Baro, "Wsxm: A software for scanning probe microscopy and a tool for nanotechnology," *Rev. Sci. Instrum.*, vol. 78, p. 013705, 2007.

[80] C. Klink, I. Stensgaard, F. Besenbacher, and E. Lægsgaard, "An stm study of carbon-induced structures on ni(111): evidence for a carbidic-phase clock reconstruction," *Surf. Sci.*, vol. 342, p. 250, 1995.

[81] A. Grüneis, K. Kummer, and D. V. Vyalikh, "Dynamics of graphene growth on a metal surface: a time-dependent photoemission study," *New J. Phys.*, vol. 11, p. 073050, 2009.

[82] J. Nakamura, H. Hirano, M. Xie, I. Matsuo, T. Yamada, and K.-i. Tanaka, "Formation of a hybrid surface of carbide and graphite layers on ni(100) but no hybrid surface on ni(111)," *Surf. Sci.*, vol. 222, p. L809, 1989.

[83] A. Zangwill and D. D. Vvedensky, "Novel growth mechanism of epitaxial graphene on metals," *Nano Lett.*, vol. 11, p. 2092, 2011.

[84] L. Meng, Q. Sun, J. Wang, and F. Ding, "Molecular dynamics simulation of chemical vapor deposition graphene growth on ni (111) surface," *J. Phys. Chem. C*, vol. 116, p. 6097, 2012.

[85] Y. Gamo, A. Nagashima, M. Wakabayashi, M. Terai, and C. Oshima, "Atomic structure of monolayer graphite formed on ni(111)," *Surf. Sci.*, vol. 374, p. 61, 1997.

[86] S. M. Kozlov, F. Viñes, and A. Görling, "Bonding mechanisms of graphene on metal surfaces," *J. Phys. Chem. C*, vol. 116, p. 7360, 2012.

[87] X. Jia, M. Hofmann, V. Meunier, B. G. Sumpter, J. Campos-Delgado, J. M. Romo-Herrera, H. Son, Y.-P. Hsieh, A. Reina, J. Kong, M. Terrones, and M. S. Dresselhaus, "Controlled formation of sharp zigzag and armchair edges in graphitic nanoribbons," *Science*, vol. 323, p. 1701, 2009.

[88] P. Koskinen, S. Malola, and H. Häkkinen, "Self-passivating edge reconstructions of graphene," *Phys. Rev. Lett.*, vol. 101, p. 115502, 2008.

[89] P. Jacobson, B. Stöger, A. Garhofer, G. S. Parkinson, M. Schmid, R. Caudillo, F. Mittendorfer, J. Redinger, and U. Diebold, "Nickel carbide as a source of grain rotation in epitaxial graphene," *ACS Nano*, vol. 6, p. 3564, 2012.

[90] X. Zhang, Z. Xu, L. Hui, J. Xin, and F. Ding, "How the orientation of graphene is determined during chemical vapor deposition growth," *J. Phys. Chem. Lett.*, vol. 3, p. 2822, 2012.

[91] J. M. Soler, E. Artacho, J. D. Gale, A. Garcia, J. Junquera, P. Ordejon, and D. Sanchez-Portal, "The siesta method for ab initio order- n materials simulation," *Journal of Physics: Condensed Matter*, vol. 14, p. 2745, 2002.

[92] J. P. Perdew, K. Burke, and M. Ernzerhof, "Generalized gradient approximation made simple," *Phys. Rev. Lett.*, vol. 77, p. 3865, 1996.

[93] a. . Girit, J. C. Meyer, R. Erni, M. D. Rossell, C. Kisielowski, L. Yang, C.-H. Park, M. F. Crommie, M. L. Cohen, S. G. Louie, and A. Zettl, "Graphene at the edge: Stability and dynamics," *Science*, vol. 323, p. 1705, 2009.

[94] Y. Murata, V. Petrova, B. B. Kappes, A. Ebnonnasir, I. Petrov, Y.-H. Xie, C. V. Ciobanu, and S. Kodambaka, "Moire superstructures of graphene on faceted nickel islands," *ACS Nano*, vol. 4, p. 6509, 2010.

[95] Y. S. Dedkov and M. Fonin, "Electronic and magnetic properties of the graphene ferromagnet interface," *New J. Phys.*, vol. 12, p. 125004, 2010.

[96] J. Wintterlin and M. L. Bocquet, "Graphene on metal surfaces," *Surf. Sci.*, vol. 603, p. 1841, 2009.

[97] R. Addou, A. Dahal, P. Sutter, and M. Batzill, "Monolayer graphene growth on ni(111) by low temperature chemical vapor deposition," *App. Phys. Lett.*, vol. 100, p. 021601, 2012.

[98] J. Gao, J. Yip, J. Zhao, B. I. Yakobson, and F. Ding, "Graphene nucleation on transition metal surface: Structure transformation and role of the metal step edge," *J. Am. Chem. Soc.*, vol. 133, p. 5009, 2011.

[99] H. Shu, X. Chen, X. Tao, and F. Ding, "Edge structural stability and kinetics of graphene chemical vapor deposition growth," *ACS Nano*, vol. 6, p. 3243, 2012.

[100] H. Amara, C. Bichara, and F. Ducastelle, "Formation of carbon nanostructures on nickel surfaces: A tight-binding grand canonical monte carlo study," *Phys. Rev. B*, vol. 73, p. 113404, 2006.

[101] H. Amara, J.-M. Roussel, C. Bichara, J.-P. Gaspard, and F. Ducastelle, "Tight-binding potential for atomistic simulations of carbon interacting with transition metals: Application to the ni-c system," *Phys. Rev. B*, vol. 79, p. 014109, 2009.

[102] [Online]. Available: http:\ams.icn.cat

[103] J. Coraux, A. T. N'Diaye, C. Busse, and T. Michely, "Structural coherency of graphene on ir(111)," *Nano Lett.*, vol. 8, p. 565, 2008.

[104] T. Michely, M. Hohage, M. Bott, and G. Comsa, "Inversion of growth speed anisotropy in two dimensions," *Phys. Rev. Lett.*, vol. 70, p. 3943, 1993.

[105] J. Jacobsen, K. W. Jacobsen, and J. K. Nørskov, "Island shapes in homoepitaxial growth of pt(111)," *Surf. Sci.*, vol. 359, p. 37, 1996.

[106] J. Shelton, H. Patil, and J. Blakely, "Equilibrium segregation of carbon to a nickel (111) surface: A surface phase transition," *Surf. Sci.*, vol. 43, p. 493, 1974.

[107] M. Eizenberg and J. Blakely, "Carbon monolayer phase condensation on ni(111)," *Surf. Sci.*, vol. 82, p. 228, 1979.

[108] R. Rosei, S. Modesti, F. Sette, C. Quaresima, A. Savoia, and P. Perfetti, "Electronic structure of carbidic and graphitic carbon on ni(111)," *Phys. Rev. B*, vol. 29, p. 3416, 1984.

[109] K. Takahashi, K. Yamada, H. Kato, H. Hibino, and Y. Homma, "In situ scanning electron microscopy of graphene growth on polycrystalline ni substrate," *Surf. Sci.*, vol. 606, p. 728, 2012.

[110] M. Losurdo, M. M. Giangregorio, P. Capezzuto, and G. Bruno, "Ellipsometry as a real-time optical tool for monitoring and understanding graphene growth on metals," *J. Phys. Chem. C*, vol. 115, p. 21804, 2011.

[111] J. Lahiri, T. S. Miller, A. J. Ross, L. Adamska, I. I. Oleynik, and M. Batzill, "Graphene growth and stability at nickel surfaces," *New J. Phys.*, vol. 13, p. 025001, 2011.

[112] P. Jacobson, B. Stoger, A. Garhofer, G. S. Parkinson, M. Schmid, R. Caudillo, F. Mittendorfer, J. Redinger, and U. Diebold, "Disorder and defect healing in graphene on ni(111)," *J. Phys. Chem. Lett.*, vol. 3, p. 136, 2012.

[113] A. M. Shikin, D. FarIas, V. K. Adamchuk, and K. H. Rieder, "Surface phonon dispersion of a graphite monolayer adsorbed on ni(111) and its modification

caused by intercalation of yb, la and cu layers," *Surf. Sci.*, vol. 424, p. 155, 1999.

[114] A. Garcia-Lekue, T. Balashov, M. Olle, G. Ceballos, A. Arnau, P. Gambardella, D. Sanchez-Portal, and A. Mugarza, "Spin polarized electron scattering at the graphene/ni(111) interface," *to be summited*, 2013.